5-2013

MULTIFUNCTIONAL NANOPHOSPHORS FOR TISSUE IMAGING AND DRUG DELIVERY

Hongyu Chen
Clemson University, hongyuchen221@yahoo.cn

MULTIFUNCTIONAL NANOPHOSPHORS FOR TISSUE IMAGING AND DRUG DELIVERY

A Dissertation
Presented to
the Graduate School of
Clemson University

In Partial Fulfillment
of the Requirements for the Degree
ph.D of Chemistry

---

by
Hongyu Chen
May 2013

Accepted by:
Dr. Jeffrey N. Anker, Committee Chair
Dr. George Chumanov
Dr. O. Thompson Mefford
Dr. Jason McNeill

ABSTRACT

X-rays have been used for non-invasive high-resolution imaging of thick biological specimens since their discovery in 1895. They are widely used for structural imaging of bone, metal implants, and cavities in soft tissue. Recently, a number of new contrast methodologies have emerged which are expanding X-ray's biomedical applications to functional as well as structural imaging. However, traditional X-ray imaging provides high spatial resolution imaging through tissue but do not measure chemical concentrations. In this dissertation, we describe an X-ray excited optical luminescence (XEOL) technique which uses a scanning X-ray beam to irradiate Gd_2O_2S phosphors and detect the resulting visible luminescence through the tissue. The amount of light collected is modulated by optical absorption in close proximity to the luminescence source. The ability to specifically target biological processes *in vivo* makes nanophosphors promising molecular imaging agents for XEOL. We also describe versatile techniques to design and fabricate multifunctional X-ray nanophosphors. The addition of pH-triggred drug release on our X-ray nanophosphors make it possible to monitor pH-triggered drug release rate in real time. The iron oxide encapsulated X-ray nanosctintillators offer promising multimodal MRI/fluorescence/X-ray luminescence contrast agents.

DEDICATION

This work is dedicated to my parents, Huanqiang Chen and Xiju Wang, and my sister Caihua Chen.

ACKNOWLEDGMENTS

I would like to thank my advisor, Dr. Jeffrey N. Anker, for this support in my research. I would also like to thank my committee member, Dr. George Chumanov, Dr. Shiou-Jyh and Dr. Jason McNeill.

I am very grateful to the opportunity to conduct my search in Clemson University. Thanks for Dr. Wu's guidance on my career plan when I came to Clemson in my first year study. I appreciate the cooperation work with Bin Qi from Dr. O. Thompson Mefford group for the particles characterization by TEM and zeta potential. Thanks for Thomas Moore from Dr. Frank Alexis group for the toxicity studies of nanoparticles and mouse model imaging. I am also grateful for Daniel C. Colvin from Dr. John C. Gore group in Vanderbilt University for their work on MRI characterization of nanophosphor and Dr. Jian He group for their work on the magnetic characterization of nanophosphors.

I would also like to extend my thanks to my colleagues in the Anker group for their help and friendship.

TABLE OF CONTENTS

Table of Contents (Continued)
Page

LIST OF TABLES

LIST OF FIGURES

List of Figures (Continued)

Figure Page

List of Figures (Continued)

Figure Page

List of Figures (Continued)

Figure Page

List of Figures (Continued)

Figure Page

CHAPTER ONE

I. X-RAY PHOSPHORS AND THEIR APPLICATIONS

Discovery of X-ray phosphors

X-rays are electromagnetic wave with shorter wavelength (<10 nm) than the infrared, visible, or ultraviolet light. They are widely used since they were discovered in 1895 by Wilhelm Conrad Roentgen.[1-2] The research started immediately to find materials capable of converting X-ray to visible light. These materials were later named X-ray phosphors (sometimes referred to as scintillators). $CaWO_4$ powder discovered in 1896 by Pupin was used more than 75 years. A few years later, Crookes and Regener found the ZnS based phosphors. The excitation energy for X-ray phosphors is X-ray which is different from the energy sources for photoluminescent and electroluminescent phosphors. The energy sources for photo-luminescent and electroluminescent phosphors are visible or ultraviolet light and electrons, respectively.

Principle of conversion of X-ray to visible light in X-ray phosphors

The conversion of X-ray to visible light mainly can be divided into three steps (Figure 1.1). The first step involves multistep interaction of X-ray with the lattice of the phosphor or absorption of X-ray by the phosphors via the Compton and photoelectric effect. In this step, plenty of electron hole pairs are generated in the conduction bands and thermalized in the valence bands. In the second step, electron hole pairs transport through the crystal lattice. The last step consists in electron hole pair trapping by the luminescent centers (doping ions) and their radioactive combination.

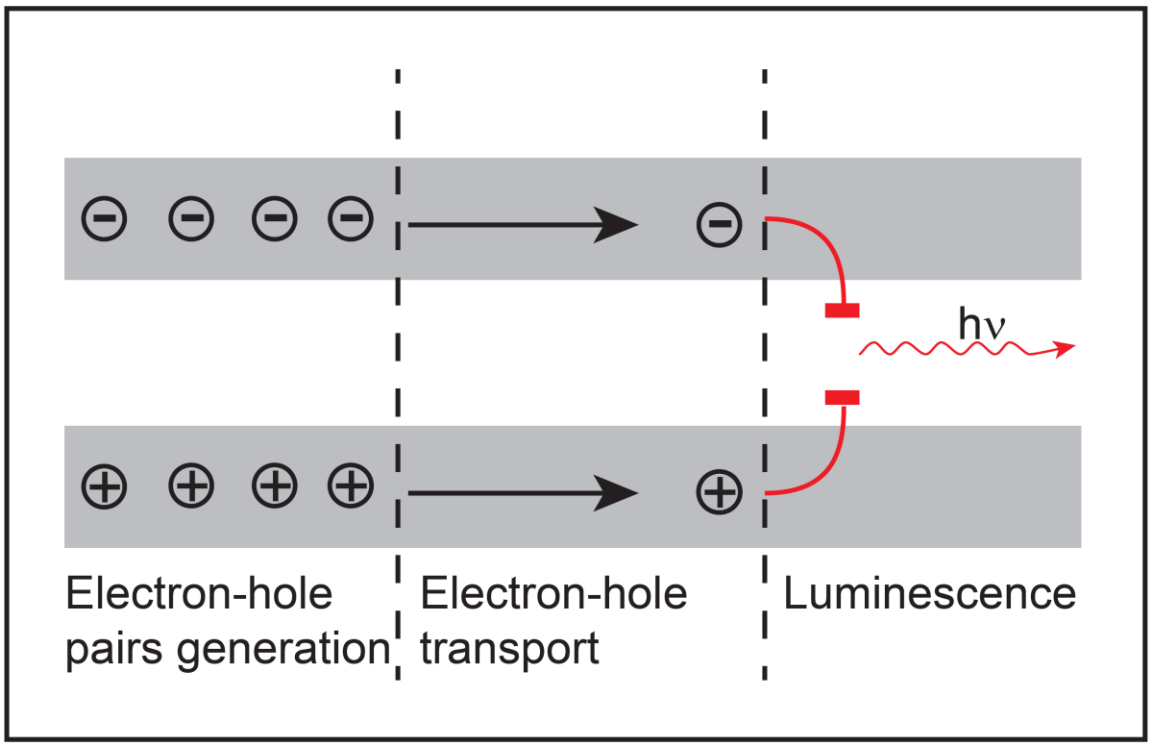

Figure 1.1 Schematic illustration of the three steps for the X-ray conversion to visible light.

Characterization of X-ray phosphors

X-ray phosphors are often used in X-ray imaging screens and films for projection imaging, fluoroscopy, and CT to convert X-ray image into light. Their most considered characteristics are the photon-conversion efficiency, luminescence decay time, and chemical stability. The total number of visible light photons emitted by X-ray phosphors under 1 keV X-ray is called photon conversion efficiency or light yield. The fundamental limit of the light yield (Y) of an activated phosphor (photons emitted/MeV) is determined by the band gap E_{gap} (eV) of the host material and is approximately given by equation (1) with a maximum of close to 40% energy efficiency.[3]

$$Y = \frac{10^6}{2.5E_{gap}} \qquad (1)$$

The fundamental limit on light output for various phosphors. The fundamental limit is smallest for fluorides with the largest band gap and the limit is largest for sulfides with small band gaps. The decay rate of the luminescence center is determined by its transition dipole moment from the excited to ground state. For most of the rare earth ions, the decay times usually in the order of μs to ms. The chemical stability is crucial for the phosphors especially hygroscopic materials in practical use because the hygroscopicity limits the long term operation of these phosphors in open air. It also limits the applications of these particles in physiological conditions which will discuss later in the X-ray excited optical luminescence technique.

Table 1.1 Examples of X-ray phosphors. Reproduced from Ref. 124 with permission from the PCCP Owner Societies.

Phosphor	Decay time (ns)	Maximum Emissior Wavelength (nm)	Conversion efficiency (visible photons/MeV)	Hygroscopicity	Density g/cm	Reference
CsI:Tl	800	550	66,000	Yes	4.51	4-6
CsI:Na	630	425	49,000	Yes	4.51	7-8
NaI:Tl	230	415	44,000	Yes	3.67	4-5, 8
LiI:Eu	1,200	475	15,000	Yes	4.08	9-10
$LaBr_3$:Ce	35	358	61,000	Yes	5.3	11
K_2LaI_5: Ce	24	420	55,000	Yes	4.4	12
CaF_2:Eu	~1,000	435	24,000	No	3.18	4, 13
SrI_2:Ce,Na	27 (25%), 450 (75%)	404	16,000	Yes	4.59	14
SrI_2:Eu	1,200	435	120,000	Yes	4.59	14
BaFBr:Eu	800	390	60,000	Yes	4.56	15-16
LaOBr:Tb	~1000,000	425	67,000	Yes	6.3	1, 17
LaOBr:Tm	~1000,000	374, 472	6,0000	Yes	6.1	18
ZnS:Ag	1,200	450	49,000	No	3.9	19
M'-$YTaO_4$	3,000	337	40,000	No	7.5	16, 18
M'-$YTaO_4$:Nb	~2,000	410	40,000	No	7.5	20-21
$BaHfO_3$:Ce	25	400	40,000	No	8.5	1, 22
$Bi_4Ge_3O_{12}$ (BGO)	300	480	9,000	No	7.1	4, 23
$CaWO_4$	8,000	425	15,800	No	6.1	24-25
$CdWO_4$	5,000	495	20,000	No	7.9	26
$YAlO_3$:Ce	24	360	20,100	No	5.35	27-28
$Y_3Al_5O_{12}$:Ce	90~120	550	16,700	No	4.55	4-5, 29
$LuAlO_3$:Ce	18	365	12,000	No	8.34	1, 30
$Lu_3Al_5O_{12}$:Ce	55	530	12,500	No	6.7	31-32
Lu_2SiO_5:Ce	30	425	33,000	No	7.4	33
Lu_2O_3:Tb,Eu	~1,000	612	30,000	No	9.4	34
Gd_2O_3:Eu	~1,000	612	40,000	No	5.91	15, 35
Gd_2O_2S:Eu	~1000,000	623	60,000	No	7.3	36
Gd_2O_2S:Tb	~1000,000	545	60,000	No	7.3	22
Gd_2O_2S:Pr,Ce,F	3,000	510	48,000	No	7.3	22
$Gd_3Ga_5O_{12}$:Cr,Ce	140,000	730	40,000	No	7.1	21, 37
Gd_2SiO_5:Ce	60	430	8,000	No	6.7	38-39

Discovered in 1896, $CaWO_4$, was used for the next 80 years in X-ray phosphor screens due to its reasonable X-ray absorption in the 20-100 keV range and blue emission.[40] However, $CaWO_4$ suffers from low conversion efficiency (only 15,000 optical photons /Mev). Currently, alkali metal halides containing small amounts of activator such as NaI:Tl and CsI:Tl are being widely used because of their superior conversion efficiency (64,000 optical photons/MeV for CsI:Tl). However, most alkali metal halides are hygroscopic requiring that the phosphors be kept moisture-free. Recently, optical ceramic phosphors have become popular due to their light conversion efficiency and chemical stability. Bismuth germanate oxide (BGO), a ceramic scinitillator, is often used due to its rapid response and little or no afterglow. The speed of response and high density make the phosphor ideal for high energy and high acquisition rate X-ray measurements. BGO is not hygroscopic, however, its low conversion efficiency (only 9,000 optical photons /Mev) results in poorer energy resolution than detectors based on alkali metal halides. Rare earth oxysulfide phosphors (M_2O_2S:Ln, M= Gd or Y. Ln= Ce, Pr, Eu, Tm, or Tb) are a promising class of ceramic scinitillators with improved absorption, greater density and higher X-ray to light conversion efficiency (60,000 optical photons/Mev).

X-ray luminescence tomography (XLT)

Though the aforementioned phosphors discussed are typically used in projection X-ray imaging and computed tomography (CT), phosphor particles with sizes ranging from nanometers to micrometers are used as contrast agents for X-ray luminescence

tomography (XLT).[41-42] The basic principle of XLT is based on luminescence measurements from selectively excited nanophosphors, it's a hybrid technique as a complementary to CT. XLT usually collects signal in physiological or mimic physiological environment. Although alkali metal halides containing small amounts of activator such as NaI:Tl and CsI:Tl have great photo conversion efficiency, but they suffer from hygroscopicity and can dissolve in physiological environment readily. Recently, rare-earth doped oxide and oxysulfide nanoparticles have been investigated as labels for low-background imaging using up-conversion,[43] radioluminescence,[18, 40] long-lifetime phosphorescence,[44-45] and proximity scintillation assays. These nanoparticles are attractive imaging agents due to their chemical stability, photostability, large X-ray absorption cross-section and scintillation efficiency, and relatively low toxicity, especially after silica encapsulation.[46] X-ray phosphors may also be coupled to photodynamic nanoparticles to enhance reactive oxygen production,[47] although their effectiveness depends greatly upon their ability to target the reactive oxygen damage to the nucleus or other sensitive sites.[48]

Through the use of a scanning luminescence X-ray microscope, Morrone imaged the optical emission of terbium labeled actin in a single cell to obtain ~50 nm resolution based on the selective excitation of lanthanide organo-polychelate complexes and optical detection of their luminescence.[49] The high resolution of this technique lies in the fact that the X-ray excited luminescence is only produced in the path of the narrow scanning X-ray beam. However, this small voxel size and weak scintillation yield necessitated the use of a very intense X-ray dose exceeding 10^8 Gy.

To increase the scintillation efficiency, Adam and coworkers proposed using quantum dots for multiplexed cell labeling.[50] Alternative optical microscopy techniques have been developed for near-field imaging in the absence of light scattering.[51-53] However, the principle of scanning X-ray excitation can also be applied to imaging in tissues thicker than 1 mm where optical scattering prevents high-resolution optical imaging.

In order to detect a wider variety of analytes with molecular information, X-ray excited optical luminescence (XEOL) based techniques were recently developed with lower backgrounds and lower X-ray doses. With a 1 mm X-ray beam and 1~100 cGy radiation dose, Pratx *et al*. developed X-ray luminescence computed tomography (XLCT) and achieved a spatial resolution of 1 mm through tissue-mimicking material.[54] X-ray phosphors are a series of materials that convert X-ray photons to visible photons when excited by an X-ray source. XLCT is similar to XFCT in its sample irradiation method, however, XLCT uses photodetectors to capture the optical photons emitted from the nanophosphors rather than an X-ray spectrometer for secondary fluorescent X-ray detection. Because the X-ray does not scatter much in tissue and the X-ray luminescence is only generated on the path of the narrow X-ray beam, the optical detector need not spatially resolve the source of luminescence. As long as the luminesence can be detected, the spatial resolution is defined by the narrow X-ray beam. The advantages of this technique are its combination of high sensitivity of radioluminescent nanoparticles and the high spatial localization of collimated X-ray beams. Pratx and coworkers recently used XLCT to image the cross sectional distribution of microsize phosphor particles in 4.5 cm of an agar tissue

phantom.[41] Carpenter recently completed a numerical phantom experiment to simulate the X-ray dose (Gy) required to achieve a signal-to-noise ratio of 10 for varying concentrations. They found that picomolar (ng/ml) concentrations of 10 nm X-ray phosphor are detectable for a mammographic-like dose.[55] They have also shown that X-ray luminescence can be observed in small animal models.[54-55]

Although high resolution was demonstrated using XLCT, the image is acquired slowly by scanning the X-ray beam through the sample and rotating the sample through 180º. In addition, there are applications such as tumor-resection where the X-ray excitation angle is limited by geometry, and where increased rapid acquisition is critical. Limited-angle X-ray luminescence tomography was deveoped to address these applications based on a hybrid X-ray/optical reconstruction, which allows XLCT spatial encoding in a limited-angle geometry, and diffuse optical spatial discrimination for the remaining dimensions. According to the model, $\mu g \cdot mL^{-1}$ particle concentrations may be observed through 5 cm of tissue with ~10 mGy doses. The limited angle technique is expected to be especially useful in surgical applicaions such as breast or brain excision due to rapid acquisition speed, convenient geometric configuration, high depth resolution, and low X-ray dose.[56]

X-ray excited optical luminescence (XEOL) can be used not only to locate X-ray phosphors in tissue, but also serve as a local light source for fluorescent and colorimetric chemical indicators. Though optical microscopy (e.g. scanning confocal microscopy) is an excellent technique for biomedical imaging, it has limited utility in tissues deeper than 1 mm because almost all light is scattered, resulting in poor

resolution.[48, 57-58] The ability to specifically target biological processes *in vivo* makes nanoparticles promising molecular imaging agents for X-ray excited optical luminescence techniques. There is a urgent need of novel X-ray nanophosphors for XEOL. However, the tranditional solid reaction methods can only provide mircosize or even bigger size particles.[18] While the commonly used coprecipiation of host material and doping ions by urea decomposition offers nanosized particles, most of the work just focus on the particles synthesis and characterization.[59] Less works have been reported on the synthesis of multifunctional X-ray nanophosphors for the chemical imaging though tissue or in vivo study.[60]

This chapter has introduced the histrical discovery, mechanism of conversion of X-rays to visible light, important characterization parameters of X-ray phosphor. Some of the important X-ray phosphors and their characterics are also included. The tranditional application of X-ray phosphors mainly in the X-ray detection and CT screen. With the developmet of XLCT, the synthesis and applicaons in deep tissue imaging or chemical detection of X-ray phosphors with nanosize attract a lot of attention in the past decades.

Chapter II describes a novel method for high-resolution chemical imaging on a surface embedded in tissue. The sensor surface consists of an X-ray scintillator film coated in a thin film loaded with chemical indicator dye. A narrow scanning X-ray beam is usedd to excite luminescence from X-ray phosphors located within the beam. This luminescence passs through the indicator film, and the spectrum is analyzed to measure chemical concentrations at that location. A pH sensor is demonstrated with a

dynamic range between pH 6 to 9 and noise level of 0.05 pH units using methyl-red dyed pH paper. The location of the interface between two types of phosphor films is obtained with 0.30 mm spatial resolution even though the images are highly blurred by 10 mm of chicken breast. This work has important applications for detecting pH changes on surfaces of implanted medical devices.

Chapter III reports a high-spatial resolution imaging technique to measure optical absorption and detect chemical and physical changes on surfaces embedded in thick tissue. Developing sensors to measure chemical concentrations on implanted surfaces through tissue is an important challenge for analytical chemistry and biomedical imaging. Tissue scattering dramatically reduces the resolution of optical imaging. In contrast, X-rays provide high spatial resolution imaging through tissue but do not measure chemical concentrations. We describe a hybrid technique which uses a scanning X-ray beam to irradiate Gd2O2S scintillators and detect the resulting visible luminescence through the tissue. The amount of light collected is modulated by optical absorption in close proximity to the luminescence source. By scanning the X-ray beam, and measuring total amount of light collected, one can measure the local absorption near scintillators at a resolution limited by the width of luminescence source (i.e. the width of the X-ray excitation beam). For proof of principle, a rectangular 1.7 mm scanning X-ray beam was used to excite a single layer of 8 μm Gd_2O_2S particles, and detect the absorption of 5 nm thick silver island film through 10 mm of pork. Lifetime and spectroscopic measurements, as well changing the refractive index of the surroundings indicate that the silver reduces the optical signal

through attenuated total internal reflection. The technique was used to image the dissolution of regions of the silver island film which were exposed to 1 mM of H_2O_2 through 1 cm of pork tissue.

Chapter IV explores a significant and novel theranostic nanotechnology that combines multimodal imaging with drug delivery. One of the greatest challenges in cancer therapy is to develop methods to deliver chemotherapy agents to tumor cells while reducing systemic toxicity to non-cancerous cells. A promising approach to localizing drug release is to employ drug-loaded nanoparticles with coatings that release the drugs only in the presence of specific triggers found in the target cells such as pH, enzymes, or light. However, many parameters affect the nanoparticle distribution and drug release rate and it is difficult to quantify drug release *in situ*. In this work, we show proof-of-principle for a "smart" radioluminescent nanocapsule with X-ray excited optical luminescence (XEOL) spectrum that changes during release of the optically absorbing chemotherapy drug, doxorubicin. XEOL provides an almost background-free luminescent signal for measuring drug release from particles irradiated by a narrow X-ray beam. We study *in vitro* pH triggered release rates of doxorubicin from nanocapsules coated with a pH responsive polyelectrolyte multilayer using HPLC and XEOL spectroscopy. The doxorubicin was loaded to over 5 % by weight, and released from the capsule with a time constant *in vitro* of ~ 36 days at pH 7.4, and 21.4 hr at pH 5.0, respectively. The Gd_2O_2S:Eu nanocapsules are also paramagnetic at room temperature with similar magnetic susceptibility and similarly good MRI T_2 relaxivities to Gd_2O_3, but the sulfur increases the radioluminescence intensity and shifts the spectrum. Empty nanocapsules

did not affect cell viability up to concentrations of at least 250 μg/ml. These empty nanocapsules accumulated in a mouse liver and spleen following tail vein injection, and could be observed *in vivo* using XEOL. The particles are synthesized with a versatile template synthesis technique which allows for control of particle size and shape. The XEOL analysis technique opens the door to non-invasive quantification of drug release as a function of nanoparticle size, shape, surface chemistry and tissue type.

Chapter V provides a mutifunctiaonl magnetic luminescent particles by partially etching and homogenous luminescent material coating method. When X-rays irradiate these radioluminescence nanoparticles, they generate visible and near infrared light that can penetrate through centimeters of tissue. X-ray luminescence tomography (XLT) maps the location of these radioluminescent contrast agents at high resolution by scanning a narrow X-ray beam through the tissue sample and collecting the luminescence at every position. Adding magnetic functionality to these radioluminescent particles would enable them to be guided, oriented, and heated using external magnetic fields, while their location and spectrum could be imaged with XLT and complementary magnetic resonance imaging. In this work, multifunctional monodispersed magnetic radioluminescent nanoparticles were developed as potential drug delivery carriers and radioluminescence imaging agents. The particles consisted of a spindle-shaped magnetic γ-Fe_2O_3 core and a radioluminescent europium-doped gadolinium oxide shell. Particles with solid iron oxide cores displayed saturation magnetizations consistent with their ~13% core volume, however, the iron oxide quenched their luminescence. In order to increase the luminescence, we partially etched the iron oxide core in oxalic acid while preserving

the radioluminescent shell. The core size was controlled by the etching time which in turn affected the particles' luminescence and magnetic properties. Particles with intermediate core sizes displayed both strong magnetophoresis and luminescence properties. They also served as MRI contrast agents with relaxivities of up to 58 mM^{-1} s^{-1} (r_2) and 120 mM^{-1} s^{-1} (r_2*). These particles offer promising multimodal MRI/fluorescence/X-ray luminescence contrast agents. Our core–shell synthesis technique offers a flexible method to control particle size, shape, and composition for a wide range of biological applications of magnetic/luminescent nanoparticles.

Chapter VI summarizes the work in this dissertation and also includes the future directions.

CHAPTTER TWO

II. HIGH-RESOLUTION CHEMICAL IMAGING THROUGH TISSUE WITH AN X-RAY PHOSPHOR SENSOR

Introduction

Advances in medical technology over the past 50 years have resulted in an increased number of patients who have implantable medical devices. The surface of implanted medical devices is a region of active chemistry due to bacterial infections, bone and tissue growth, and drug releasing stents. For example, bacteria easily colonize implanted device surfaces and form biofilms with heterogeneous pH and oxygen environments that are highly resistant to antibiotics.[61-62] Monitoring local changes in pH and other analytes would be valuable for detecting, studying, and monitoring in situ biofilm growth and chemistry. However, no conventional biomedical imaging techniques are able to perform high-resolution surface chemical imaging on surfaces. X-ray transmission and computed tomography (CT) have limited chemical sensitivity especially compared to optical techniques. Similarly, MRI and ultrasound provide high-resolution tissue imaging with limited chemical sensitivity.[63] Positron emission tomography (PET) and single photon emission computed tomography (SPECT) image the location of radiolabeled molecules and have only ~1 mm resolution due to difficulties collimating the γ rays and due to the diffusion length of the positions. In additions, they do not have surface specificity. Optical microscopy is a powerful technique for chemical analysis in biological samples. A wide variety of fluorescent and absorptive dyes are available for non-invasive, sensitive, specific, rapid, and high-resolution chemical imaging. However, the utility of optical techniques is limited in tissues deeper than 1 mm as almost all light

is scattered (no ballistic photons). It is difficult to reconstruct the original object from the blurred images except at low resolution.[58] Confocal microscopy improves image resolution in thin tissues by raster scanning a focused illumination spot through the sample and rejecting out of focus light (not originating from the focal spot) via a pinhole aperture at the image plane. In deep tissue, however, the amount of unscattered photons decreases exponentially with depth, and the focal spot becomes very large once it is dominated by diffuse photons. In practice, conventional confocal microscopy works well through tissue samples up to ~200 μm deep and under best reported conditions with two-photon NIR excitation up to about 1 mm deep.[64]

Moronne used a related scanning X-ray technique to image optical emission from terbium-labeled actin in a single cell with ~50 nm resolution, far below the far-field optical diffraction limit.[49] In addition, no pH or small analyte sensitivity was shown, and very large X-ray intensities were needed to excite light from a small number of dye molecules/pixel rather than a much larger area and volume from many scintillating particles in our work. Chen and co-workers demonstrated that X-ray excited phosphor nanoparticles can transfer energy to fluorescent photodynamic dyes.[47-48, 65] The suggested that similar X-ray phosphor/fluorescent particles could serve as oxygen dosiometers.[66] However, oxygen sensitivity and tissue imaging have not yet been shown. Recently, Pratx and co-workers developed X-ray luminescence computed tomography (XLCT) which detects the presence and location of X-ray phosphors in optically diffusive medium. Using less than 1~100 cGy of radiation dose, they achieved a spatial resolution of 1 mm through tissue-mimicking material based on the selective excitation of subpicomolar of

50 nm phosphor and optical detection of their luminescence.[54] Pratx et al. also showed that XLCT could image the cross sectional distribution of microsize phosphor particles in 1 cm of an agar tissue phantom.[41] However, sensors for small chemical analyte which can be detected using indicator dyes have not yet been explored.

Herein, we demonstrate a versatile chemical sensing technique in tissue. The image is acquired point-by-point as the sample is scanned under the X-ray beam using a principle analogous to other scanning probe microscopies such as nearfield scanning optical microscopy, (NSOM). NSOM forms images by scanning a probe across a surface and measuring the amount of light transmitted or scattered at each location.[67] The resolution of the image is largely defined by the size of the probe aperture (<50 nm for aperture NSOM), rather than the size of the spot on the photodetector (which must be at least as large as a diffraction limited spot). Chemical imaging NSOM is performed by coating modulate absorbance/fluorescence.[68] Our technique uses a similar scanning light source to image local optical absorbance and chemical concentrations through tissue, however, rather than scanning a physical probe over the surface, our light source is a "virtual probe" formed by scanning a narrow X-ray beam across an X-ray phosphor film on the implant surface. The narrow X-ray beam serves as a local excitation light source for the phosphor film and the camera serves as a single pixel detector measuring total intensity of red and green light at each sample position. The phosphors are fabricated with a thin film containing indicator dyes to modulate the luminescence spectrum collected through the tissue. Unlike conventional fluorescence microscopy, the X-ray beam is far less scattered by tissue than incident visible light so the "virtual probe size"

and image resolution is limited by the X-ray beam width. We expect that the technique will be especially valuable for measuring concentrations of chemical analytes on the surface of films such as detecting local changes in pH due to biofilm colonization of implanted device surfaces.

Results and discussion

In order to demonstrate the chemical sensitivity of our novel technique as a potential tool in diagnosis of many diseases including cancer, infection, osteolysis, and antibiotic resistance,[69-70] we developed a pH sensor by placing methyl-red dyed filter paper over a thin layer of X-ray phosphor powder (Gd_2O_2S:Tb, Phosphor Technology, Ltd. See Figure 2.1). The phosphor and pH paper were irradiated with a narrow rectangular X-ray beam from an X-ray diffractometer (Ultima IV, Rigaku Inc.), and the visible luminescence was collected with an optical fiber-coupled spectrometer (BRC741E, BWTEK, Inc. USA). (See Figure 2.2) The spectrum was collected through a strip of pH paper at a specific pH, and then a motorized stage (MTS50 Thorlabs, Inc.) moved the sample to another pH paper strip at a different pH. The phosphor spectrum displayed sharp peaks which were modulated by the pH-dependent absorbance of the filter paper.

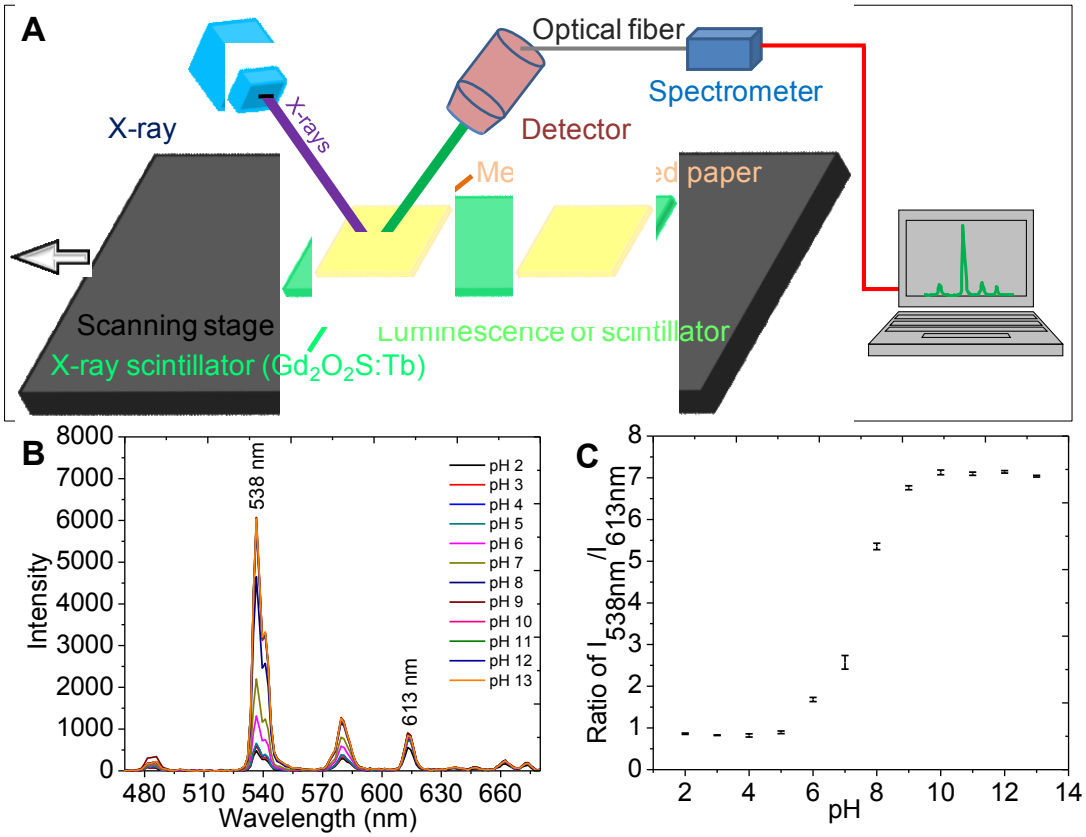

Figure 2.1 An X-ray excited pH sensor, formed by measuring spectra X-ray excited luminescence through methyl red-dyed paper. (A) Schematic, (B) Spectra of Gd_2O_2S:Tb through methyl red paper at different pHs, (C) Calibration curve: peak ratio as a function of pH. Error bars represent the standard deviation of 5 replicable trials. Reprinted with permission from ref. 112. Copyright 2011 American Chemical Society.

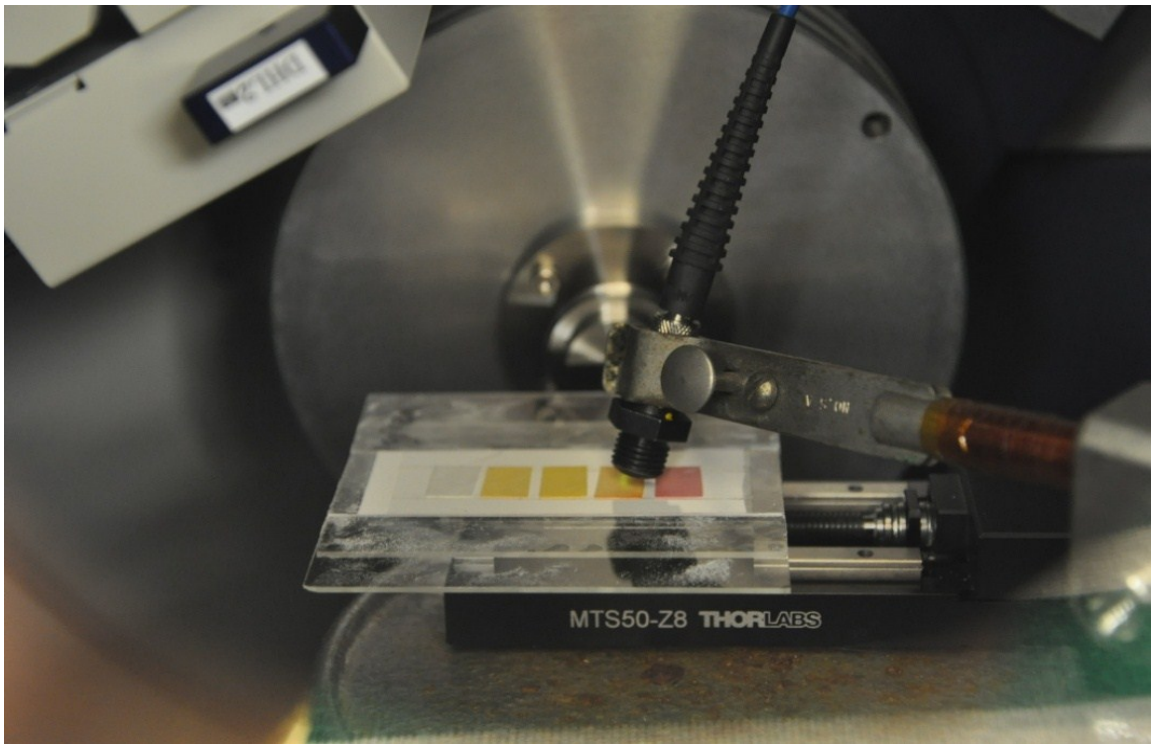

Figure 2.2 Photograph of experimental setup for measuring pH by detecting luminescence spectrum through methyl red dyed filter paper. Reprinted with permission from ref. 112. Copyright 2011 American Chemical Society.

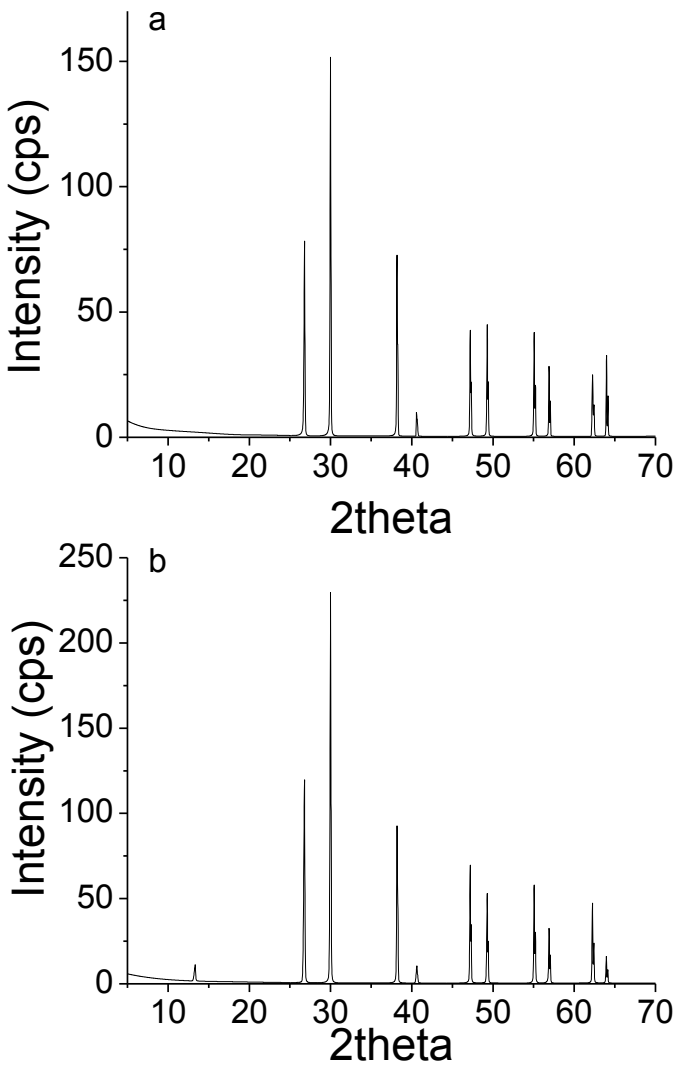

Figure 2.3 XRD patterns of the phosphor powders. (a) Gd_2O_2S:Tb (green) phosphor, (b) Gd_2O_2S:Eu (red) phosphor. Reprinted with permission from ref. 112. Copyright 2011 American Chemical Society.

Rare earth oxysulfide phosphors have been widely used for X-ray detectors due to their robustness and large quantum efficiency for X-ray to visible light conversion (~60,000 visible photons/MeV).[16, 71] Previous studies also showed rare earth ions such as Gd and Eu are not highly toxic: LD_{50} for intravenous injection is 10-100mg/kg.[72] For example, gadolinium MRI contrast agents are used in 20 million scans per year with an average dose of 1.2 g/patient.[73] The relatively low toxicity, chemical stability, and resistance to photobeaching of rare earth oxysulfide phosphors make them ideal labels in physiology conditions.[74-75] For our application, the multiple narrow and intense spectral luminescence peaks are advantageous because they are readily distinguished from phosphors doped with other rare earth elements and secondary emission from fluorescent dyes. As shown in Figure 2.1B, the intensity of the 538 nm luminescence changes with pH because of changes in the dye absorbance spectrum. The intensity of peak at 613 nm, however, was relatively constant and provides a reference. A calibration curve (Figure 2.1C) shows a dynamic range of pH 6-9 (note the pK_a of the dye shifted upon adsorption to the paper). The noise level between pH 7 and 8 was calculated to be 0.05 pH unit (based on standard deviation and slope).

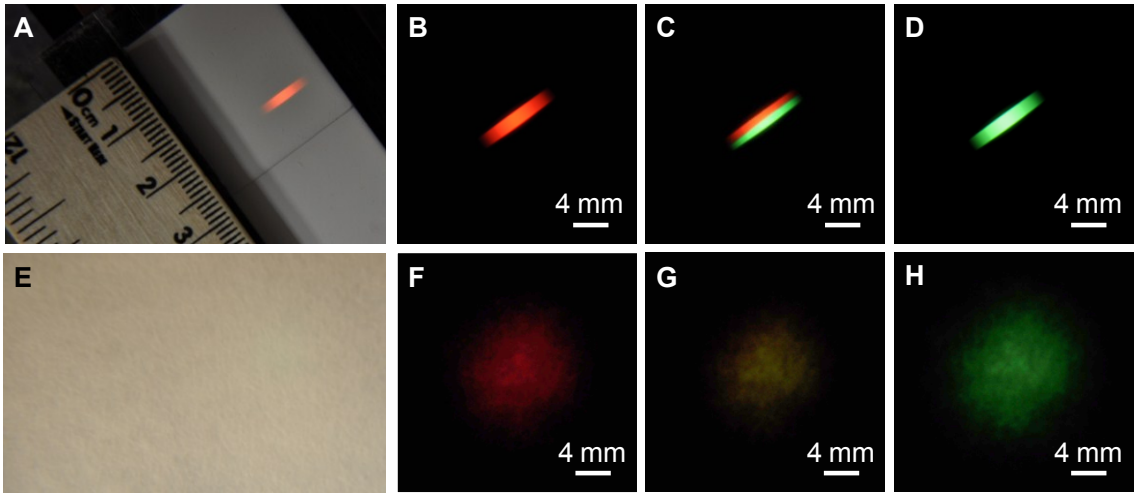

Figure 2.4 Demonstration of imaging with X-ray limited resolution. Green X-ray phosphors (Gd_2O_2S: Tb) and red phosphors (Gd_2O_2S: Eu) were deposited in a film with a sharp interface between the red and green sections. The film was irradiated by a 2.0 mm X-ray beam and a photograph was acquired at a series of sample positions (0.5 mm per step). (A) Photo of phosphor film with X-ray beam excitation and room light. (B), (C), (D) photo of luminescence (with room light blocked) as the sample was moved across the red/green (Tb/Eu) phosphor interface. The positions of each figure were 5.5 mm, 6.5 mm, 7.5 mm. (E) Same image as (A) but with the film covered by a filter paper at a distance of 10 mm. (F), (G), (H) corresponding to (B), (C), (D), respectively, but with the film covered with a filter paper. The Luminescent image is blurred by the scattering in the filter paper. Reprinted with permission from ref. 112. Copyright 2011 American Chemical Society.

Poor spatial resolution due to scattering is the most significant limitation of conventional optical microscopy in thick tissue. To demonstrate the effect of scattering upon resolution, we fabricated a two-component film with a region of Gd_2O_2S:Tb (green luminescence), a second region of Gd_2O_2S:Eu (red luminescence), and a sharp interface between the two regions. A 2 mm wide X-ray beam was used to excite optical luminescence at different regions of the film before and after adding a piece of filter paper above the sample to introduce scattering (See Figure 2.4). When the interface was illuminated, the green and red phosphor films regions can be easily resolved before the filter paper is added. After the paper is placed 1 cm above the sample, however, the luminescence spot blurs and the color looks homogeneous. This color depends upon which region is irradiated, thus scanning X-ray excited optical luminescence image is convolved with the X-ray beam profile, thus the spatial resolution depends upon the beam width. To image the phosphor interface at higher resolution through a scattering medium we reduced the X-ray slit width to produce a narrower X-ray beam (260 μm width). For a more realistic imaging scenario, we also replaced the filter paper with chicken breast tissue.(Figure 2.5). The luminescence was imaged with a Nikon D90 digital camera as the sample position was scanned relative to a fixed X-ray beam (Figure 2.5 C-F). The phosphor film was then sandwiched between two 10 mm thick sections of chicken breast and the experiment was repeated (Figure 2.5 B and G-J). Although the optical image blurred to 8.5 mm after the phosphor film was inserted into the chicken breast, the color indicated which region was under excitation. In our analysis, we treat the camera as a single pixel detector and measure the total red, green, and blue pixel intensity in each

picture using MATLAB scripts. The 90%/10% knife-edge resolution was 0.16 mm without tissue, and 0.17 mm with tissue; the full knife-edge resolution including the most tails was approximately 0.26 mm without tissue and 0.30 mm with tissue (Figure 2.6). The small resolution increase in the tissue was likely due to imperfect sample alignment and scattering of the incident X-rays in the tissue.

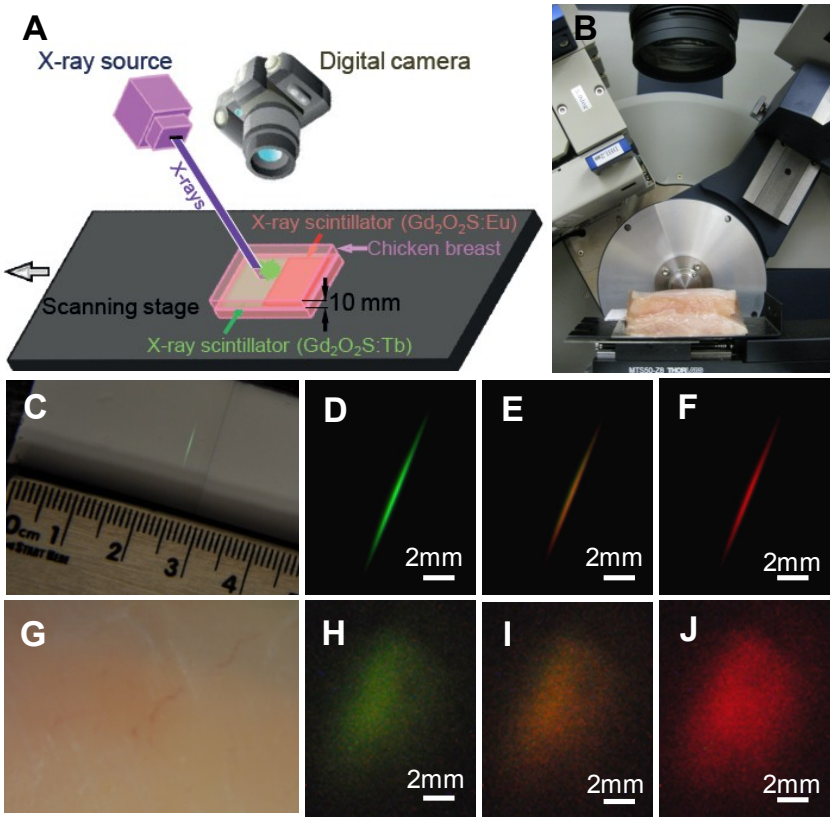

Figure 2.5 Example of imaging XEOL with X-ray limited resolution. Green X-ray phosphors (Gd_2O_2S:Tb) and red phosphors (Gd_2O_2S:Eu) were deposited in a film with a sharp interface between the red and green sections. The film was irradiated by a narrow rectangular X-ray beam and a photograph was acquired at a series of sample positions (20 μm steps). (A) Setup schematic. (B) Setup photograph. (C) Photo of phosphor film with X-ray beam excitation and room light. (D), (E), (F) Photo of luminescence (with room light blocked) as the sample was moved across the red/green (Tb/Eu) phosphor interface. (G) Same image as (C) but with the film inserted between two 10 mm thick sections of chicken breast. (H), (I), (J) corresponding to (D), (E), (F), respectively, but with the film inserted into chicken breast. The luminescent image is blurred by the scattering in the

tissue from 0.26 mm to ~8.5 mm. The color ratio is shown as a function of position in Figure 2.6. The positions of D, E, F and H, I, J in Figure 2.5 were 0.12 mm, 0.22 mm, 0.42 mm, respectively. Reprinted with permission from ref. 112. Copyright 2011 American Chemical Society.

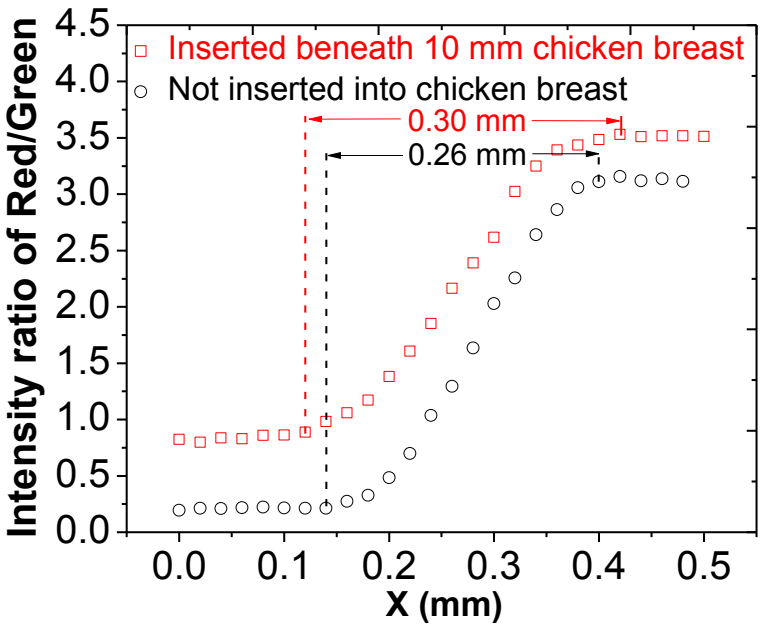

Figure 2.6 Ratio of red to green light intensity scanned at different positions (20 μm step size) with/without 10 mm of tissue. It gives evidence of optical contrast at 0.30 mm resolution through 10 mm chicken tissue. Reprinted with permission from ref. 112. Copyright 2011 American Chemical Society.

The technique has three advantages compared to conventional X-ray absorption images. First, indicator dyes provide chemical sensitivity. Second, phosphor luminescence is a positive contrast mechanism with essentially no background, while conventional X-ray transmission imaging detects small changes in the relatively large background of transmitted X-rays, although contrast is enhanced using barium, gold nanoparticles and other contrast agents.[76] The positive contrast allows relatively non-invasive X-ray doses to be used. For phosphor films, doses are typically equal to or less than that used in conventional X-ray imaging, except with blue light or deep tissue where tissue absorbance can reduce total signal intensity. Third, multiple phosphors may be used with distinguishable spectra for multiplexed imaging. It should be noted that conventional X-ray images can be co-registered simultaneously with luminescence if X-ray detectors are used to capture the transmitted X-rays while the optical detectors measure luminescence.

A visible/near-infrared point light source in an infinite tissue slab is attenuated by a factor of 3 to 300 per cm of tissue depending on the type of tissue and wavelength used.[77] Spectral distortion remains a potential problem for our technique, although the use of lanthanide phosphors with long lifetimes and narrow peaks can greatly mitigate the problem. Spectral distortion is caused by effective attenuation in tissue which is wavelength dependent according to the photon diffusion model:

$$\mu_{eff} = (3\mu_a(0.35\mu_a + \mu_s'))^{1/2} \qquad (2)$$

Where μ_{eff} is the effective attenuation coefficient, μ_a is the absorption coefficient, and μ_s' is the reduced scattering coefficient.[78-79] For example, although figure shows that the spatial resolution was hardly affected by the 10 mm thick chicken breast, it is also evident that the red/green ratio increased, especially for the Gd_2O_2S:Tb phosphor because the 538 nm light is more rapidly attenuated than the 613 nm light. The methyl red absorption causes a similar effect, thus the chicken breast tissue can cause interference if not adjusted for. The tissue absorbance disproportionately affects the color ratio detected by the digital camera because the camera filters are not tuned to the luminescence peaks. However, the shift is considerably smaller between two nearby spectral peaks (e.g. 613 nm and 620 nm in the Gd_2O_2S:Tb and Gd_2O_2S:Eu phosphors, see Figure 2.7). In addition, there are several ways to address the spectral distortion such as a function of time. Phosphorescence lifetime is alternative approaches which are not affected much by scattering. Photoacoustic imaging is the only other technique that can provide high-resolution visible imaging deep in tissue. Both X-ray phosphor imaging and

photoaccoustic imaging avoid the problems of visible light scattering by converting between visible light and another energy source.

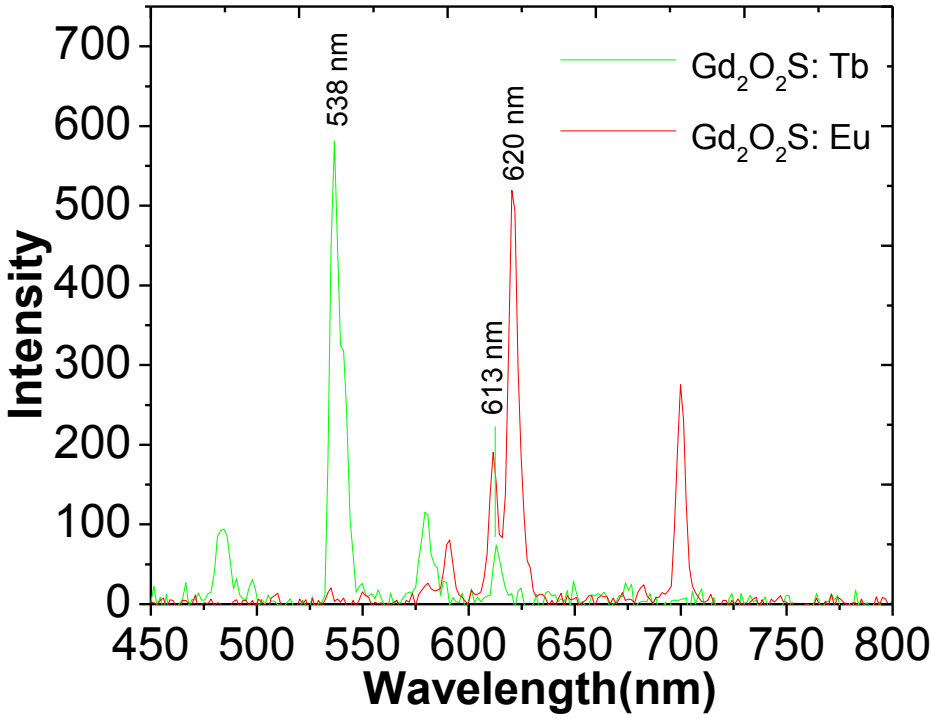

Figure 2.7 Luminescent spectra of Gd_2O_2S:Tb and Gd_2O_2S:Eu phosphors. Reprinted with permission from ref. 112. Copyright 2011 American Chemical Society.

Photoaccoustic microscopy measures acoustic waves generated by photothermal expansion of tissue that absorbs a short pulse of intense light. The acoustic waves generated are far less scattered than the optical waves and the image resolution is limited by the acoustic transducer (45 μm lateral resolution and 3 mm imaging depth with a 50 MHz transducer) rather than the optical diffraction.[80] The main limitations are that (a) tissue scattering and absorption cause spectral distortions, and no lifetime discrimination

techniques are available, (b) bone and metal can cause spatial distortions, (c) photoacoustic microscopy requires a wavelength tunable high power pulsed laser, and (d) samples must be immersed in an acoustic bath.

Conclusion

In summary, we developed a novel technique for in situ chemical imaging in tissue. It combines chemical sensitivity from indicator dyes, demonstrated by the pH sensor, with high spatial resolution, demonstrated by detecting a two-color X-ray phosphor object with 0.30 mm resolution through 10 mm of chicken breast. The technique is sensitive because it is essentially background-free. The X-ray phosphors with different emission spectra make them versatile sensing agents for colorimetric detection. Future work involves using chemical indicator dyes for oxygen and other analytes, developing lifetime-based chemical sensors which will not be affected by tissue attenuation, using narrower X-ray beams and more sensitive detection optics for two dimensional chemical imaging and tomography, and developing a portable imaging system. Two dimensional chemical imaging will be especially useful for measuring chemical changes on a surface, such as in situ detection of acidosis, hypoxia, and hydroxyapatite degradation on implanted devices with bacterial colonies.[62, 81]

Experimental Section

Materials

Methyl Red ($C_{15}H_{15}N_3O_2$) and filter paper (medium porosity) were purchased from Fisher Scientific Co. (Fair Lawn, NJ, USA). pH buffers solution was purchased from BDM Chemicals Ltd (Poole, Dorset, UK). Terbium-doped gadolinium oxysulfide phosphor powder (Gd_2O_2S:Tb) and Europium doped Gadolinium oxysulfide (Gd_2O_2S:Eu) were purchased from Phosphor Technology Ltd. (Stevenage, UK). Both Gd_2O_2S samples contained microparticles that ranged in size from 2-15 μm with a nominal diameter of 8 μm. Carboxymethyl cellulose sodium was purchased from TCI (Tokyo, Japan). Cover glass was purchased from Electron Microscopy Sciences (Fort Washington, PA, USA). Deionized (DI) water and ethanol were purchased from EMD Chemicals Inc. (Gibbstown, NJ, USA). Chicken breast was purchased from Coleman Natural Foods, Inc. (Golden, CO, USA). All chemicals were used as received without further purification.

Preparation of phosphor film: 1.0 g Gd_2O_2S:Tb phosphor powder was mixed with 2 mL carboxymethyl cellulose sodium aqueous solution (0.5% w/v) and the entire solution was applied to a cover glass (24×60 mm) and allowed to dry overnight. The film of Gd_2O_2S:Tb and Gd_2O_2S:Eu phosphor coated on the same glass slide (25×75 mm) was prepared in a similar way. 0.5 g Gd_2O_2S:Tb phosphor and 0.5 g Gd_2O_2S:Eu phosphor were each drop-coated onto a separate cover glass (24×60 mm). These two phosphor-coated cover glasses were brought together and stuck to a glass microscope slide (25×75 mm) using double-sided tape.

Preparation of methyl red dyed filter paper and pH measurement: A 12×100 mm strip was prepared from filter paper of medium porosity and this strip was immersed in 600 µL ethanolic solution of methyl red (0.05% w/v) over night and dried thoroughly. The ethanolic solution of methyl red (0.05% w/v) was prepared by adding 0.0010 g methyl red powder into 2.00 ml ethanol. The 12×100 mm methyl red dyed strip then was cut into a series of 12×8 mm pH-strips. After that, these pH-strips were placed onto a No. 0 coverslip covering the phosphor film as shown in Figure 2.2. A series of calibrated pH buffer solution (pH 2.00-13.00) were then pipette onto each pH strip (10 µL). The stage was moved so that each pH strip was irradiated and a series of five spectra were recorded from different areas of the strip to determine the average and standard deviation of the peak intensity ratio, as shown in Figure 2.1.

Instrumentation

To determine the phase of the samples, X-ray powder diffraction was performed at 40 kV and 40 mA using a Rigaku Ultima IV X-ray diffractometer with CuKα radiation at a scanning rate of 0.5º/min from 5º to 70º. The XRD patterns (Figure 2.3) were almost identical. They displayed narrow peaks indicative of particles with average crystal domains > 90 nm in diameter.

For X-ray phosphor luminescence, the X-ray diffractometer was operated at 120º with tube voltage of 40 kV and tube current of 50 mA. Luminescent spectra were captured at room temperature with a FPC-400-0.22-1.5-UV fiber coupled photodiode array spectrometer (BRC741E-02 BWTEK Inc, Newark, DE, USA).The stepper motor

stage (MTS 50, Thorlabs, Inc. Newton, NJ, USA) was controlled by a program written in Labview (National Instruments, Austin, TX, USA).

The luminescent images in Figure 2.4 were taken with a Nikon D90 digital camera with a 67 mm diameter lens at 50 mm FL and a macro lens adaptor. All the parameters of the camera were controlled by the software of Camera Control Pro2 (Nikon Instruments Inc., Melville, NY, USA). The images without chicken breast (Figure 2.4 C-G) were taken at ISO=200, shutter speed 1/4 s, f/5.6. The images with the phosphor between two 10 mm thick sections of chicken breast (H-J) were taken at ISO=2000, shutter speed 30 s, and aperture f/4.0. The increased exposure time, ISO and aperture were necessary because the luminescence was dispersed over a wider area (~8.5 mm instead of 0.26 mm), and the light and X-ray beam were attenuated by passing through the tissue. A more sensitive detector (e.g. a photomultiplier tube or avalanche photodiode) would require far shorter exposure times. All images were analyzed by Matlab R2008b.

In order to determine the X-ray beam width in Figure 2.4, we measured the ratio of red/green intensity at the interface between the Gd_2O_2S:Tb and Gd_2O_2S:Eu phosphor films. In addition to this intensity ratio we also measured absolute green intensity of a phosphor film edge, which provided a similar beam width 0.26 mm as shown in Figure 2.6.

CHAPTTER THREE

III. OPTICAL IMAGING IN TISSUE WITH X-RAY EXCITED LUMINESCENT SENSORS

Introduction

Non-invasive biomedical imaging techniques are important for diagnosing diseases studying disease processes. Bright-field and fluorescence microscopy are excellent techniques for chemical imaging in cells and thin tissue sections (<~200 μm) because a wide range of fluorescent indicator dyes and nanoparticles are available that provide high chemical sensitivity and selectivity. However, optical microscopy is of limited utility in tissues deeper than 1 mm because almost all light is scattered causing poor resolution.[82-83] For tissue imaging other techniques are used such as X-ray transmission and computed tomography (CT), ultrasound, and magnetic resonance imaging (MRI). These techniques provide high spatial resolution, but have limited chemical sensitivity especially compared to optical techniques.[84] Positron emission tomography (PET),[85] single photo positron emission computed tomography (SPECT),[86] and Cerenkov radiation optical imaging[87] are used to measure the *in vivo* distribution of injected radioactive analytes. However, detection is limited in that the analyte must be radiolabelled, the resolution is typically in millimeters, and there is only a relatively short observation half-life (typically hours). Herein, we report a novel high-spatial resolution imaging technique to measure optical absorption and detect chemical and physical changes through thick tissue. The technique uses a narrow X-ray source to excite luminescence from X-ray phosphors at a resolution limited by the X-ray beam-width. The

phosphors serve as light sources with spectra and intensity that depend on local absorption. Here we detect changes in luminescent intensity and spectrum due to deposition of silver and gold nanoparticles onto the phosphors. We demonstrate imaging of silver and gold patterns through 10 mm pork, and describe the mechanism of luminescent attenuation.

Rare earth oxysulfide phosphors we used in this study have been widely used for X-ray detectors due to their robustness and large quantum efficiency for X-ray to visible light conversion.[16, 18, 71, 88] Previous studies also showed rare earth ions such as Gd^{3+} and Eu^{3+} are not highly toxic: LD_{50} for intravenous injection is 10-100mg/kg.[72] For example, chelated gadolinium MRI contrast agents are used in 20 million scans per year with an average dose of 1.2 g/patient.[73] The relatively low toxicity, chemical stability, and resistance to photobeaching of rare earth oxysulfide phosphors make them ideal labels in physiology conditions.[74-75] They are used in X-ray excited optical luminescence (XEOL) to map luminescent centers in semiconductor and rare-earth doped materials.[89-90] The principle can also be applied to detection of scintillation in cell labeling studies, for example, Morrone used a form of scanning X-ray excited optical luminescence (XEOL) to image optical emission of terbium labeled actin in a single cell and obtained a ~50 nm resolution.[49] However, other optical techniques are available for near-field imaging in the absence of scattering,[91-92] and they did not apply their technique to the challenge of tissue imaging where light scattering causes far more severe blurring (typically a ~10 mm point spread for imaging through 10 mm of tissue). Adam and coworkers also proposed using quantum dots for multiplexed cell labeling XEOL experiments using a table-top soft X-

ray source.[50] Chen et al demonstrated energy transfer between X-ray excited phosphor nanoparticles which caused X-ray excited photodynamic, therapy,[48, 65-66] but chemical sensitivity and tissue imaging have not yet been shown. Recently, Pratx and co-workers developed X-ray luminescence computed tomography (XLCT) which detects the presence and location of X-ray phosphors in optically diffusive medium. Using 1-100 cGy of radiation dose, they achieved a spatial resolution of 1 mm through tissue-mimicking material based on the selective excitation of subpicomolar of 50 nm phosphor and optical detection of their luminescence.[54] Pratx et al. recently showed that XLCT could image the cross sectional distribution of microsize phosphor particles in 1 cm of an agar tissue phantom.[41] However, sensors for small chemical analyte in thick tissue have not yet been explored. We demonstrate below that scanning XEOL can be used for high-resolution imaging of local optical absorption through tissue.

Results and discussion

Imaging silver coating on X-ray phosphors in 1 cm tissue

High-resolution imaging of small features through tissue can be challenging. Conventional X-ray imaging detects attenuation of transmitted X-ray photons, and contrast requires a relatively large change in sample thickness or density. However, XEOL is a positive contrast method which can detect lower concentrations of particles. In addition, it is able to detect local absorption from indicator dyes and inorganic materials, which enables high contrast and chemically specific imaging. For example, gold has an X-ray absorption cross section of only a factor of ~1000× more than tissue,

while the visible and NIR attenuation constant for a gold nanoparticle can be 10^8 times larger than tissue allowing detection of nanometer thick gold films through a centimetre of tissue.

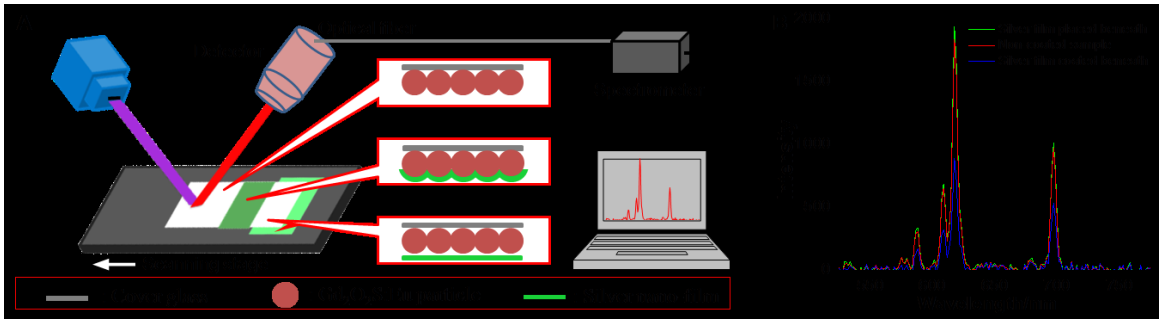

Figure 3.1 (A) Schematic of the scanning X-ray excited optical luminescence (XEOLs) absorption imaging technique. (B) Spectra of europium doped gadolinium oxysulfide (Gd_2O_2S:Eu) film either uncoated or coated with 5 nm of vapour deposited silver. As a control for whether silver contact was needed to attenuate XEOL, a glass slide coated with 5nm of silver was also placed beneath the phosphor. Reproduced from Ref. 123 with permission from the Royal Society of Chemistry.

Gold and silver nanoparticles are especially interesting materials for spectrochemical sensors because they support a localized surface Plasmon resonance (LSPR) mode, which provides intense sized- and shape-dependent optical absorption and scattering spectra.[93] They are used in a wide variety of chemical sensors based upon refractive index changes as well as nanoparticle aggregation and disaggregation.[94-95] Silver nanomaterials are also important antimicrobial agents and have been proposed as a method to prevent and reduce implant associated infection.[95-96] Methods to study the *in*

situ silver dissolution rate and amount of silver coating remaining would thus be valuable for evaluating antimicrobial efficacy and silver toxicity.

To demonstrate that a thin silver coating can be detected and imaged using scanning tissue XEOL, we formed a monolayer of 8 μm Gd_2O_2S:Eu phosphor on tape, and vapour-deposited a 5 nm thick silver film onto one side of the film. A physical mask was employed so that one region was silver-coated and another left uncoated with a sharp transition between the two regions. The silver coated film was irradiated with X-rays, and the luminescence intensity was measured as shown in Figure 3.1. The intensity of the silver-coated region was attenuated by 51% (at 617 nm) compared to the uncoated region. Direct coating of the silver onto the phosphors was required: a control prepared by placing a 5 nm silver-coated cover glass beneath the same slide of uncoated sample resulted in an increase of intensity (5%) rather than reduction because of increased reflection (see Figure 3.1 B).

The multiple narrow and intense spectral luminescence peaks of Gd_2O_2S:Eu are advantageous because they are easily distinguished from secondary emission of fluorescence from tissue. The strong red and near infrared luminescence peaks are only weakly absorbed by tissue, although scattering greatly reduces resolution.

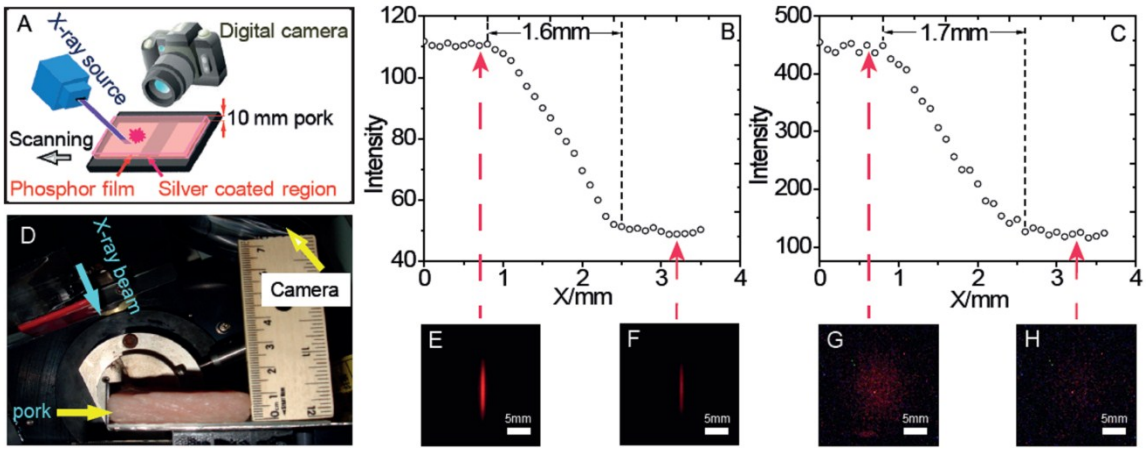

Figure 3.2 (A) Schematic of the scanning X-ray excited optical luminescence (XEOLs) absorption imaging technique in tissue. (B), (C) Intensity of red light scanned at different positions with/without 10 mm of tissue. The full-width resolution is 1.7 mm through the pork tissue (half-width is 0.85 mm). (D) Setup photograph of X-ray phosphor film under 10 mm pork. (E) Photograph of XEOL for the X-ray beam on a region of bare phosphor. (F) Photograph of XEOL for a region of silver-coated phosphor. (G), (H) Same image as (E), (F) but with the film under 10 mm thick section of pork, and with a larger exposure time (30 s). Reproduced from Ref. 123 with permission from the Royal Society of Chemistry.

To measure the spatial resolution of the scanning XEOL, a rectangular X-ray beam (1.7 mm × 10 mm) irradiated the silver-coated phosphor sample through 1 cm of pork tissue (Figure 3.2 A, D). The luminescent intensity was imaged with a Nikon D90 digital camera as the sample position was scanned relative to a fixed X-ray beam. Although each optical image showed a blurred 10 mm luminescence region due to scattering, the

intensity and spectrum was modulated by local optical absorption. The total red, green, and blue pixel intensity in each picture was analyzed in Matlab. The total intensity collected as a function of position shows a clear knife-edge profile with a full-width of just 1.7 mm through 10 mm of tissue (Figure 3.2C), limited by the X-ray beam width. The slight broadening from 1.6 mm without the tissue is likely due to misalignment of the phosphor film after placed under 1 cm pork, or a halo effect from scattering of soft X-rays.

Attenuation Mechanism

Having demonstrated high spatial-resolution imaging through tissue, we decided to investigate the mechanism by which silver attenuated XEOL. Three potential mechanisms were initially considered. (a) Irreversible damage to the phosphor during vapour deposition. This mechanism was ruled out after we showed that the intensity recovered when the silver was dissolved in H_2O_2. (b) Energy transfer and dynamic quenching of the Eu excited state by the silver nanoparticles. Silver and gold are known to be efficient fluorescence quenchers[97-98] and research by Chen and co-workers demonstrated that nanophosphors are able to transfer their energy to generally less efficient fluorescent dye.[99-100] However, the phosphor particles had an average diameter of 8 μm, and Forster energy transfer generally occurs over distances <10 nm and would therefore only be efficient near the surface of the particle unless there is very long lifetime and efficient energy diffusion to the surface. The hallmark of dynamic energy transfer is a decrease in the excited state lifetime, which was measured below. (c) Local absorption of light by the silver nanoparticles, i.e. the "inner filter effect." Since the

phosphor particles are significantly larger than the wavelength of light, we expected geometric optics to largely apply. However, no direct absorption was possible because the silver was deposited beneath the phosphors and the camera was imaging from above (see Figure 3.1).

Based on the experiments outlined in Figure 3.1A, the likely mechanism is indirect absorption due to attenuated total internal reflection. We also note that a 5 nm silver film deposited on the top rather than bottom side of the phosphors reduced the luminescence intensity by a total of 61% (at 617 nm) when viewed from above. (see Figure 3.3). The intensity is reduced because the silver lies between the phosphor and the camera and acts as a filter.

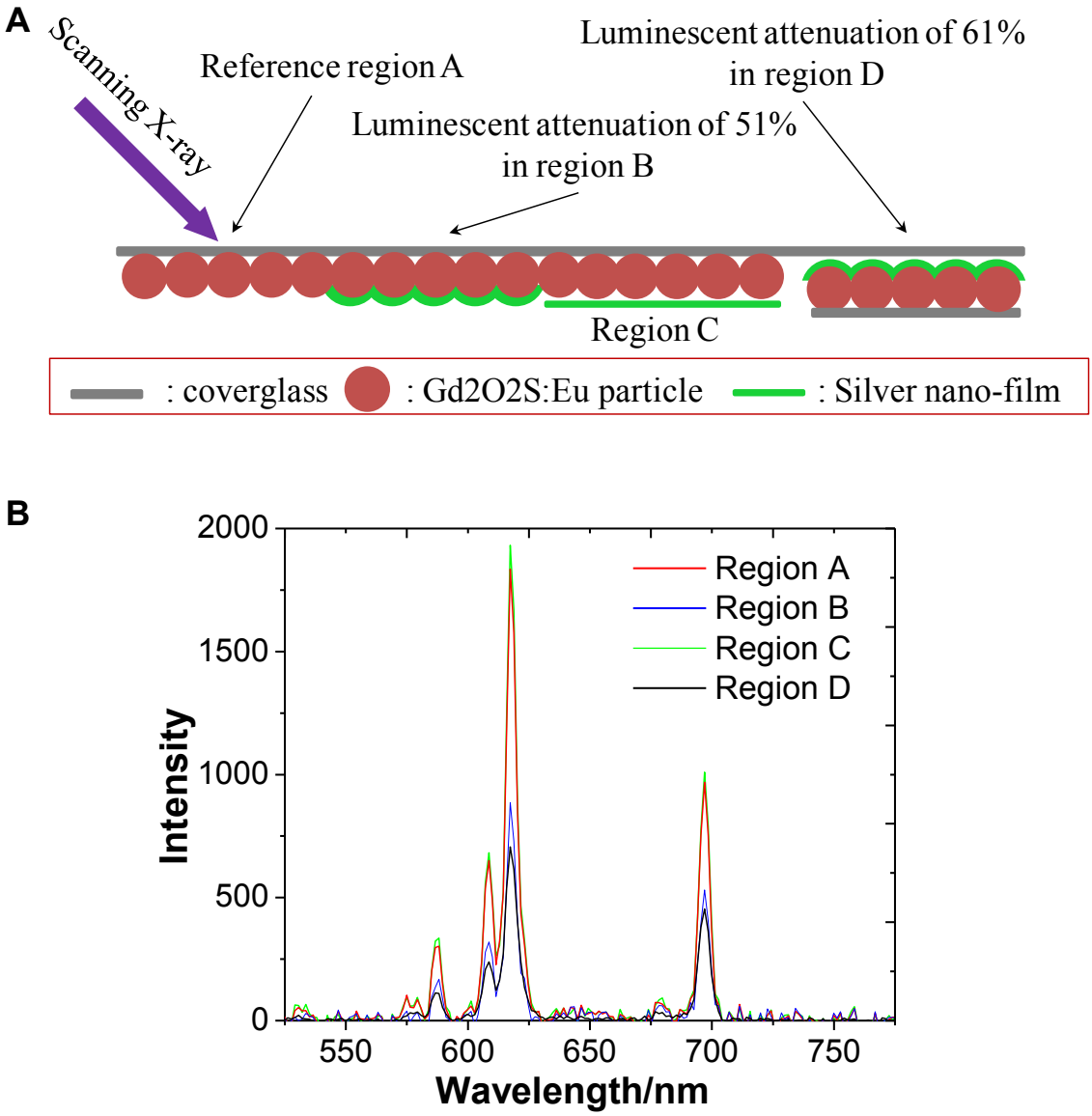

Figure 3.3. (A) Different mode of luminescent attenuation compared with reference region, (B) Luminescence spectra of different region of phosphor film. Reproduced from Ref. 123 with permission from the Royal Society of Chemistry.

Luminescence Lifetime

To determine if the silver caused dynamic quenching of the X-ray luminescence, we measured the XEOL lifetime. An optical chopper was placed in front of the X-ray beam and rotated at 250 Hz. A small amount (~3%) of X-ray energy passes through the 1 mm thick Al chopper wheel even in the blocked state; however, a clear signal modulation is evident (see Figure 3.4). The luminescence lifetime(s) was determined from the shape of the curve. After a short transition period while the chopper shifts from not blocking the X-ray beam to fully blocking the beam, the intensity is expected to decay exponentially as follows:

$$I(t) = I_0 e^{-t/\tau}$$

where *I(t)* is the intensity at time, *t*, I_0 is the intensity at time t=0, and τ is the luminescence lifetime of the X-ray phosphor. A plot of ln(*I*) vs. *t* shows a linear curve indicating a single lifetime over the observed timescale (Figure 3.4B, C). The lifetime of phosphor luminescence from silver coated and uncoated samples is 0.387 ms and 0.390 ms, respectively. The lifetimes are similar to the nominal value quoted for the Gd_2O_2S:Eu phosphor of no more than 0.45 ms.[101] The unchanged lifetime between coated and uncoated samples indicate that dynamic quenching was not responsible for attenuated XEOL intensity, and absorption is the most likely alternative.

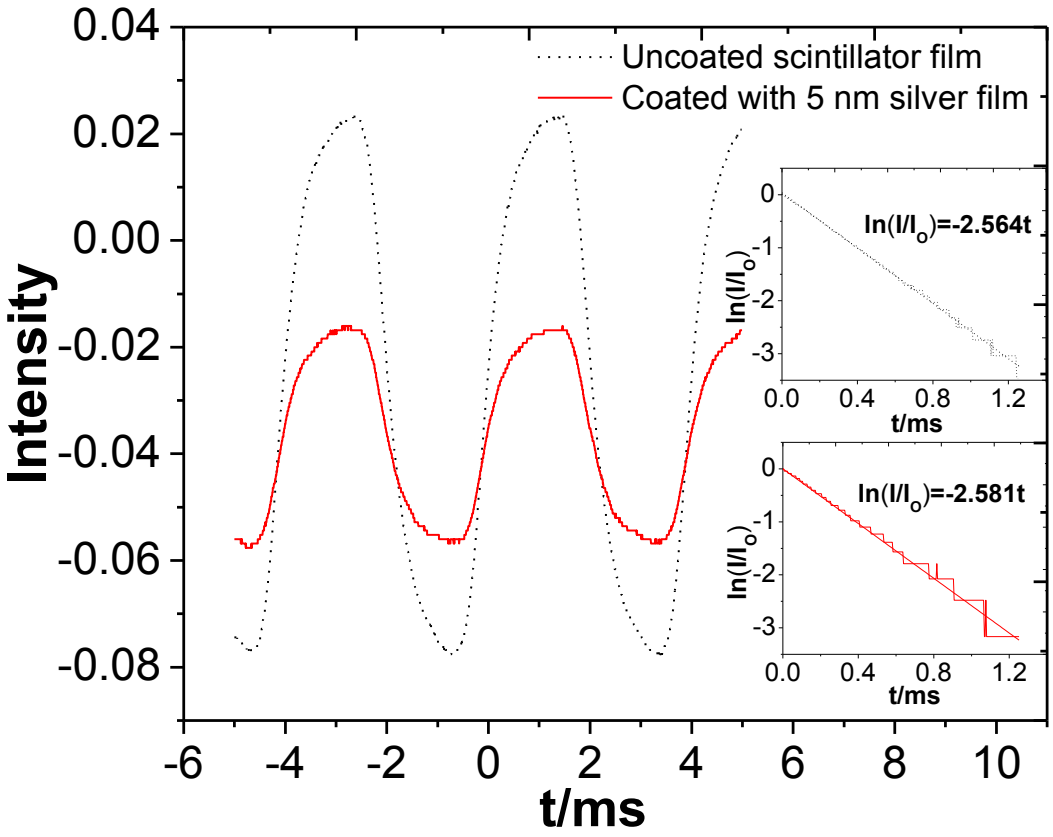

Figure 3.4 (A) Luminescence responses resulting from X-ray pulse at 250 Hz measured with a photomultiplier tube (B). (C) Plot of the log of the intensity vs. time after the chopper blocked the X-ray beam. Digitization noise is evident at low intensities. Lifetimes for coated and uncoated samples are 0.387 ms, and 0.390 ms, respectively. Reproduced from Ref. 123 with permission from the Royal Society of Chemistry.

Effect of silver film thickness on luminescent absorption

To determine if absorption was responsible for the reduced XEOL intensity, we measured the XEOL intensity at various wavelengths as a function of silver film thickness. We reasoned that if absorption were responsible, the signal would be smaller

at wavelengths which are more strongly absorbed by silver nanoparticcles. The LSPR absorption spectrum depends strongly on nanoparticle shape. Silver island film nanoparticles are formed during vapour deposition, and as more silver is deposited the particles become flatter until a continuous film is formed. Figure 3.5 shows SEM images of progressively thicker silver film deposition. The particles change in shape from small and approximately spherical to larger flatter particle shapes and eventually continuous films with some surface roughness. For particles deposited upon a flat glass surface, this change in shape leads to a larger transverse LSPR resonance and a red-shift in extinction spectrum as shown in Figure 3.6A. When the silver is deposited upon the angled and faceted surfaces of the phosphor microparticles the extinction spectrum (Figure 3.6B) is blue-shifted compared with the spectrum on flat glass due to changes in nanoparticle orientation and shape.

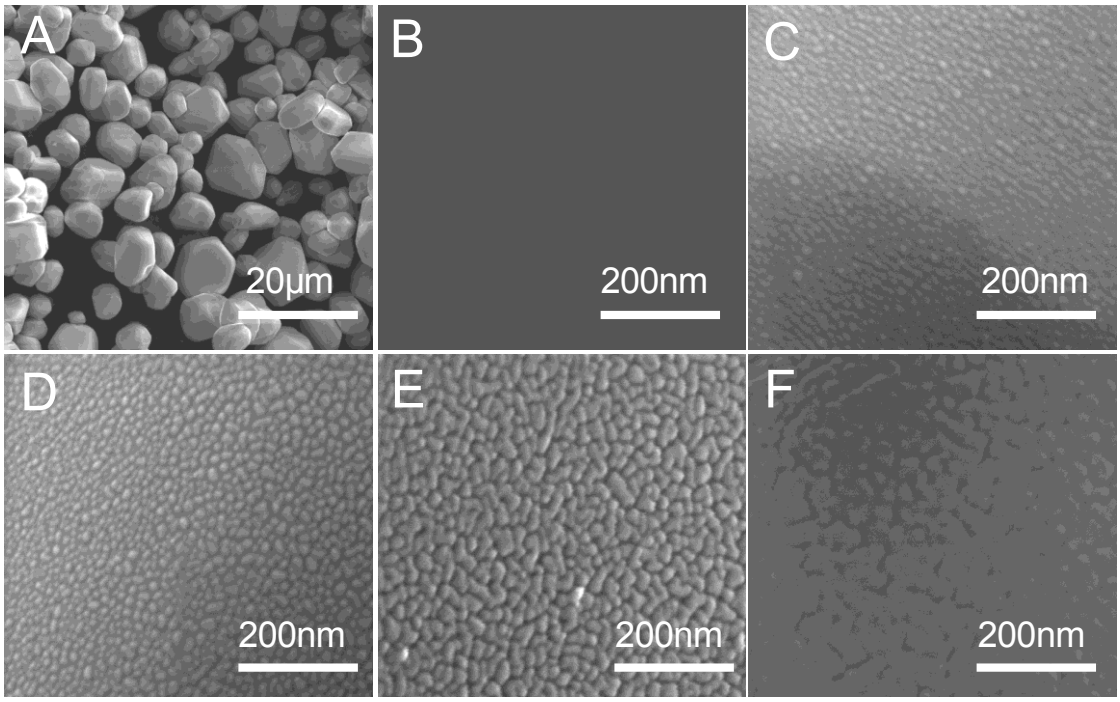

Figure 3.5 SEM images of (A) phosphor particles (B)-(F) Close up view of the phosphor surface coated with different thicknesses of silver: (B) 0 nm silver, (C) 3 nm, (D) 5 nm, (E) 10 nm, (f) 20 nm. Reproduced from Ref. 123 with permission from the Royal Society of Chemistry.

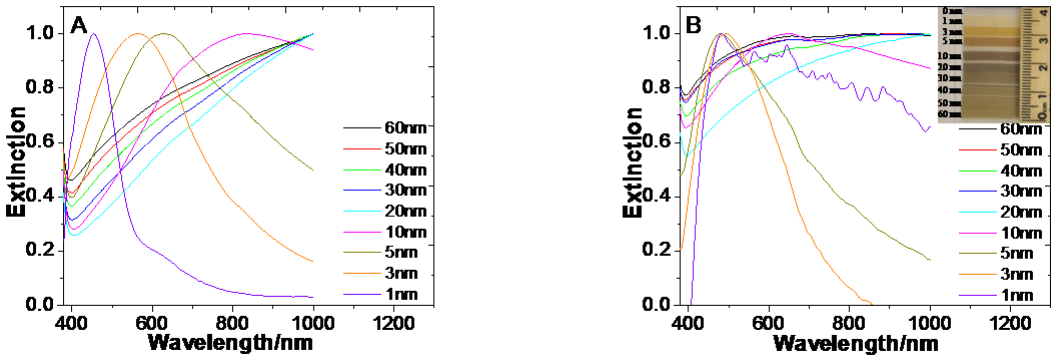

Figure 3.6 (A) Extinction spectra of silver film on cover glass (cover glass was used as the reference). All spectra are normalized to A_{max}=1. The real A_{max} for 1, 3, 5, 10, 20, 30, 40, 50, 60 nm are 0.02, 0.17, 0.31, 0.59, 0.84, 1.25, 1.60, 1.95, and 2.23, respectively. (B) Extinction spectra of silver film on phosphor particles (phosphor film coated cover glass was used as the reference). All spectra are normalized to A_{max}=1. The real A_{max} for 1, 3, 5, 10, 20, 30, 40, 50, 60 nm are 0.02, 0.09, 0.14, 0.51, 0.55, 0.69, 0.83, 0.87, and 0.90, respectively. Inset shows a photograph of the silver coated phosphor film. Reproduced from Ref. 123 with permission from the Royal Society of Chemistry.

The XEOL spectrum depended on the silver deposition thickness (see Figure 3.7A). The variation of relative luminescence lost for film from 1 nm to 10 nm can be explained by the size and shape-dependent absorption properties of the nanparticles in the silver island film. (See Figure 3.6). In general, the luminescent attenuation order for each peak is 588 nm> 608 nm> 617 nm> 697 nm which is consistent with the extinction spectra of silver film on phosphor particles (Figure 3.6B). For films thicker than 10 nm

(more than the optical penetration depth of silver), the silver largely behaves as a lossy mirror, and the attenuation effect saturates.

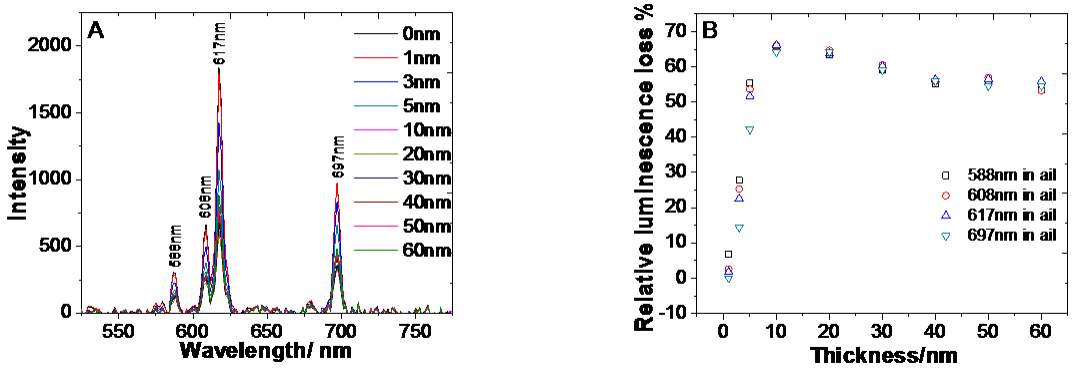

Figure 3.7 (A) Luminescent spectra of Gd_2O_2S:Eu phosphor coated with different thickness of silver film. (B) Relative luminescence loss $((I_{uncoated}-I_{coated})/I_{uncoated}\times 100\%)$ varies with different thickness of silver. Reproduced from Ref. 123 with permission from the Royal Society of Chemistry.

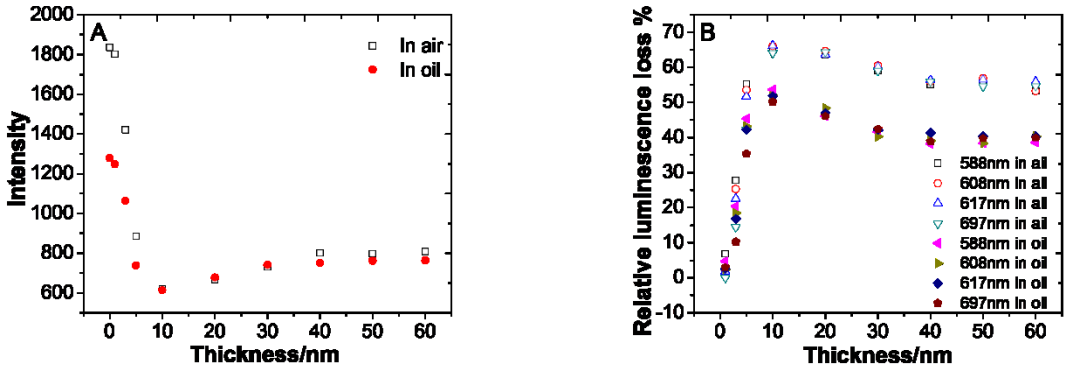

Figure 3.8 (A) Luminescent intensity at 617 nm in air and oil. (B) Relative luminescent intensity loss $((I_{uncoated}-I_{coated})/I_{uncoated}\times 100\%)$ in air and oil. Reproduced from Ref. 123 with permission from the Royal Society of Chemistry.

The above experiments indicated that absorption was the most likely explanation for the silver attenuation because the attenuation showed a spectra dependence that was consistent with the silver nanoparticle extinction spectrum. However, since the silver coating was beneath the phosphors, and the camera and spectrometer detected light emitted through the top of the particles, the silver must absorb light that would otherwise be reflected from the bottom of the particles (e.g. due to refractive index mismatches). The refractive index of Gd_2O_2S:Eu is between 2.1 and 2.3 RIU.[102] Assuming an intermediate refractive index of 2.2, the phosphor/air interface has a critical angle of 27º which corresponds to reflection from a solid angle of $1.82\pi^2$, or 91% of an incident angles. In addition, 14% of normally incident light reflected at the Gd_2O_2S/air interface. For comparison, the critical angle for the phosphor/double-sided sticky tape interface is 42º, assuming a refractive index of 1.5 for the tape, this corresponds to reflection from a solid angle of $1.54\pi^2$ or 77% of incident angles; the normal reflection coefficient is 3.6%.

Therefore, most of the light is reflected once or more and most of light is emitted through the top of phosphor/tape interface. This hypothesis explains why a silver coating below affects the light above. It also explains why placing a mirror below the phosphors increases the luminescence, but by less than a factor of 2 (see Figure 3.1B). To further test this hypothesis, we incubated the phosphor film in microscope immersion oil with a refractive index of 1.518 RIU (see Figure 3.8). The overall intensity of light collected through the top of the film decreased, consistent with a decrease in reflection from the bottom surface (Figure 3.8A). In addition, the relative effect of attenuation from silver absorption was less significant after adding oil which is consistent with a reduced amount of internal reflection (Figure 3.8B). These results support the internal reflection hypothesis. Internal reflection increases the effective absorption path length and enhances local absorption from nanoparticles and dyes on the surface which is adventurous for measuring small changes in absorbance. Furthermore, the particles can be designed to detect changes in local refractive index, a feature which can be employed to observe label-free protein binding and polymer degradation.

Dissolution of silver nano-film in H_2O_2

Hydrogen peroxide plays a significant role in cell biology. It is a messenger molecule for a wide variety of processes including cell development and programmed cell death.[103-104] It is produced by macrophages to destroy pathogens and also serves as an inflammatory marker. H_2O_2 is also produced in many aerobic processes and enzymatic reactions. These reactions are often used in electrochemical analysis, for example glucose

is routinely detected by electrochemically measuring the amount of H_2O_2 produced in the presence of glucose oxidase[105] and peroxidise enzymes.

Silver is an important antimicrobrial agent which is found in a wide variety of cosmetics and textiles, and has been proposed as an antimicrobial agent for implanted medical devices.[106-107] Recently there have been several studies of the reaction rate of Ag with H_2O_2 in different pH and temperature conditions. The overall reaction is shown below.[108-109] The reaction is sensitive to concentrations of salts and enzyme, for example Liu et al. showed an increase in reaction rate with decrease in pH, and proposed a hydroxyl radical intermediate (OH•),[108] while Ho et al. found an increase in reaction rate with increasing pH (due to reaction of HO_2^-) and no hydroxyl intermediate.[109] A technique capable of measuring in situ silver dissolution would therefore be useful.

$$2Ag_{(s)} + H_2O_2 \rightarrow 2Ag^+_{(aq)} + 2OH^- \text{ (see ref.27, 28)}$$

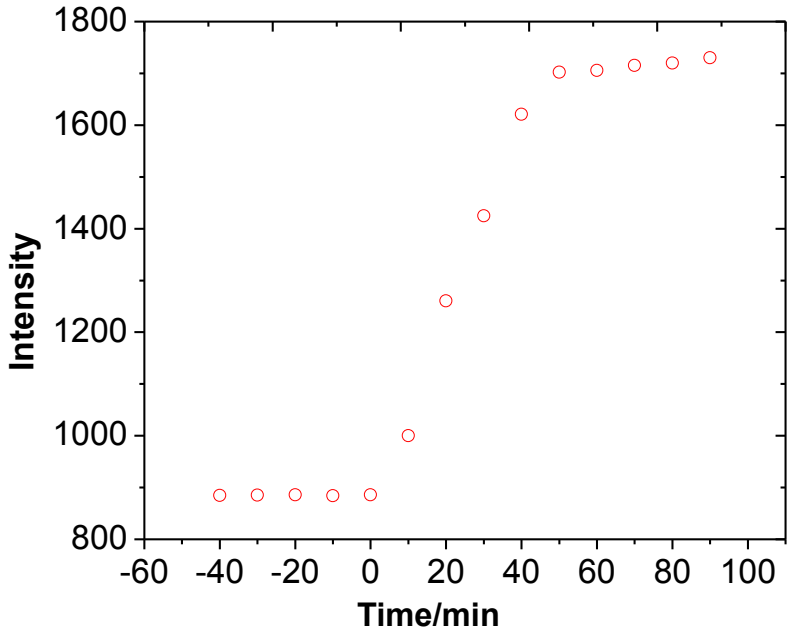

Figure 3.9 Luminescent intensity at 617 nm as a function of time during silver dissolution in 1 mM H_2O_2. Reproduced from Ref. 123 with permission from the Royal Society of Chemistry.

To study the dissolution of a silver island film in H_2O_2, 5 nm of silver was vapour deposited upon a Gd_2O_2S:Eu phosphor film, and the luminescent spectra were recorded in time during dissolution in a 1 mM H_2O_2 aqueous solution. The dissolution of the silver was indicated by the increase in luminescent intensity. As shown in Figure 3.9, after the silver film dissolved in H_2O_2, the luminescent intensity recovered to normal intensity within experimental error from sample to sample variation. Although 1 mM H_2O_2 concentration is a very high level for physiological conditions,[110-111] the dissolution was relatively rapid (30 min), compared to a few weeks in physiological conditions. For

example, assuming that rate is proportional to concentration,[108-109] 30 minutes at 1 mM corresponds to a 7 μM concentration dissolving in 3 days or 700 nM over one month. In addition, the physiological rate may be different due to changes in pH, increased temperature (37 ºC instead of 23 ºC), extracellular components including chloride ions and metal binding enzymes, adsorption of protective proteins, and mechanical abrasion. The ability to tune the silver thickness and location presents a promising method to study dissolution kinetics *in vivo*.

Imaging silver dissolution through tissue

To detect low concentrations of H_2O_2 (1 mM) in thick tissue with high spatial resolution, we use a narrow X-ray beam to excite the phosphor film. We selected a 5 nm thick silver film on Gd_2O_2S:Eu since the luminescent reduction is enough to distinguish (Figure 3.8A) and the small particle size reduces the time required to dissolve the silver (Figure 3.9). The silver coated phosphor film was incubated in 1 mM H_2O_2 solution (100 μl of 30% (w/w %) H_2O_2 solution was added in 1000 ml DI water (pH 5.5)) at room temperature for 3h. We also deposited a 5 nm thick strip of gold as a chemically inert control. Figure 3.10 shows that the 5 nm gold film reduces the intensity more than the 5 nm silver film. This intensity difference and the stability of gold in physiological conditions make the gold film a good reference and fiduciary marker.

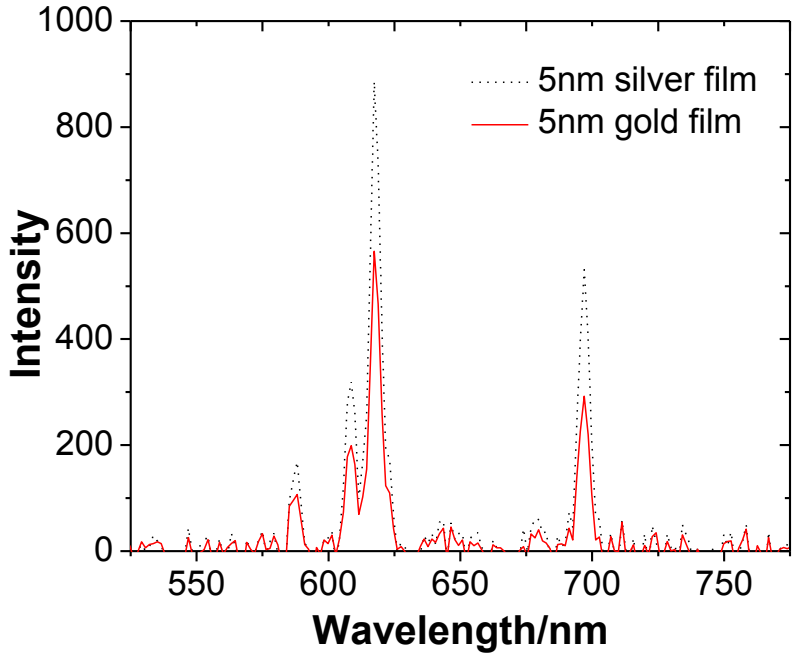

Figure 3.10 Luminescent spectra of phosphor film with 5 nm of silver and 5 nm of gold film. Reproduced from Ref. 123 with permission from the Royal Society of Chemistry.

In order to image local changes in silver absorbance, we masked some regions of a silver film with double sided sticky tape prior to exposure to 1 mM H_2O_2. Figure 3.11A is a photograph of a phosphor film coated by a strip of silver 5 nm thick and 7.4 mm wide as well as a strip of vapour-deposited gold, 5 nm thick and 2.3 mm wide. Two regions of the silver film were masked with thin strips of tape so that only a strip in the center was unprotected. The sample was plasma etched for 5 min in air plasma to make all regions hydrophilic. The sample was then incubated in H_2O_2 for 3 hr to dissolve the unprotected section of silver film (See Figure 3.11D). A one dimensional XEOL image was acquired

from the film before and after silver dissolution, and the XEOL was performed with and without placing a 1 cm thick section of pork tissue above the film. The H_2O_2 etched area can be clearly identified by the increased luminescence, while it can be distinguished from the gold coated region with lower XEOL intensity. The gold coated region was unaffected by H_2O_2 providing a control strip. Most importantly, the resolution of the XEOL scan was hardly affected by the 1 cm of pork demonstrating that high resolution imaging through thick tissue.

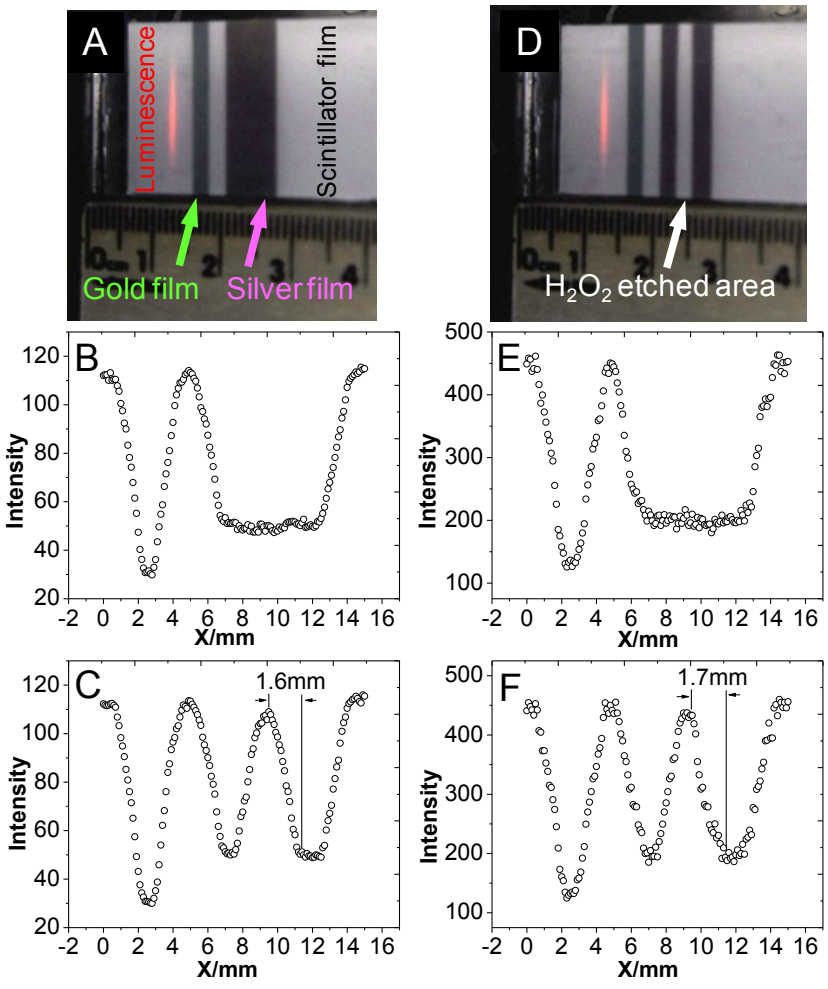

Figure 3.11 (A), (D) Images of gold and silver coated phosphor film before and after H_2O_2 etching. (B), (E) Intensity of red light scanned at different positions with/without 10 mm of tissue before H_2O_2 etching. (C), (F) Intensity of red light scanned at different positions with/without 10 mm of tissue after H_2O_2 etching. The resolution through 10 mm tissue is 1.7 mm. Reproduced from Ref. 123 with permission from the Royal Society of Chemistry.

Conclusion

We have extended the XEOL technique to tissue imaging where it offers a combination of high spatial resolution (limited by the X-ray beam width) and high sensitivity optical detection. The high spatial resolution is competitive with conventional X-ray imaging but offers the ability to detect nanometer thick metal coatings and small changes in local absorption near indicator particles. Proof-of-principle involved detecting silver and gold nanoparticle patterns through 10 mm of pork as well as monitoring silver dissolution in H_2O_2, but the technique is general to a wide variety of indicator dyes and nanoparticle labels. Interestingly, the high refractive index of the Gd_2O_2S phosphor increased the effective attenuation path length around the particle and also provided a method for label free detection of changes in local refractive index.

In future, the instrumentation can be enhanced using a narrower X-ray beam for higher spatial resolution imaging and using a multiple axis stage for two and three dimensional imaging. In addition, higher sensitivity and more rapid signal acquisition can be realized with a modulated X-ray source and a photomultiplier tube with lock-in signal amplification (see Figure 3.4). An important application will be the non-invasive

detection of localized implant associated infection. We plan to use the technique to study bacterial products and inflammation markers, including hydrogen peroxide, oxygen, pH,[112] quorum sensing molecules, and bacterial stains. Multiple analytes may be detected on spatially patterned sensors, as shown above using silver and gold nanoparticle patterns (see Figure 3.11). Alternatively, spectrally multiplexed sensing is possible using multiple rare-earth doped phosphors with narrow spectral peaks. Relatively robust and long-lived sensors can be developed using inorganic materials, such as silver nanoparticles and hydroxyapatite, to monitor *in situ* chemical reactions through associated changes in local absorption and refractive index. Overall, scanning XEOL provides new capabilities for chemical analysis in tissue and turbid media.

Experimental Section

Materials

Hydrogen peroxide aqueous solution (30% w/w) was purchased from BDH Chemicals Ltd (Poole, Dorset, UK). Europium doped Gadolinium oxysulfide (Gd_2O_2S:Eu) was purchased from Phosphor Technology Ltd. (Stevenage, UK) and it contained microparticles that ranged in size from 2~15 μm with a nominal diameter of 8 μm. Silver wire (>99.99%, 1 mm diam.) and gold wire (99.999%, 1 mm diam.) were purchased from Sigma-Aldrich (St Louis, MO, USA). Double sided tape (3M 666, 1×1296 Inch) was purchased from 3M Company (St. Paul, MN, USA). Cover glass (No. 0, 24×60 mm) was purchased from Electron Microscopy Sciences (Fort Washington, PA, USA). Immersion oil was purchased from Leica Microsystems

(Wetzlar, Germany). Deionized (DI) water was purchased from EMD Chemicals Inc. (Gibbstown, NJ, USA). Pork was purchased from Ingles Market, Inc. (Asheville, NC, USA). Reynolds Wrap Quality Aluminum Foil was purchased from Consumer Products Division of Reynolds Metal (Richmond, VA, USA). All chemicals were used as received without further purification.

Preparation of the Gd_2O_2S:Eu phosphor film and coated with silver and gold nano-film

A 24×60 mm cover glass was covered with double sided tape. A single layer of particles was attached to the surface of double-sided tapped by spreading 0.5 g europium doped gadolinium oxysulfide (Gd_2O_2S:Eu) powder on top of the tape. Excess particles were removed by rinsing in DI water, followed by drying at room temperature for 2hr. The sample was plasma etched for 5 min in a Harrick plasma etcher at media power in air plasma to make the surface hydrophilic. Finally the sample was coated with silver or gold using thermal vapour deposition.

Nano-film of silver and gold coating and dissolution of the silver in hydrogen peroxide solution

The Gd_2O_2S:Eu film was coated with a thin layer of gold or silver. The metal was deposited using thermal vapour deposition (Auto 360 vacuum coater/thermal evaporator, Edwards, West Sussex, UK) under high vacuum ($< 5 \times 10^{-6}$ Torr). The thickness of the metal was controlled using a shutter and measured with a quartz crystal microbalance. In order to study the rate of silver dissolution in H_2O_2, a Gd_2O_2S:Eu film was prepared with

a 5 nm thick average coating of silver. The film was then incubated in 1 mM H_2O_2 and the sample was taken out for luminescent spectra in every ten minutes. In order to selectively dissolve only a portion of silver in H_2O_2, a 5 nm silver film was masked with two strips of tape leaving an unmasked region between the two strips. The sample was then incubated in 1 mM H_2O_2 for 3 hr to dissolve the unmasked region.

Instrumentation

An X-ray diffractometer (Rigaku; MiniFlex, Cu Kα) was used as an X-ray source. For X-ray phosphor luminescence, the X-ray diffractometer was operated with tube voltage of 30 kV and tube current of 15 mA. The sample was mounted on a stepper motor stage (MTS 50, Thorlabs, Inc., Newton, NJ, USA) which was controlled by a program written in Labview (National Instruments, Austin, TX, USA). To measure lifetime, the X-ray irradiation was modulated by an optical beam chopper equipped with a 1 mm thick aluminium chopper wheel (Stanford Research Systems, model SR540, CA). The intensity of the emitted light was measured with a PMT (R955, Hamamatsu Photonics, Japan) connected to Tektronix TDX 2004B Oscilloscope. The signal acquisition was triggered off of the chopper wheel photodiode. Data was transferred from the oscilloscope using an interactive measurement software v1.2 (NI SignalExpress Tektronix edition). The PMT was placed over a 0.5 cm thick piece of glass to block the small amount of scattered X-ray photons while passing the visible luminescence. Scanning electron microscopy (SEM) was performed on a SU6600 microscope operated at 20 kV. Luminescent and extinction spectra were acquired at room temperature with a FPC-400-0.22-1.5-UV fiber (Thor Labs) coupled photodiode array spectrometer (BRC741E-02 BWTEK Inc, Newark,

DE, USA). Luminescent images were taken with a Nikon D90 digital camera with a 67 mm diameter lens at 50 mm FL and a macro lens adaptor. To increase the captured luminescence, a 3×16 cm piece of aluminum foil was placed beneath the phosphor film. All the parameters of the camera were controlled by the software of Camera Control Pro2 (Nikon Instruments Inc., Melville, NY, USA). All images were analyzed using Matlab R2009b.

CHAPTTER FOUR

IV. MONITORING PH-TRIGGERED DRUG RELEASE FROM RADIOLUMINESCENT NANOCAPSULES WITH X-RAY EXCITED OPTICAL LUMINESCENCE

Introduction

Doxorubicin (DOX) is a chemotherapy drug used to treat a wide range of cancers. However, its serious adverse effects such as suppression of hemaropoiesis, gastrointestinal and cardiac toxicity limit its applications.[113-114] It is crucial to control the concentration of doxorubicin specifically in the blood circulation, normal tissues, and tumor tissues. Unfortunately, DOX clears rapidly from circulation (circulation half-life of < 5 min)[115] which makes it difficult to specifically target tumor cells using free drug. A pH- responsive controlled system for DOX could address this issue by releasing drugs into the blood only gradually, but rapidly release drugs after endocytosis in acidic tumor lysosomes and endosomes. The particles could be targeted to tumors via enhanced permeability and retention (EPR) effect and by functionalizing the nanoparticle surface with appropriate antibodies or other targeting molecules. In 2005, Lee *et al.* reported pH-sensitive micelles as carriers for DOX to enhanced tumor specificity and endosome disruption property on the carrier.[116-117] Recently, mesoporous silica has gained attention as drug storage and release hosts due to their textural properties and easily modified surface.[118-121] Zhu and co-workers reported pH-controlled delivery of DOX to cancer cells based on small mesoporous carbon nanospheres. In our previous work, a ratiometric pH sensor based on the ratio of certain radioluminesence peaks of terbium doped gadolinium oxysulfide (Gd_2O_2S:Tb) was developed.[112] The ratio of luminescent spectral

peaks is independent of the luminescence intensity which provides a promising method to detect chemicals in tissue with high spatial resolution with a narrow scanning X-ray beam and selectively exiting the phosphor film by taking advantage of the excellent penetration of X-ray beam in tissue and wide range of availability of X-ray phosphors.[122] Xing group and we found that changes in spectrum and intensity can be imaged through tissue at a resolution dictated by the X-ray beam,[54-55, 123] and we have demonstrated submilimeter imaging through 1 cm of chicken breast.[112, 124] We also demonstrated that the XEOL spectrum of hollow Gd_2O_3:Eu nanoparticles is greatly reduced by the presence of an iron oxide core,[125] and the luminescence of solid Gd_2O_2S:Eu particles is modulated by the absorption spectrum of silver nanoparticles on the phosphor surface.[123] Based upon these results, we hypothesized that we could monitor release of dyes and optically absorbing drugs from the core of nanocapsules.

In this work, we synthesize rare-earth (Tb, Eu) doped Gd_2O_2S based radioluminescent capsules as a drug nanocarrier and drug release monitor. Compared with gadolinium oxide doped with Eu, Tb and Eu doped gadolinium oxysulfide possesses higher photo conversion efficiency (60,000 visible photons/MeV for Gd_2O_2S:Tb, and Gd_2O_2S:Eu, 40,000 visible photons/MeV for Gd_2O_3:Eu).[124] Their bright radioluminescence (Figure 4.1) can be used to track the delivered drug (DOX) and monitor the drug release process. Meanwhile, these capsules serve as good T_2-weighted MRI contrast agent which can be used as a complementary imaging mode for X-ray functional imaging.[126]

Results and discussion

Particle shape plays a crucial role in the application of drug delivery systems.[127-128] Some previous studies on particles with high aspect ratio (e. g. nanorod, nanorice) showed that those particles (> 500 nm in length) with high aspect ratio have slower clearance rate compared with particles with low aspect ratio (e.g. spherical particles) in the application of drug delivery systems.[129-130] To demonstrate the shape effect on the clearance rate for the future study, we chose ellipsoidal hollow silica nanorice as templates to synthesize monodispersed ellipsoidal nanocapsules. In addition, by varying the synthesis condition of template,[131-133] the length of these nanocapsules are can be tuned from 20 nm to 600 nm and the aspect ratio can be adjusted from spheres to prolate spheroids. In order to obtain monodispersed silica nanoshells, as shown in Figure 4.2, monodispersed hematite nanorice is first prepared, then treated through a modified Stöber procedure to form a thin silica shell. Finally the hematite core was removed by etching in 0.5 M oxalic acid for 17 h. The uniform and negatively charged silica shell were then coated with a layer of positive charged $Gd_2O(CO_3)_2 \cdot H_2O$ doped with terbium (Tb^{3+}, 2.4% mol) or europium (Eu^{3+}, 5.1% mol) through a homogeneous precipitation method from gadolinium, europium nitrate. This method employs an electrostatic interaction between negative charged silica shell and positive charged radioluminescent shell.[125] After heat treatment at 600 °C for 1 h, the amorphous $Gd_2O(CO_3)_2 \cdot H_2O$ layer transformed into Gd_2O_3. The above product was treated by sulphur gas with argon flow at 900 °C for 1h to convert the Gd_2O_3 to Gd_2O_2S. The obtained nanoparticles was re-heated at 400 °C in the

air for 1h and incubated in boiling water for 2 h to remove the residue of sulphur and gadolinium sulphide.

TEM images in Figure 4.3A show monodispersed spindle-shaped iron oxide seeds. Figure 4.3B represents the intact silica shell after the iron oxide core was removed by dissolving in oxalic acid. The SEM image in Figure 4.3C and narrow size distribution in Figure 4.3D indicate the monondispersed nanocapsules were obtained successfully with an average length of 420 +/-20 nm and width of 130 nm +/-15 nm. The nanocapsules possess a 10 nm thick inner silica shell and a 25 nm thick outer Gd_2O_2S:Tb radioluminescent shell (Figure 4.3F) with porous morphology (Figure 4.3E, F and Figure 4.4,). The pores are irregular in shape, with an average diameter of (8.5 +/- 2 nm). These visible pores in the shell (Gd_2O_2S:Tb) of the nanocapsules likely facilitate drug loading and releasing. Crystal structure and composition of these nanocapsules were characterized by powder X-ray diffraction (XRD) and the host is shown as hexagonal phase of Gd_2O_2S according to the data of JCPDS card no. 26-1422 (Figure 4.5). Gd_2O_2S:Eu with similar aspect ratio were also synthesized by the same silica nanotemplate (Figure 4.6). The tunable size range and the morphology make these nanocapsules promising as drug carriers. In order to apply these nanocapsules in biological applications, the stability of the nanocapsules was tested in 0.3 % (v%) acetic acid (pH ~3.0). The SEM images in Figure 4.7 show no discernible dissolution indicating that the nanocapsules are very stable under pH 3 at 37 °C even after 24 hr. The cell viability of our X-ray phosphors on MCF-7 breast cancer cells is also tested and it's

shown that cell viability is greater than 90% when the concentration of Gd_2O_2S:Tb and Gd_2O_2S:Eu is as high as 250 μg/ml, after incubation for 24 h (Figure 4.8).

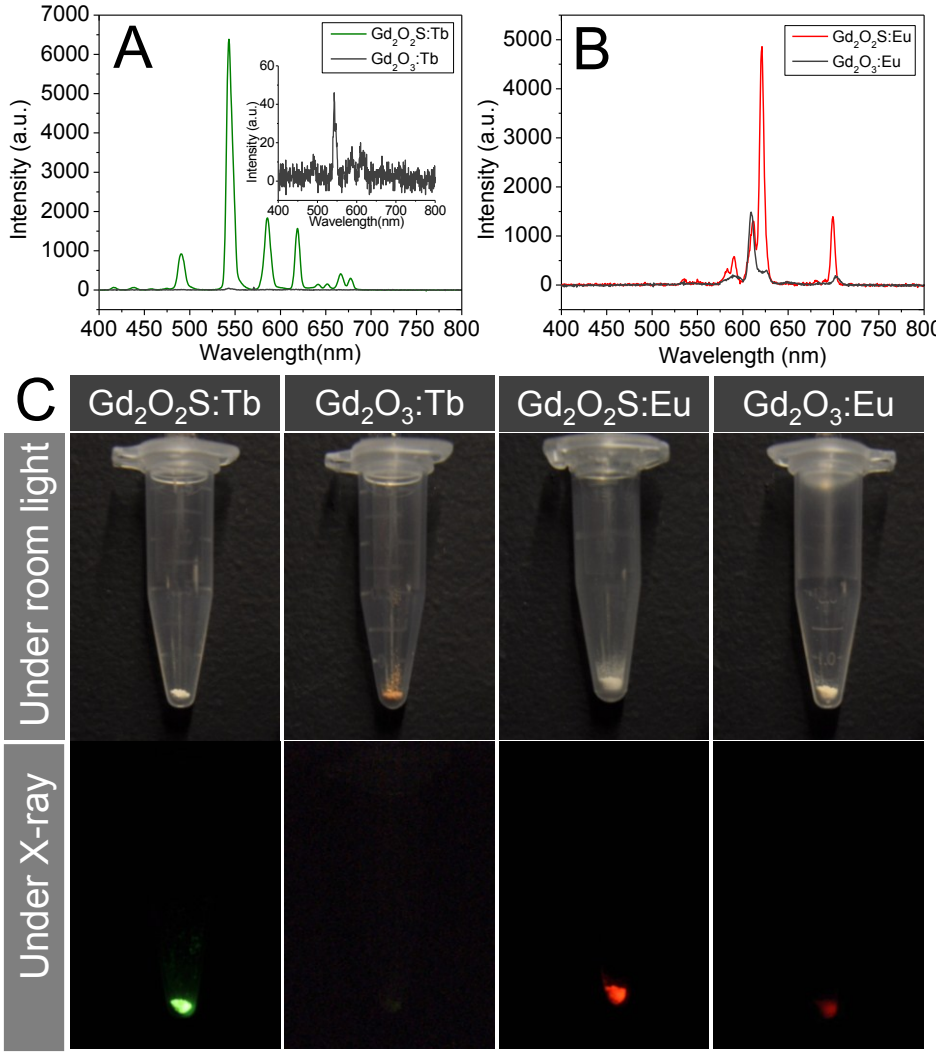

Figure 4.1 X-ray luminescence of (A) Gd_2O_2S:Tb and Gd_2O_3:Tb nanocapsules, inserted figure shows the spectrum of Gd_2O_3:Tb in high magnification, (B) Gd_2O_2S:Eu and Gd_2O_3:Eu nanocapsules. Photograph of Gd_2O_2S:Tb, Gd_2O_3:Tb, Gd_2O_2S:Eu, and

Gd_2O_3:Eu under X-ray (C). Reprinted with permission from ref. 126. Copyright 2012 American Chemical Society

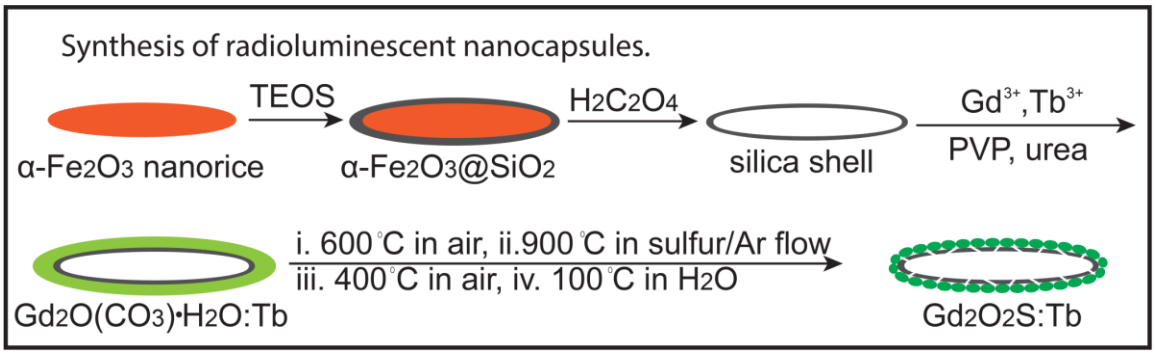

Figure 4.2 Schematic illustration of the synthesis of radioluminescent nanocapsules. Reprinted with permission from ref. 126. Copyright 2012 American Chemical Society.

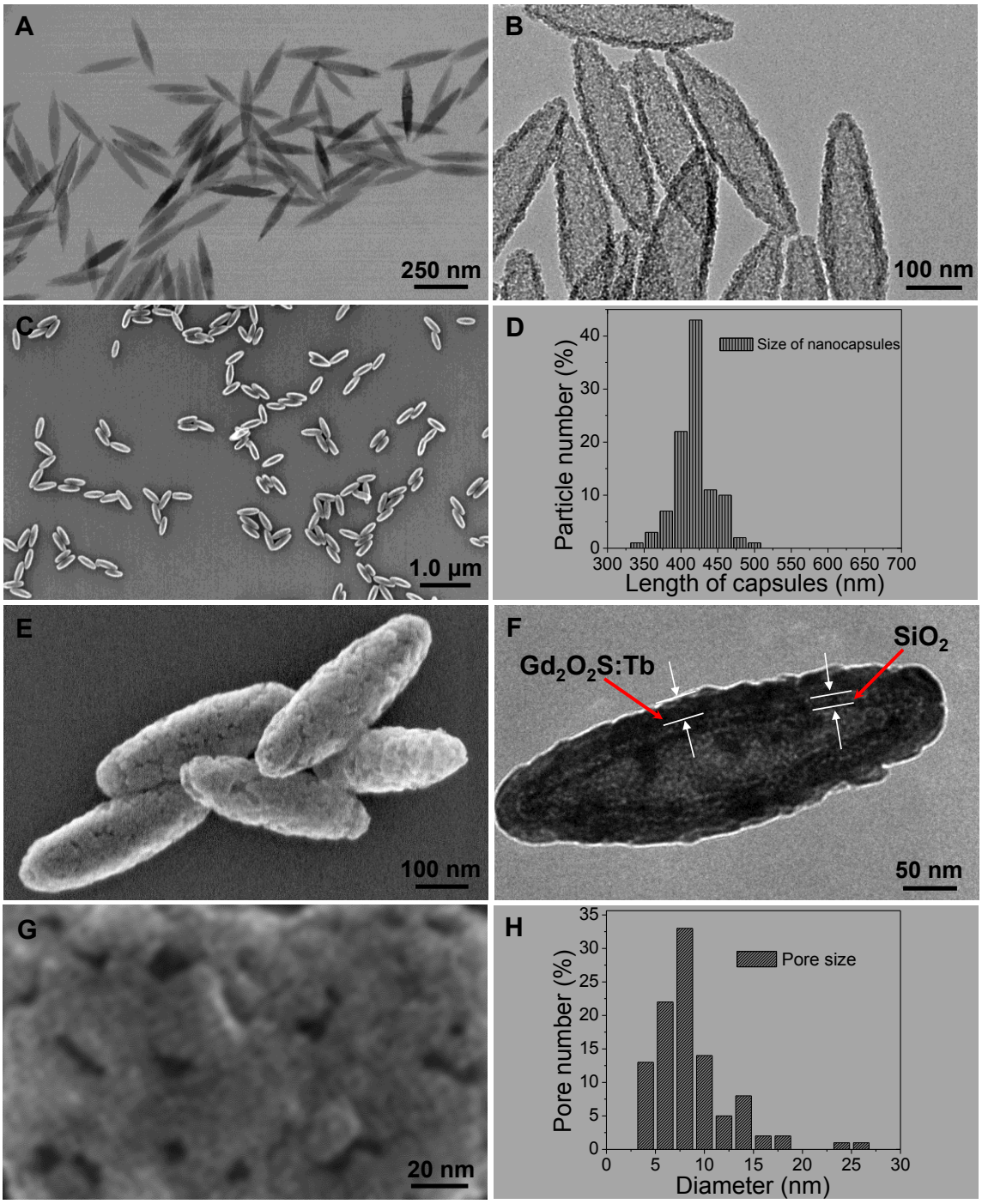

Figure 4.3 (A) TEM image of monodispersed iron oxide seeds, (B) TEM image of hollow silica shell after removing iron oxide core, (C) SEM image of monodispersed radioluminescent nanocapsule (Gd_2O_2S:Tb (Tb/Gd=2.4% mol), (D) Size distribution of

the nanocapsules, (E) High magnification SEM image of nanocapsule, (F) TEM image of the nanocapsule, (G) High magnification SEM image of surface of a nanocapsule, (H) pore size distribution from 100 nanocapsules. Reprinted with permission from ref. 126. Copyright 2012 American Chemical Society.

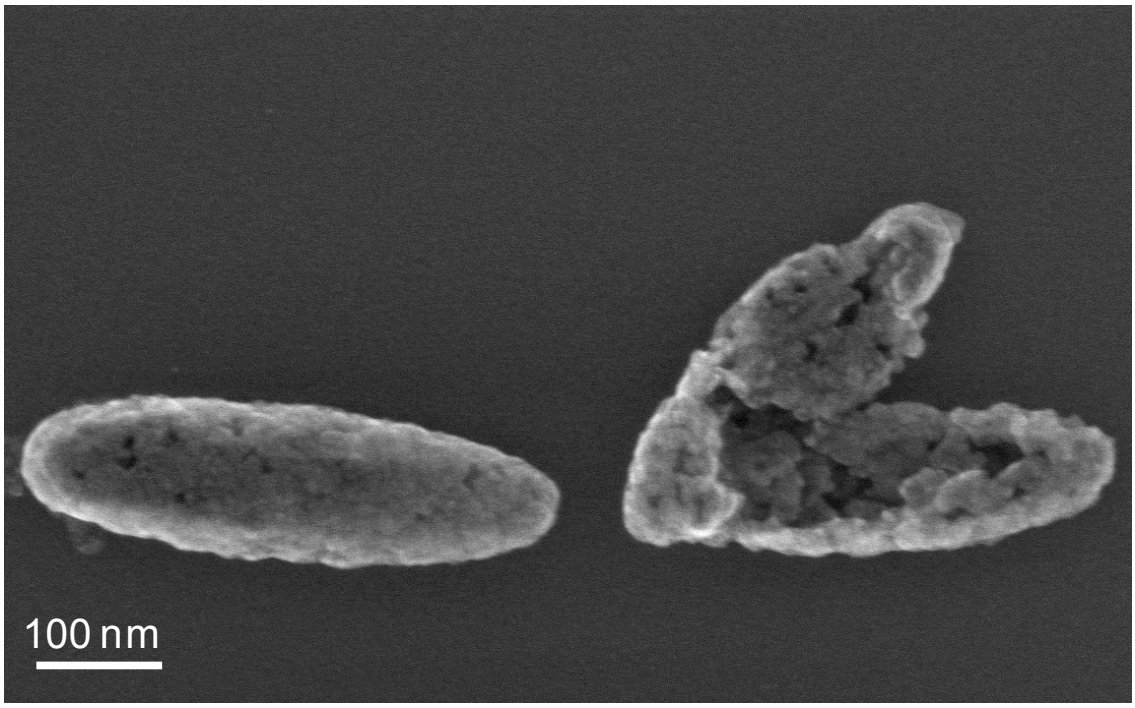

Figure 4.4 SEM image showing the porous and hollow nanocapsules (Gd_2O_2S:Tb). Reprinted with permission from ref. 126. Copyright 2012 American Chemical Society.

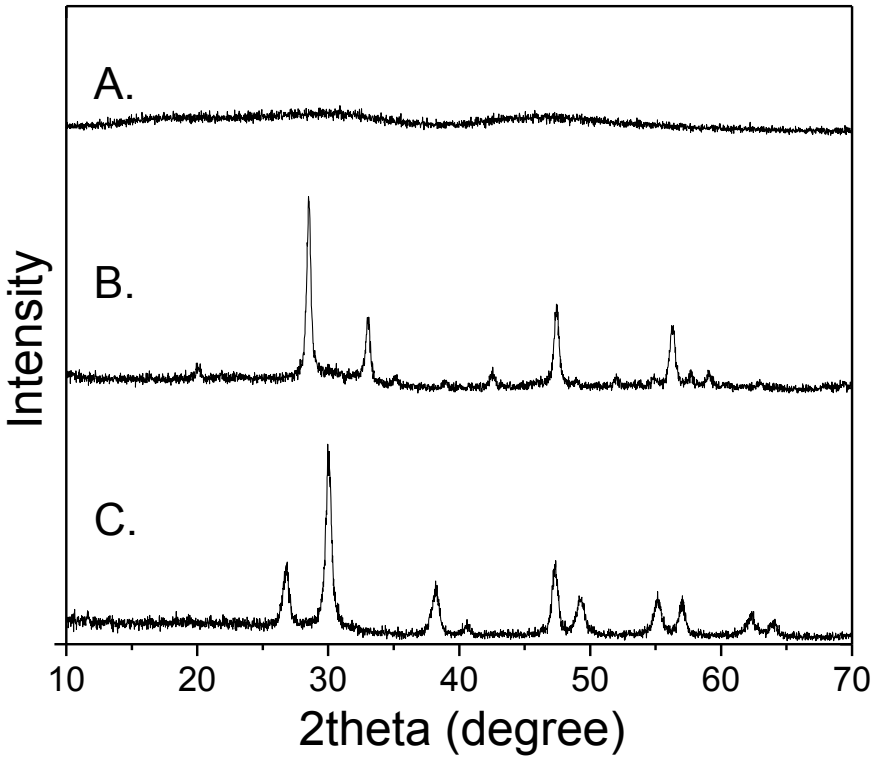

Figure 4.5 XRD patterns of (A) $Gd_2O(CO_3)_2 \cdot H_2O$:Tb, (B) Gd_2O_3:Tb, (C) Gd_2O_2S:Tb. Reprinted with permission from ref. 126. Copyright 2012 American Chemical Society

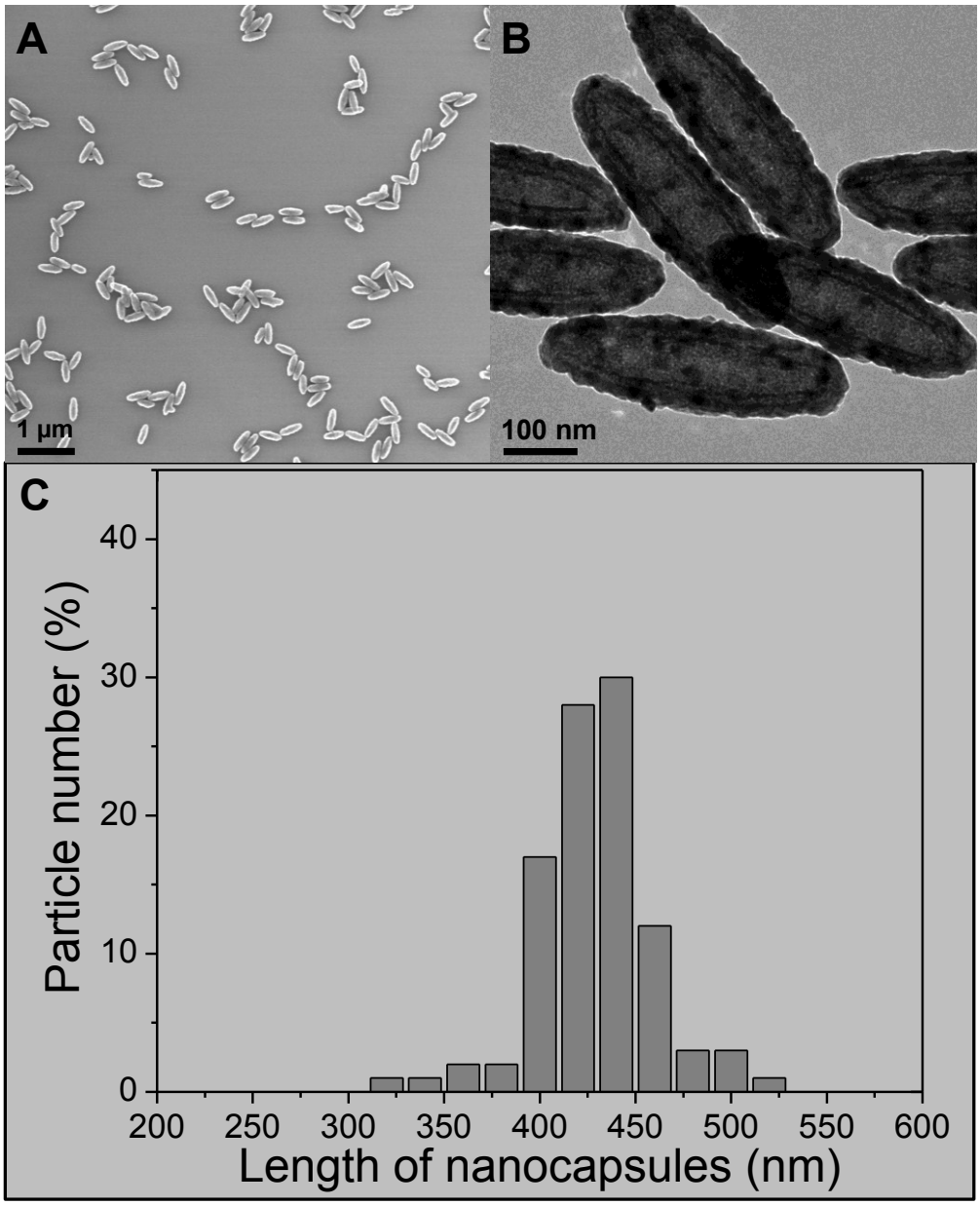

Figure 4.6 SEM (A) and TEM (B) images of nanocapsule (Gd_2O_2S:Eu, Eu/Gd=5.1% mol), (C) size distribution of nanocapsules (Gd_2O_2S:Eu). Reprinted with permission from ref. 126. Copyright 2012 American Chemical Society.

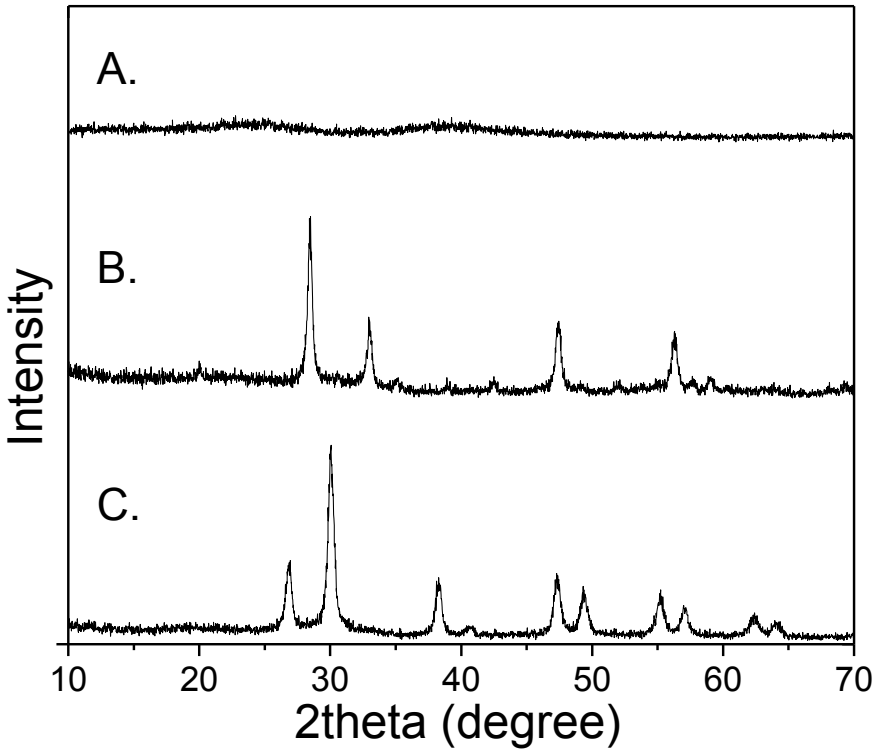

Figure 4.7 XRD patterns of (A) $Gd_2O(CO_3)_2 \cdot H_2O$:Eu, (B) Gd_2O_3:Eu, (C) Gd_2O_2S:Eu. Reprinted with permission from ref. 126. Copyright 2012 American Chemical Society.

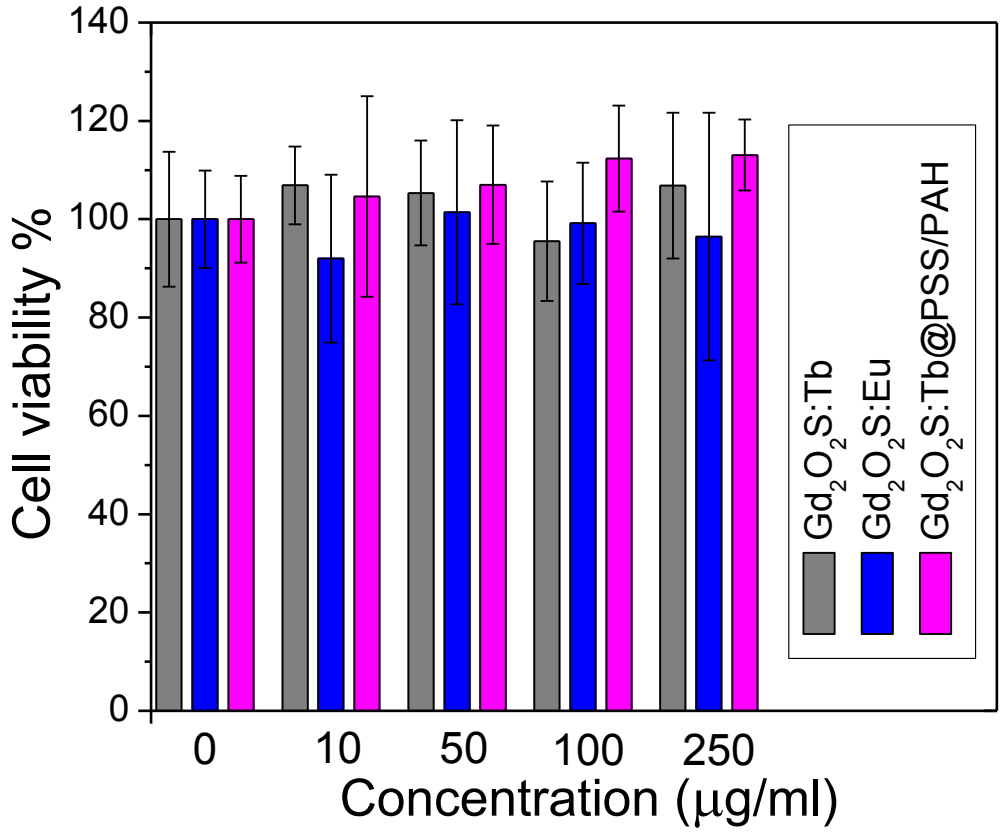

Figure 4.8 Cytotoxicity test of nanocapsules (Gd_2O_2S:Tb and Gd_2O_2S:Eu) and PSS/PAH multilayers coated nanocapsules (Gd_2O_2S:Tb). Reprinted with permission from ref. 126. Copyright 2012 American Chemical Society.

The radioluminescence spectra of nanocapsules (Gd_2O_2S:Tb, Eu) are presented in Figure 4.9. The radioluminescence mechanism involves the generation of electron-hole pairs in the host lattice following X-ray absorption. These electron-hole pairs then excite Tb^{3+} and Eu^{3+} centers which emit visible and near infrared light. The conversion

efficiency is 60,000-70,000 visible photons/MeV X-ray photon in bulk Gd_2O_2S:Eu, corresponding to an energy efficiency of 15%.[22, 36, 134] The narrow luminescent peaks of Gd_2O_2S:Tb are attributed to the transitions from the $^5D_4$ excited-state to the ^7F_J (J=6, 5, 4, 3, 2, 1, 0) ground states of the Tb^{3+} ion. The $^5D_4 \rightarrow {}^7F_5$ transition at 544 nm is the most prominent group. The $^5D_{0,1} \rightarrow {}^7F_J$ (J=0, 1, 2, 4) transition lines of the Eu^{3+} ions generate the intense peak at 590, 612, 620, 720 nm. The strongest red emission which splits into two peaks at 621 and 612 nm arises from the forced electric-dipole $^5D_0 \rightarrow {}^7F_2$ transitions of the Eu^{3+} ions. These nanocapsules displayed similar fluorescence spectra under blue excitation light (460-495 nm) (Figure 4.10). However, blue light does not penetrate as deeply into tissue as X-rays, and unlike X-rays, does not stay collimated or focused which dramatically reduces image resolution.

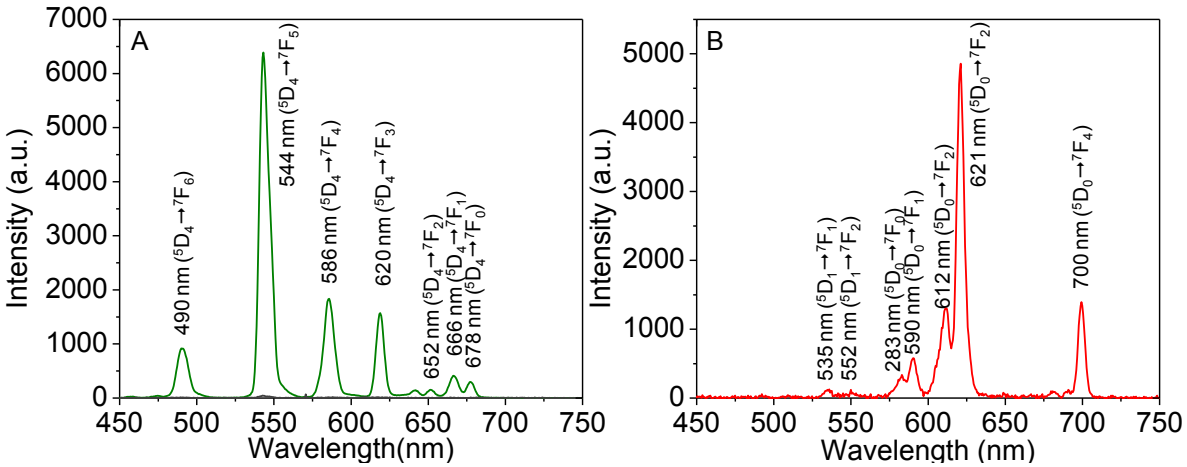

Figure 4.9 X-ray luminescence of nanocapsules. (A) Gd_2O_2S:Tb, (B) Gd_2O_2S:Eu. Reprinted with permission from ref. 126. Copyright 2012 American Chemical Society.

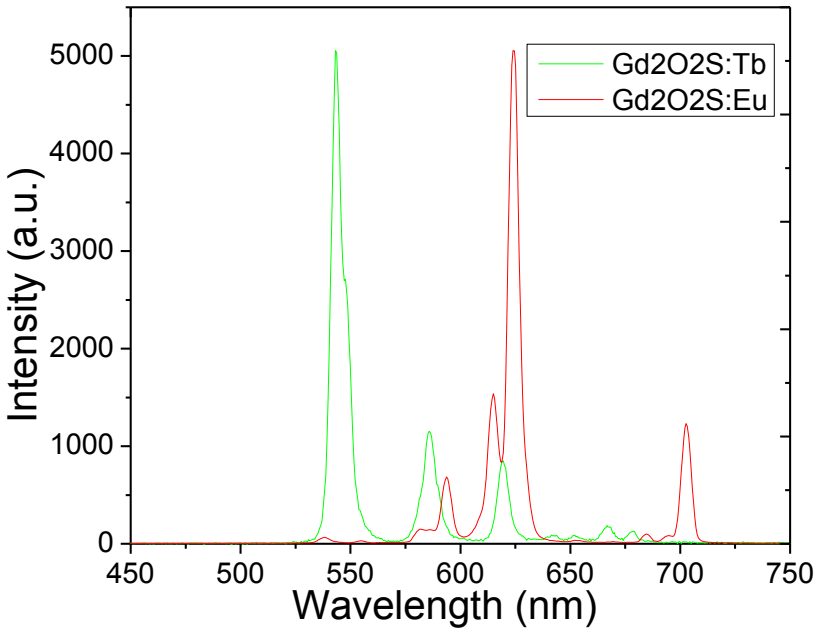

Figure 4.10 Fluorescence spectra of nanocapsules (Gd_2O_2S:Tb and Gd_2O_2S:Eu) excited by 460 to 495 nm light. Reprinted with permission from ref. 126. Copyright 2012 American Chemical Society.

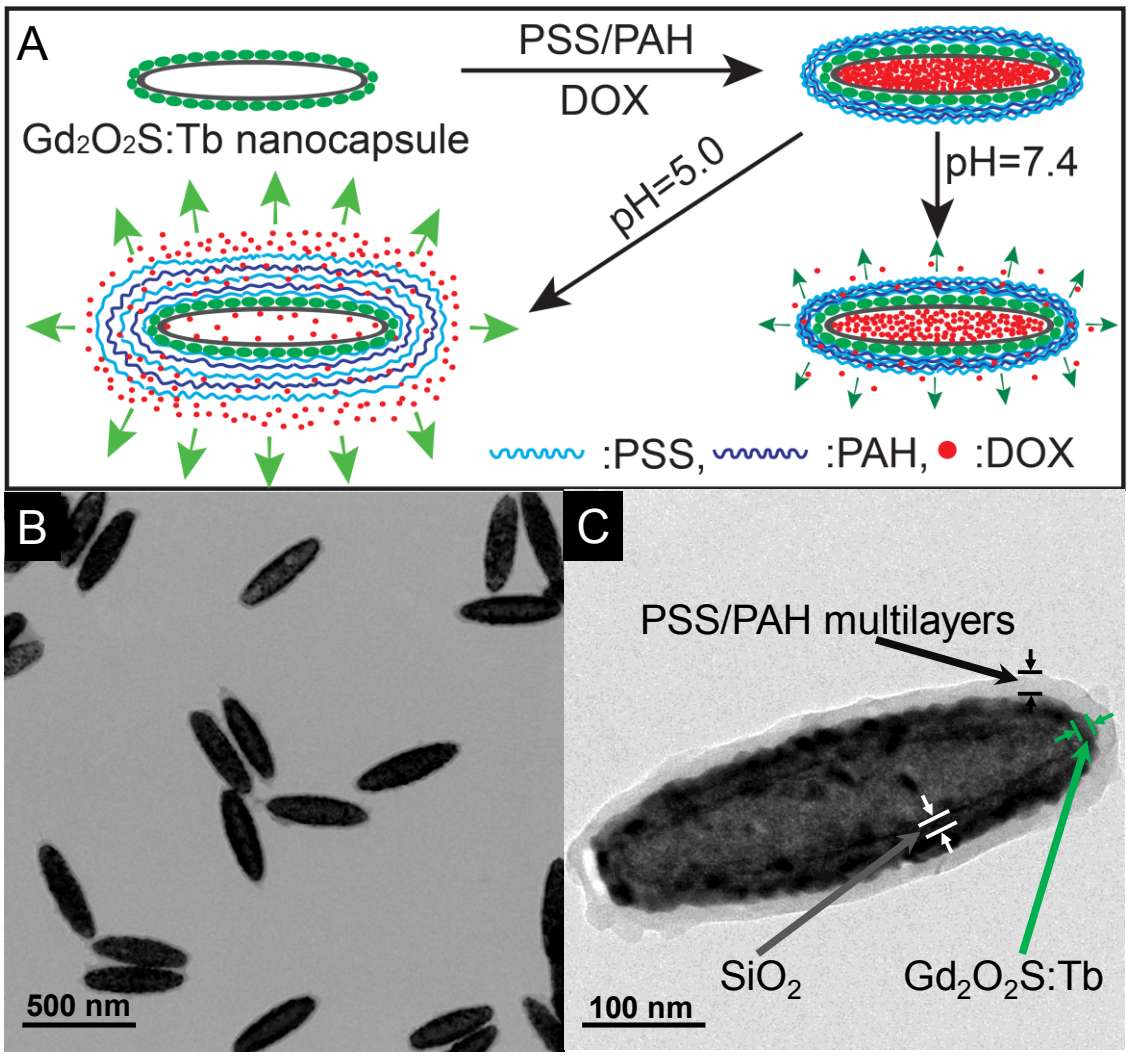

Figure 4.11 (A) schematic illustration of the synthesis of DOX@Gd_2O_2S:Tb@PSS/PAH and pH-responsive release of DOX. Low magnification (B) and high magnification (C) TEM image of DOX@Gd_2O_2S:Tb@PSS/PAH. Reprinted with permission from ref. 126. Copyright 2012 American Chemical Society.

Styrenesulfonate sodium (PSS) and poly(allylamine hydrochloride) (PAH) are widely used polyelectrolytes in pH-controlled release systems.[135-138] In order to create a stimuli-responsive system for DOX, our X-ray luminescent nanocapsules coated with

eight layers of negative charged PSS and seven layers of positive charged PAH to encapsulate DOX with layer by layer assembly (Figure 4.11; the particle is denoted as DOX@Gd_2O_2S:Tb@PSS/PAH). Due to the surface of our nanocapsules are positive charged (+14.9 mV, Figure 4.12), the first layer of polyelectrolyte coated on nanocapsules is PSS. After the layer by layer coating, the nanocapsules are coated by an average of 30 nm thick polyelectrolyte with a layer of PSS on the surface. Cell viability test indicates that the empty Gd_2O_2S:Tb nanocapsules coated with PSS/PAH multilayers show no significant toxicity to a concentration of at least 250 μg/ml, the highest concentration measured (Figure 4.8). In order to demonstrate the DOX is loaded into the nanocapsules, nanocapsules filled with solid core were synthesized as a control by using the silica coated hematite instead of hollow silica shells as the template. The same DOX loading and polyelectrolyte coating were employed to the nanocapsules with a solid core (iron sulfide). From the released DOX from these solid particles, we calculate that the hollow particles release approximately 20× more DOX than the solid-core particles, indicating that most of the DOX is stored in the core of the hollow particles (Figure 4.13).

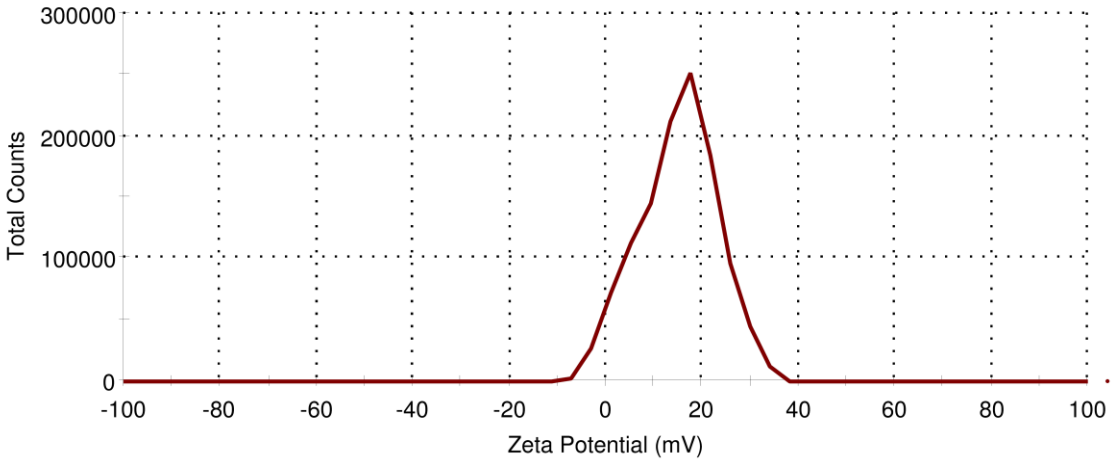

Figure 4.12 Zeta potential of Gd_2O_2S:Tb nanocapsules. Reprinted with permission from ref. 126. Copyright 2012 American Chemical Society.

To study the release rate at normal physiological pH and in acidic cancer environments, we measured the release rate in pH 7.4 PBS and 5.0, respectively. The cumulative release profile of doxorubicin from these nanocapsules is pH-dependent (Figure 4.14). The drug release is enhanced at pH 5.0 which is applicable for cancer therapy due to the low pH environment in tumor endosomes. Based upon exponential fitting to the HPLC release curve, the release rate time constant was estimated to be ~ 36 days at pH 7.4, and 21 hr at pH 5.0. From the released DOX at pH 5.0 after 48 h, the encapsulated DOX in DOX@Gd_2O_2S:Tb@PSS/PAH was over 5% by weight. The luminescence peak ratio at 544 nm and 620 nm is used to track the release of DOX (Figure 4.14B). The release rate time constant was estimated to be ~ 7 days at pH 7.4, and 4 hr at pH 5.0. The radioluminescence peak ratio is shown to be very sensitive to the release of DOX in the first 10 hr.

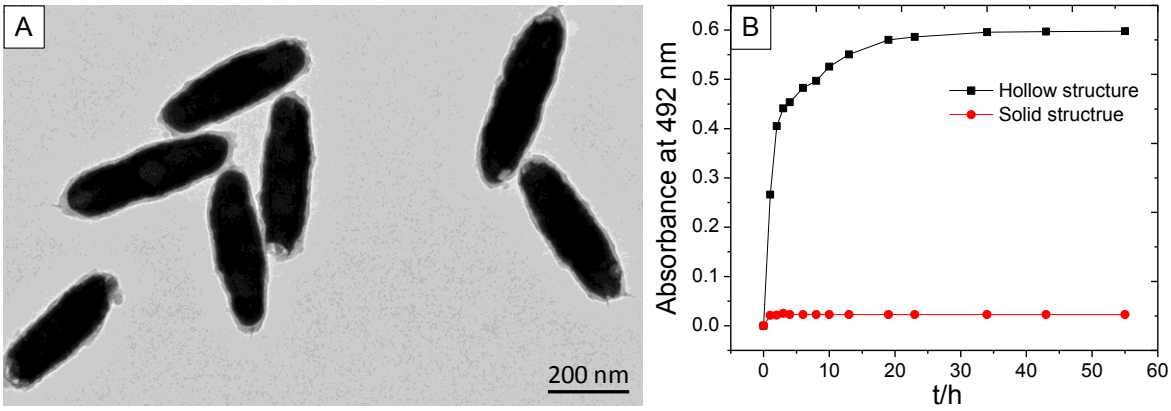

Figure 4.13 (A) PSS/PAH coated multilayers of nanocapsules with solid core, (B) absorbance of cumulative DOX released of hollow nanocapsules and nanocapluses with solid core at pH 2. Reprinted with permission from ref. 126. Copyright 2012 American Chemical Society.

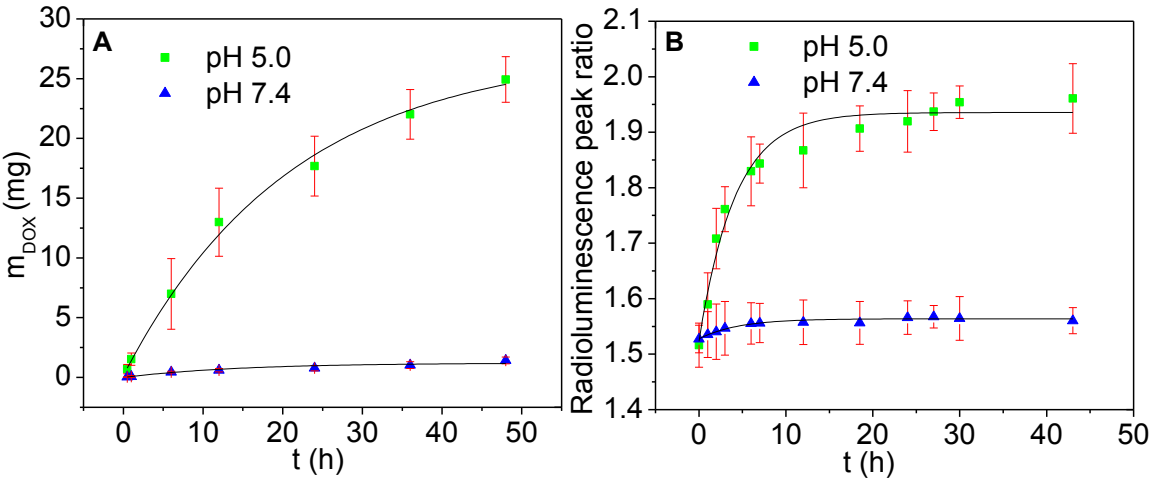

Figure 4.14 (A) Cumulative release of doxorubicin from DOX@Gd_2O_2S:Tb@PSS/PAH at pH 5.0 and 7.4, (B) peak ratio of real time radioluminescence detection at 544 and 620

nm as a function time in pH 5.0 and pH 7.4. The data fits to a single exponential. Reprinted with permission from ref. 126. Copyright 2012 American Chemical Society.

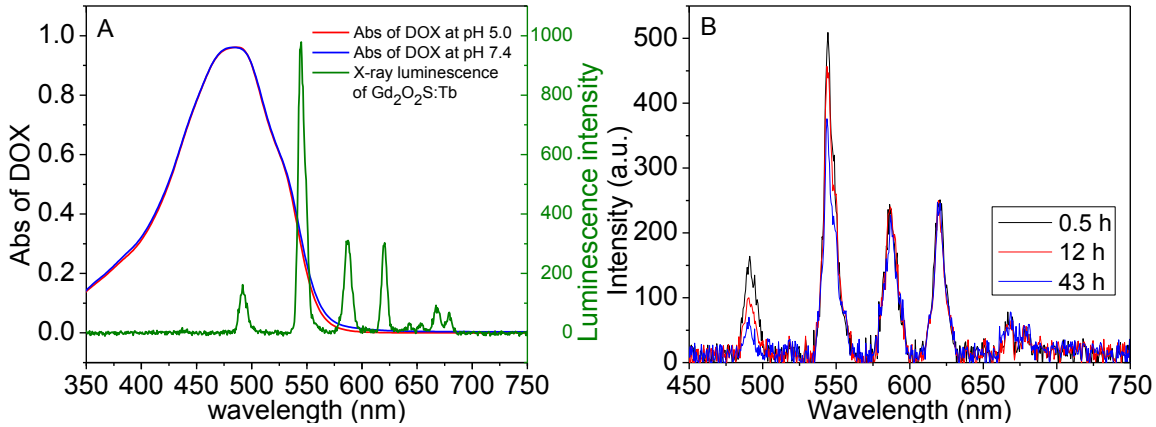

Figure 4.15 (A) Absorption of DOX (0.05 mg/ml at pH 5.0 and 7.4) and radioluminescence of Gd_2O_2S:Tb@PSS/PAH, (B) real-time radioluminescent spectra of DOX@Gd_2O_2S:Tb@PSS/PAH at pH 5.0. Reprinted with permission from ref. 126. Copyright 2012 American Chemical Society.

Our pH-responsive controlled release system is also able to monitor the release process of DOX at different pH by detecting the radioluminescence of Gd_2O_2S:Tb nanocapsules (Figure 4.15B). At pH 5.0 and 7.4, DOX has a similar broad absorption of light from 350 to 600 nm which overlaps with some of the XEOL peaks of Gd_2O_2S:Tb (Figure 4.15A). Figure 4.15B shows the intensity ratio of X-ray luminescence at 544 nm and 620 nm increases with the release of doxorubicin because local luminescence absorption by DOX decreases when DOX is released. We observed the similar luminescent increase of nanoparticle with iron oxide as a core when the iron oxide are

partially dissolved.[125] The peak intensity ratio reaches a maximum value when the DOX concentration in the particles is in equibilibrium with the solution concentration.

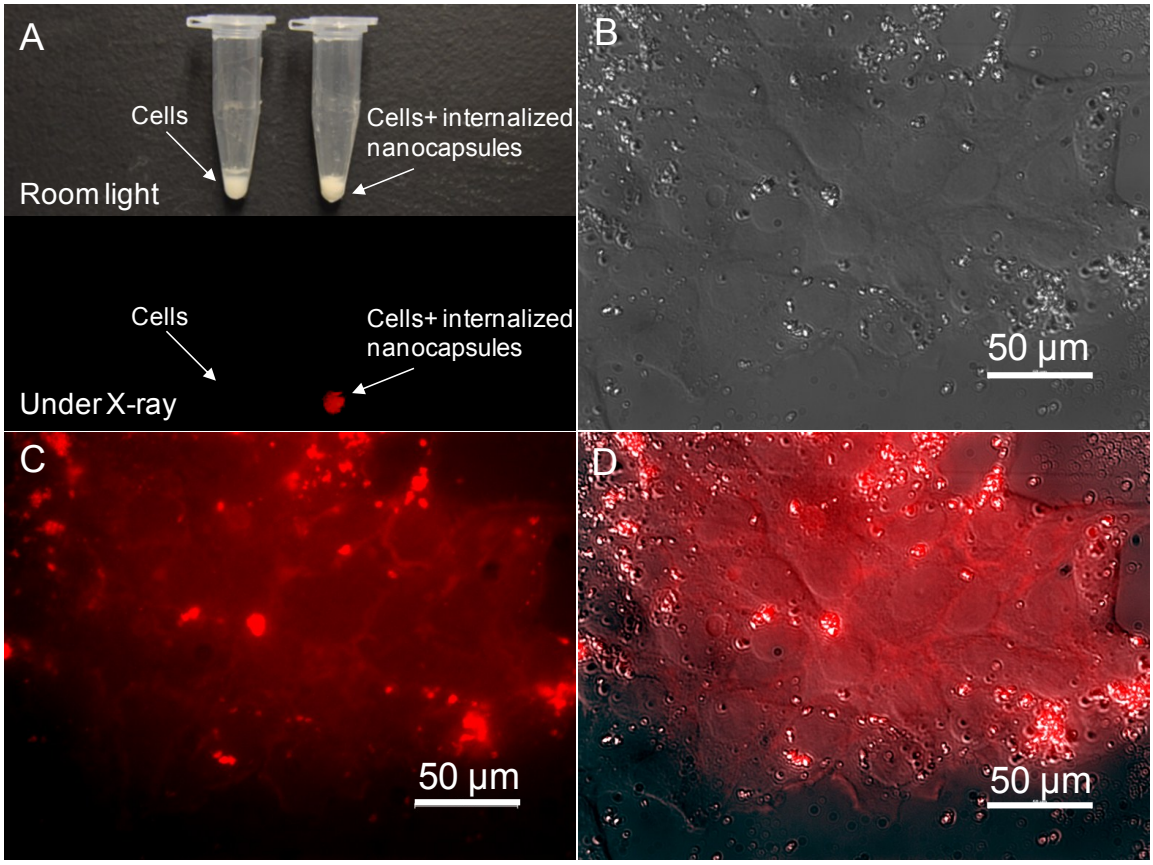

Figure 4.16 (A) Photograph of MCF-7 breast cancer cells with and without internalized nanocapsules (Gd_2O_2S:Eu) under room light and X-ray irradiation. Transmitted differential intereference contrast microscopy (B) and fluorescence image (C) of MCF-7 cells with internalized nanocapsules (Gd_2O_2S:Eu), (D) Merged image of (B) and (C). Reprinted with permission from ref. 126. Copyright 2012 American Chemical Society.

In order to examine the uptake of these nanocapsules by cancer cells, nanocapsules doped with europium (Gd_2O_2S:Eu) were incubated with MCF-7 cancer cell and washed multiple times to eliminate nanocapsules from the cell culture media. The internalized nanocapsules were brightly luminescent under X-ray radiation (Figure. 4.16A). The bright fluorescence signal of nanocapsules is very useful in drug localization and cell labeling. Figure 4.16C shows the fluorescence signal of the Gd_2O_2S:Eu nanocapsules in MCF-7 cancer cell after multiple washing step to eliminate nanocapsules from the cell culture media.

To demonstrate that the nanoparticle XEOL can be imaged *in vivo* using a IVIS Lumina-XR Imaging System (Caliper Life Sciences, Hopkinton, MA, US) during irradiation with miniature X-ray source (Amptek Mini X-ray tube, Ag target, Amptek Inc. MA, USA), 200 μL of 1 mg/mL Gd_2O_2S:Eu nanocapsules coated with PSS/PAH multilayers were inject into a mouse tail vein. The effective nanocapsule concentration in the mouse is about 133 μg/ml (the blood volume of a mouse is around 1.5 ml) which did not affect cell viability for MCF7 breast cancer cells *in vitro*. Furthermore, a preliminary Maximum Tolerated Dose (MTD) study was carried out and it shows no morbidity or weight loss was observed for doses up to 400 mg/kg. The *in vivo* accumulation of the

nanocapsules in the liver was evident under X-ray irradiation with 0.1 s exposure time. Compared to the Gd_2O_2S:Eu without PSS/PAH mutilayers (Figure 4.17), the accumulation rate for polyelectrolytes coated nanocapsules is slower in the first 1 h. Post mortem, XEOL images of the excised organs confirmed that the nanocapsules accumulated in liver and spleen (Figure 4.18).

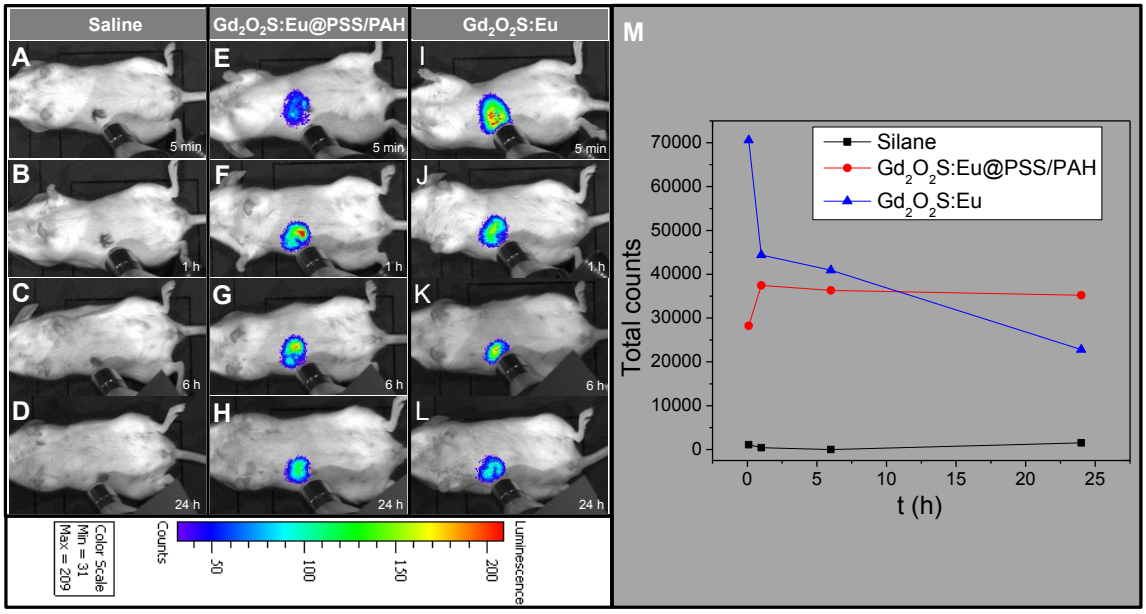

Figure 4.17 Representative luminescent images of accumulation of Gd2O2S:Eu nanocapsules with and without polymer coating in mouse. (A) 5 min, (B) 1 h, (C) 6 h, (D) 24 h after the mouse was injected with saline (200 µl). (E) 5 min, (F) 1 h, (G) 6 h, (H) 24 h after the mouse was injected with Gd2O2S:Eu@PAH/PSS nanocapsules (200 µl, 1 mg/ml). (I) 5 min, (J) 1 h, (K) 6 h, (L) 24 h after the mouse was injected with

Gd2O2S:Eu nanocapsules (200 µl, 1 mg/ml). (M) Total radioluminescent intensity counts as a function of time after injection. Reprinted with permission from ref. 126. Copyright 2012 American Chemical Society.

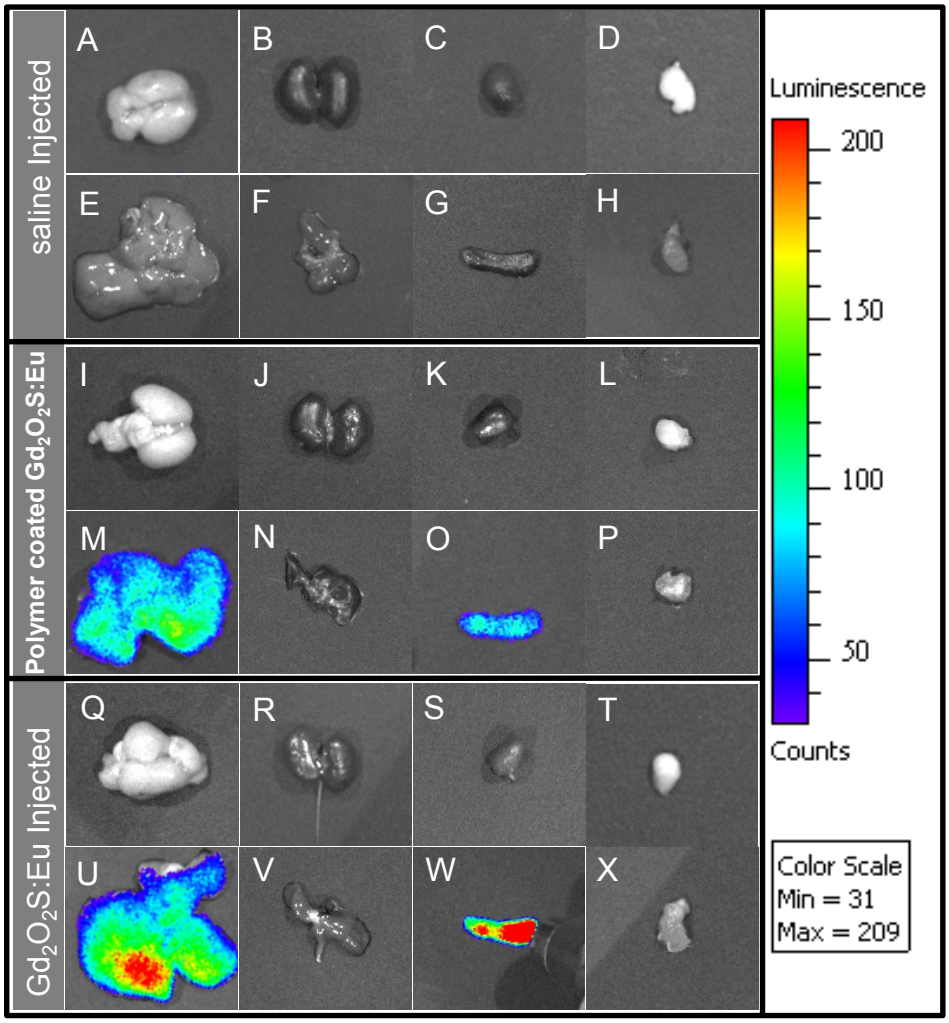

Figure 4.18 Representative radioluminescent images of accumulation of Gd_2O_2S:Eu nanocapsules with and without polymer coating in organs after 24 h. (A) Brain, (B) Kidney, (C) Heart, (D) Fat, (E) Liver, (F) Lung, (G) Spleen, and (H) Muscle in the saline injected mouse. (I) Brain, (J) Kidney, (K) Heart, (L) Fat, (M) Liver, (N) Lung, (O)

Spleen, and (P) Muscle in the Gd_2O_2S:Eu@PAH/PSS nanocapsules (200 µl, 1 mg/ml) injected mouse. (Q) Brain, (R) Kidney, (S) Heart, (T) Fat, (U) Liver, (V) Lung, (W) Spleen, and (X) Muscle in the Gd_2O_2S:Eu nanocapsules (200 µl, 1 mg/ml) injected mouse. Reprinted with permission from ref. 126. Copyright 2012 American Chemical Society.

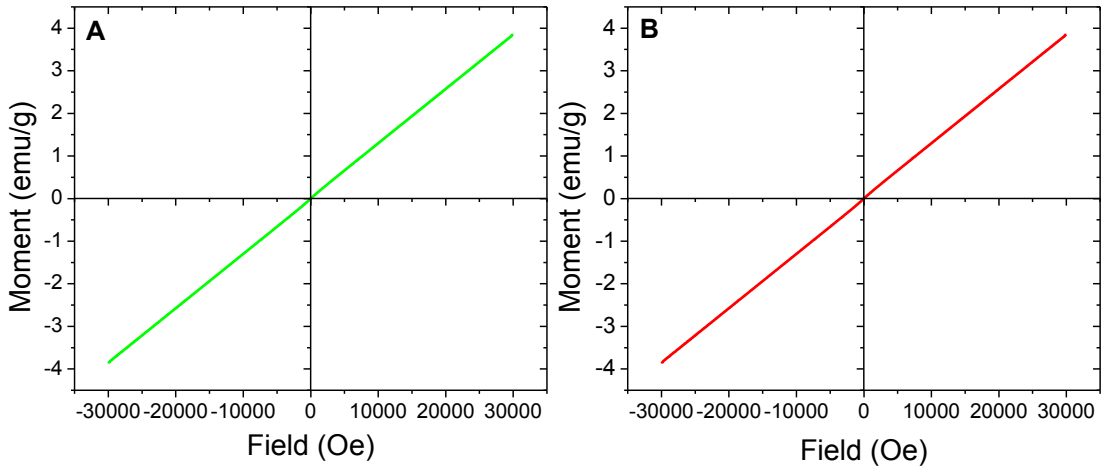

Figure 4.19 The magnetic hysteresis loops of (A) Gd_2O_2S:Tb and (B) Gd_2O_2S:Eu. Reprinted with permission from ref. 126. Copyright 2012 American Chemical Society.

Recent studies describe the synthesis and applications of gadolinium oxide (Gd_2O_3) nanoparticles as MRI contrast agents.[125, 139-143] However, to our knowledge, no investigation of gadolinium oxysulfide based MRI contrast agents are reported so far. Our luminescent nanocapsules mainly consisting of gadolinium oxysulfide (Gd_2O_2S) also have similar magnetic properties with gadolinium oxide which make them a potential MRI contrast agent and magnetic separation tool. The room temperature magnetic hysteresis loops of nanocapsules (Gd_2O_2S:Tb, Gd_2O_2S:Eu) are shown in Figure 4.19. As

the strength of the applied magnetic field increased, the linear correlation between the magnetization and the applied magnetic field indicates the both Gd_2O_2S:Tb and Gd_2O_2S:Eu nanocapsules are paramagnetic, with minimal hysteresis and a magnetic susceptibility of 1.2×10^{-4} emu g^{-1} Oe^{-1} and showed no sign of saturation up to applied fields of 30 kOe.

We performed *in vitro* MR assays (T_2 and T_2* weighted imaging) in 0.5% agarose gel for both types of Gd_2O_2S:Tb and Gd_2O_2S:Eu nanocapsules with a series of concentration (0.8 mg/ml, 0.4 mg/ml, 0.1 mg/ml, and 0.05 mg/ml). Figure 4.20 shows T_2 and T_2* weighted images after 3 ms. the proton relaxivities r_2 of the nanocapsules was determined from the longitudinal and transverse relaxation rates at various concentrations. These relaxation rates are shown as a function of concentration in Figure 4.21. The relaxivities, r_2 and r_2* are 50.3 $mM^{-1}s^{-1}$ and 116.0 $mM^{-1}s^{-1}$ respectively for Gd_2O_2S:Tb nanocapsules; 51.7 mM^{-1} s^{-1} and 116.4 $mM^{-1}s^{-1}$ for Gd_2O_2S:Eu nanocapsules.

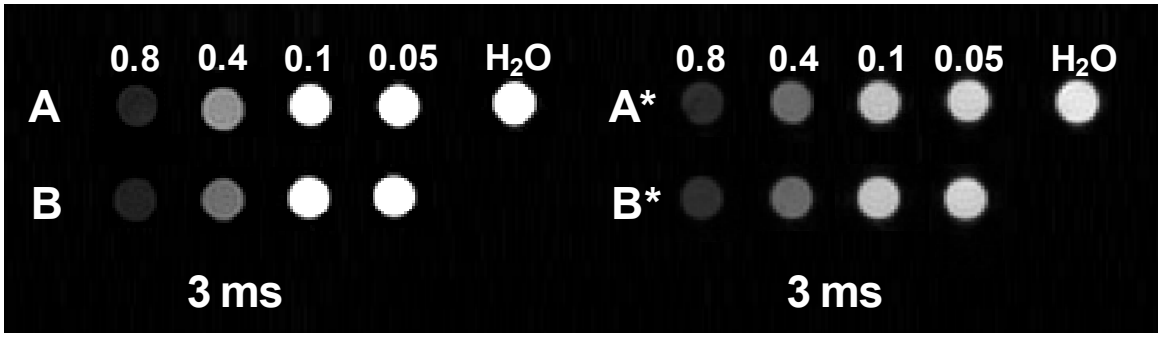

Figure 4.20 T2 and T2*-weighted images of radioluminescent nanocapsules. Group A: T2-weighted images of Gd_2O_2S:Eu nanocapsules with concentration of 0.8 mg/ml, 0.4 mg/ml, 0.1 mg/ml, and 0.05 mg/ml. Group B: T2-weighted images of Gd_2O_2S:Tb with concentration of 0.8 mg/ml, 0.4 mg/ml, 0.1 mg/ml, and 0.05 mg/ml. Group A*: T2*-weighted images of Gd_2O_2S:Eu nanocapsules with concentration of 0.8 mg/ml, 0.4

mg/ml, 0.1 mg/ml, and 0.05 mg/ml. Group B*: T2*-weighted images of Gd_2O_2S:Tb nanocapsules with concentration of 0.8 mg/ml, 0.4 mg/ml, 0.1 mg/ml, and 0.05 mg/ml. Reprinted with permission from ref. 126. Copyright 2012 American Chemical Society.

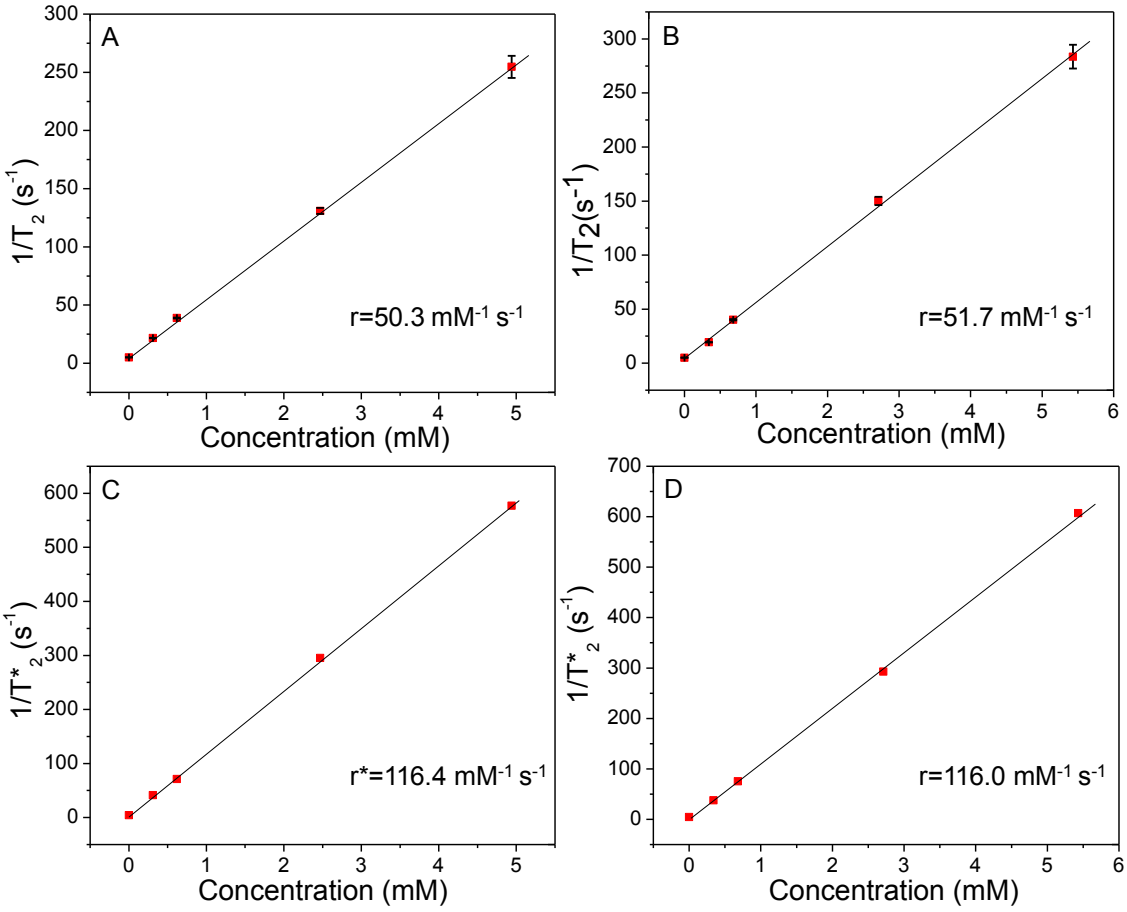

Figure 4.21 MRI T_2 and T_2* relaxation rate curves as a function of Gd_2O_2S:Tb (A, C) and Gd_2O_2S:Eu (B, D) concentration. Reprinted with permission from ref. 126. Copyright 2012 American Chemical Society.

For these nanocapsules, r_2* is larger than r_2 due to the inhomogeneities of local static field from the magnetic moment of the particles. Previous work towards the gadolinium nanoparticles (e. g. ultrasmall Gd_2O_3 nanoparticles (1~10 nm)[139-142] and hollow nanosparticles with thin Gd_2O_3 shell (~10 nm)[143]) reported that they can served as good T_1 contrast agents and moderate T_2 contrast agents. However, our nanocapsules with a ~25 nm Gd_2O_2S based nanoshell worked as a better T_2 contrast agents compared with Gd_2O_3 nanoparticles (r_2=14.1~16.9 $mM^{-1}s^{-1}$)[144-146] and gadolinium chelates (Gd-DTPA, 4.9 $mM^{-1}s^{-1}$)[144] compared with some In addition, the T_2 relaxivities value of our nanocapsules has similar value with some FDA-approved iron oxide nanoparticle contrast agents such as Ferumoxtran (Resovist®, 65 $mM^{-1}s^{-1}$), cross-linked iron oxide particle (CLIO-Tat, 62 $mM^{-1}s^{-1}$), and water soluble iron oxide (WSIO, 78 $mM^{-1}s^{-1}$).[147-150]

Conclusion

In summary, we present a flexible template-directed method to produce radioluminescent nanocapsules for a hydrophilic drug carrier and monitor release kinetics. The release rate time constant was ~ 36 days at pH 7.4, and 21.4 hr at pH 5.0, respectively. Importantly, the release mechanisms could be monitored *in situ* by tracking the ratio of readioluminescence spectral peaks. Radioluminescence offers several advantages over traditional optical imaging agents, including greater tissue penetration,

elimination of autofluorescence, and the ability to perform high-resolution imaging through thick tissue via functional X-ray Luminescence Tomography (FXLT)[54-55, 112, 123]. Finally, the multifunctional nanocapsules combined the advantages of positive contrast of radioluminescence and negative contrast of T_2 weighted MR imaging. These capabilities provide these nanocapsules to enable novel drug delivery and imaging modalities. In future, we plan to target DOX loaded capsules to tumors and measure *in situ* release rates and tumor growth for various nanocapsule sizes, shapes, and surface chemistries.

Experimental Section

Materials

Tetraethoxysilane (TEOS), poly(styrenesulfonate sodium) (PSS, MW:~70,000), Iron (III) chloride anhydrous was purchased from Sigma-Aldrich (St. Louis, MO). Gadolinium nitrate, europium nitrate, and poly(allylamine hydrochloride) (PAH, MW:~15,000) were purchased from obtained from Alfa Aesar (Ward Hill, MA). Ethanol (96%), urea, oxalic acid, ammonium hydroxide, and nitric acid were obtained from BDH Chemicals Ltd (Poole, Dorset, UK). Deionized (DI) water was purchased from EMD Chemicals Inc. (Gibbstown, NJ, USA). Polyvinylpyrrolidone (PVP K-30, MW 40,000) was purchased from Spectrum Chemicals (Gardena, CA). Agarose (melting point 88±1 ºC) was purchased from Shelton Scientific (Peosta, IA). All chemicals were used as received without further purification.

***In vitro* HPLC drug-release study and real-time drug release tacking:** 100 µl of DOX encapsulated nanocapsules with polyelectrolyte mutilayers (10 mg/ml) were suspended

with release media (7 ml) at pH 5.0 and 7.4 in Slide-A-Lyzer MINI dialysis units at room temperature. The release medium was removed for analysis at given time intervals, and replaced with the same volume of fresh release medium. The DOX concentration was measured with high performance liquid chromatography (HPLC) on a Waters system using an Alltima C18 column (250×4.6 mm, 5 μm).

Radioluminescence drug release tracking experiment: 2 ml DOX encapsulated nanocapsules with polyelectrolyte multilayers (25 mg/ml) were magnetically stirred at a rate of 400 rpm in release media of either pH 5 or pH 7.4. 50 μl of the solution was taken out for X-ray luminescence analysis without any separation at given time intervals.

Preparation of nanocapsules for MR Imaging: T_2 and T_2* MR measurements were acquired for the spindle-shaped SiO_2@Gd_2O_2S:Eu and Gd_2O_2S:Tb particles at a series of concentrations (0.8 mg/ml, 0.4 mg/ml, 0.1 mg/ml, and 0.05 mg/ml). The particles were dispersed in 0.5% agarose gel at 80 °C and cooled to room temperature in NRM tubes to set the gel. The gel prevented settling and aggregation allowing MRI imaging several days after preparation.

Cell viability test: MCF-7 breast cancer cells were seeded at a density of 10,000 cells/well in a 96-well plate. Cells were stored at 37 °C at 5% CO_2 and attached to the plate overnight. Nanocapsules were suspended in media, sonicated for 10 minutes to disperse, and diluted to 250, 100, 50, and 10 μg/ml. Media was removed from wells and fresh media or nanoparticle in media was added to each well. Five repeats were done for each concentration. Nanoparticles were incubated with cells overnight and the next day a Presto Blue assay (Life Technologies) was performed. Media was removed and 100 μl of

a 1:9 ratio Presto Blue in culture media was added to each well. Cells were incubated at 37 °C and 5% CO_2 for 45 minutes. Fluorescent intensity was taken with a plate reader with an excitation wavelength of 560 nm and an emission wavelength of 590 nm. Fluorescent intensity for each concentration of nanoparticle was normalized as a percentage of the fluorescent intensity of the control cells. Percent viability averages were plotted with error bars of one standard deviation.

Characterization methods: Transmission and scanning electron microscopy (TEM) were performed on a H9500 operated at 200 kV and HD2000 microscope operated at 20 kV, respectively. Powder XRD patterns were obtained on a Rigaku diffractometer at 40 kV and 40 mA ($Cu_{K\alpha}$ radiation). For fluorescence spectra, 480 nm light was used to excite the phosphors. To measure radioluminescence, X-ray was generated by a mini X-ray tube (Amptek Inc. MA, USA), the X-ray tube was operated with tube voltage of 40 kV and tube current of 40 mA. The sample was mounted on a Leica Microscope (Leica DMI 5000M, Wetzlar, Germany) equipped with a DeltaNu DNS 300 spectrometer (Intevac-DeltaNu, Laramie, WY USA) with a 150 lines/mm grating blazed at 500 nm and with a cooled CCD camera (iDUS-420BV, Andor, South Windsor, CT). X-ray luminescence images were captured with an IVIS Lumina-XR Imaging System (Caliper Life Sciences, Hopkinton, MA, US). Bright field and fluorescent images were taken on a Nikon microscope (Eclipse Ti, Nikon, Melville, NY USA). Determination of the Zeta-potential of the nanoparticles was performed via a Zetasizer Nano ZS (with a 633 nm He-Ne laser) from Malvern Instrument. Prior to the experiment, the particles were diluted in distilled water (0.1 mg/ml). Magnetization measurements were performed at the

designated temperature using vibrating sample magnetometer (VSM) option of physical property measurement system (PPMS, Quantum Design, USA), with the applied magnetic field sweeping between +/- 3.0 Tesla at a rate of 50 Oe/sec. Determination of the gadolinium content in a sample was performed by inductively coupled plasma (ICP)-(Optima 3100 RL; Perkin-Elmer). All MRI experiments were performed on a Varian 4.7T horizontal bore imaging system (Agilent Inc, Santa Clara, CA). Samples, contained in 5 mm NMR tubes, were placed in a 63 mm inner diameter quadrature RF coil for imaging.

CHAPTTER FIVE

V. MAGNETIC AND OPTICAL PROPERTIES OF MULTIFUNCTIONAL CORE-SHELL RADIOLUMINESCENCE NANOPARTICLES

Introduction

Multifunctional magnetic and fluorescent nanomaterials have attracted broad interest because of their utility in biomedical applications such as bioimaging,[151] drug delivery carriers,[152] magnetic resonance imaging (MRI),[153] bio-separation,[154] fluorescent labeling,[155-156] magnetic hyperthermia,[157] and immunoassays.[158] These magnetic particles can be magnetically guided, oriented, heated, and imaged using external magnetic fields. Meanwhile the particle fluorescence provides a sensitive label for imaging in cells and thin tissue sections.

Although biological tissues are essentially transparent to magnetic fields which facilitates *in vivo* magnetic control and imaging, fluorescence measurements are limited in thick tissue due to autofluorescence backgrounds and optical scattering. X-ray luminescence tomography (XLT) addresses these issues by using radioluminescent contrast agents for low background, high resolution imaging in tissue.[42, 159] Radioluminescence is well-suited for tissue imaging because both the X-ray excitation and near-infrared (NIR) emission penetrate deeply through tissue and because unlabeled tissues display minimal radioluminscence backgrounds. XLT images are generated by scanning a narrow X-ray beam relative to the sample and detecting the diffuse light escaping from the tissue using sensitive photodetectors. By restricting the X-ray excitation to a single narrow beam, the origin of the optical photons can be inferred

regardless of how many times these photons scatter in tissue and where they emerge from the tissue. This enables tomography with a resolution limited by the X-ray beam width in the tissue. The principle is similar to scanning confocal and structured illumination optical microscopies, except that while multiphoton confocal microscopy is limited to tissue thicknesses of 1 mm or less,[82] XLT can image through several centimeters of tissue because the X-rays are far less scattered than visible and NIR light. With a 1 mm X-ray beam and 1–100 cGy radiation dose, Pratx *et al*. achieved a spatial resolution of 1 mm through tissue-mimicking material based on the selective excitation of subpicomolar of 50 nm phosphor and optical detection of their luminescence.[42] They also showed that XLT could image the cross sectional distribution of microsize phosphor particles in 4.5 cm of an agar tissue phantom.[41]

Previously, we extended the XLT technique towards functional chemical imaging on implanted phosphor films using X-ray excited optical luminescence as a local light source for absorption spectroscopy of indicator dyes on the film surface. We developed a radioluminescent pH-sensing film based upon indicator dye absorption, and demonstrated 0.3 mm knife-edge resolution imaging through 1 cm of chicken.[112] We also imaged patterns of silver deposition and dissolution on a phosphor film through 1 cm of pork tissue.[123] Our technique is uniquely suited for studying chemical changes on the surface of implanted medical devices. The principle can also be extended to the third dimension for using particles with indicator dyes.

Herein, we developed a novel and facile strategy to fabricate magnetic phosphors for MRI and XLT imaging. Magnetic fluorescent and upconversion nanoparticles have

previously been reported with an iron oxide core and rare earth doped $NaYF_4$:Yb,Er shell.[160-161] However, a challenge is that iron oxide quenches most of the fluorescence if it contacts the phosphor or is in proximity, even with a thin silica spacer layer.[162-165] This demonstrates that absorption in the core modulates the luminescence signal, which would be a useful feature for generating chemical sensors with encapsulated indicators. However, the iron oxide core decreases the luminescence intensity and leaves no space for encapsulating drugs or dyes. In order to increase the luminescence intensity, we partially etched the iron oxide core in oxalic acid. The particles' optical and magnetic properties depend upon the core size, which in is controlled by varying the etching time. The etching process also produced a hollow space around the core which could be used for drug and dye encapsulation.

Results and discussion

Our objective was to synthesize radioluminescent particles with controllable size, shape, optical, and magnetic properties. We selected europium-doped gadolinium oxide as a matrix because of its photostablity,[166] its narrow and distinct spectral features under fluorescence and radioluminescence,[167-168] its MRI contrast,[139-140, 142-143, 169] and its relatively non-toxicicity.[140, 142-143] We selected a core-shell template synthesis route so that we could separately control the magnetic core and luminescent shell materials. Our initial studies employed spindle-shaped hematite cores and therefore generated spindle-shaped shells. However, the shape of the shell can be altered by using different core shapes by changing the hematite synthesis conditions.[132-133, 170] Although macrophage uptake of particles with diameters larger than 500 nm reduces circulation time and is an

obstacle to particulate drug delivery,[171] there are some reports that changes in particle shape strongly affect macrophage uptake and biodistribution. For example, Huang and Decuzzi *et al.* studied the clearance of a series of non-spherical silica/silicon nanoparticles with a length range of 300 nm~5 μm and observed that the particle shape plays a crucial role in the circulation lifetime and biodistribution which are important for drug delivery applications.[127-128, 130] Champion and co-workers recently found that macrophages internalize ellipsoid particles 2~6 μm long in a strongly orientation-dependent manner. They observed that it took only a few minutes to internalize particles with the high radius of curvature region contacting the macrophages, while particles contacting the macrophages on their low curvature sides were not internalized within 12 h.[129] Our long term goal will be to study how shape and size affect the biodistribution using *in situ* XLT imaging.

Structure and morphology of magnetic luminescent nanoeyes (γ-Fe_2O_3@SiO_2@Gd_2O_3:Eu)

The template core-shell synthesis process is presented in Figure 5.1. We first synthesized a monodispersed spindle-shaped hematite core according to methods described by Ozaki and co-workers.[21] Our particles were spindle shaped with an average length of 400 nm and diameter of 80 nm, however, by varying the synthesis conditions, the nanoparticle size can be tuned from 120 to 550 nm, and the aspect ratio from spheres to prolate spheroids.[132, 170] Hematite is a chemically stable antiferromagnetic phase of iron oxide which can be later reduced to magnetite or iron and oxidized to ferrimagnetic

maghemite (γ-Fe_2O_3). Hematite is used as a template because it is difficult to directly synthesize uniform spindle magnetite or maghemite particles, and these large particles often aggregate in magnetic fields especially at high particle concentration. The colloidal hematite particles had a positive zeta potential of +26 mV which kept them well dispersed in solution due to electrostatic repulsion. This positively charged hematite could not be directly used as template for growing a phosphor shell because the positively charged hematite would repulse the positively charged phosphor precursor ($Gd_2O(CO_3)_2$:Eu, +11 mV), see Figure 5.2. Instead, the hematite nanoparticles were first treated through a modified Stöber procedure[172] to deposit a thin silica layer which reversed the surface charge (-36 mV), see Figure 5.3. A phosphor shell was then successfully grown on these silica-modified hematite particles.

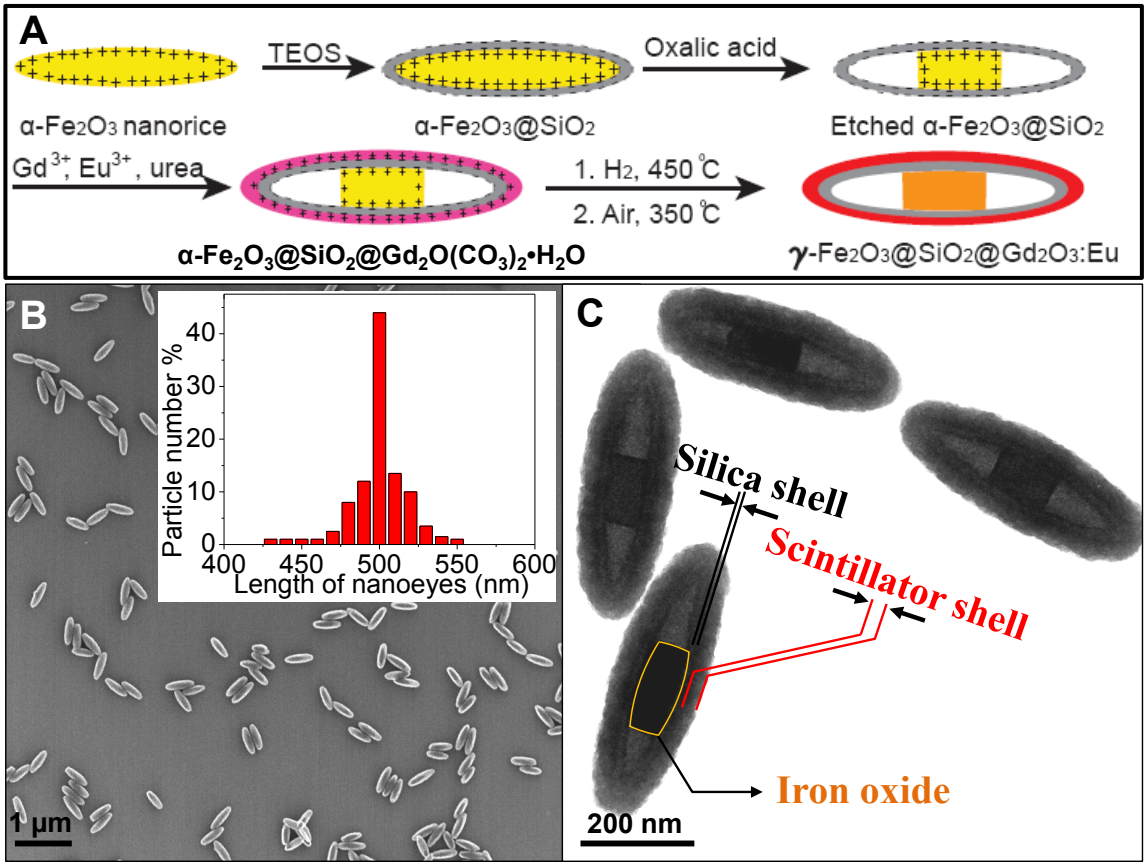

Figure 5.1 (A) Schematic illustration of the synthesis of nanoeyes (γ-Fe_2O_3@SiO_2@Gd_2O_3:Eu), SEM (B) and TEM (C) image of nanoeyes. The inserted figure in Figure 5.1A is the size distribution of nanoeyes. Reproduced from Ref. 125 with permission from the Royal Society of Chemistry.

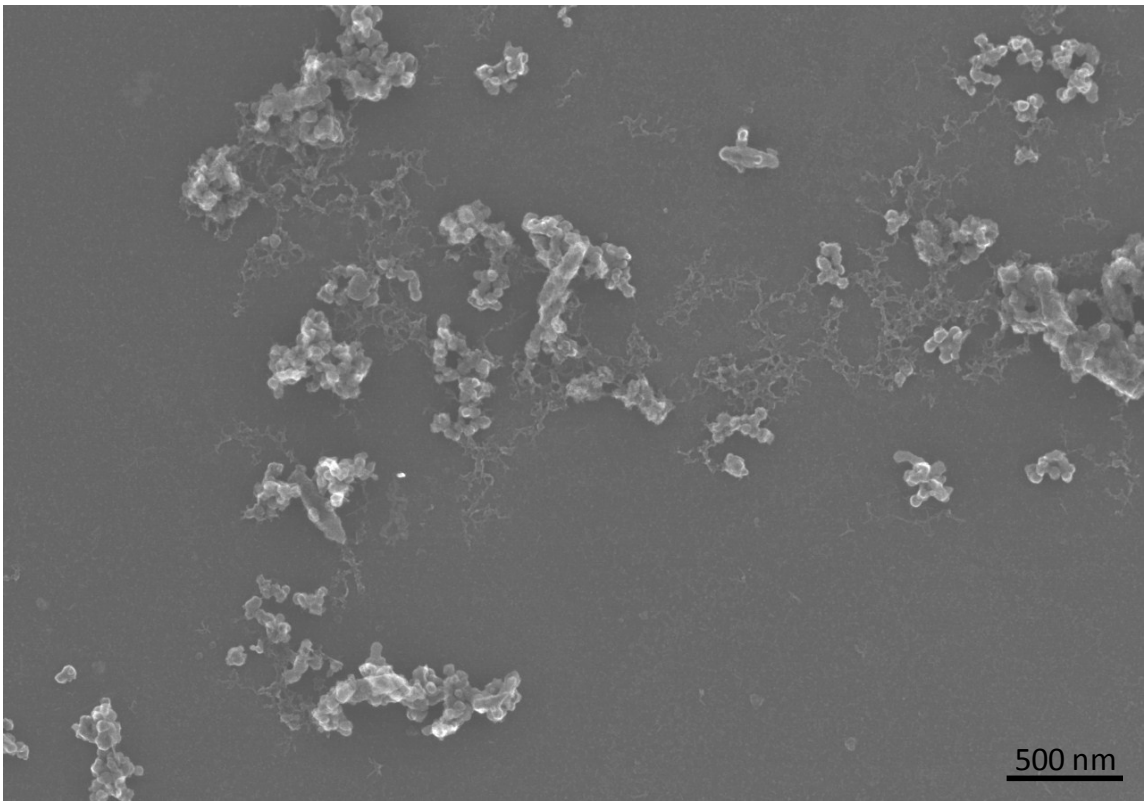

Figure 5.2 SEM images of growth of $Gd_2O(CO_3)_2$:Eu on spindle-shaped hematite nanoparticles without using an intermediate silica shell. Reproduced from Ref. 125 with permission from the Royal Society of Chemistry.

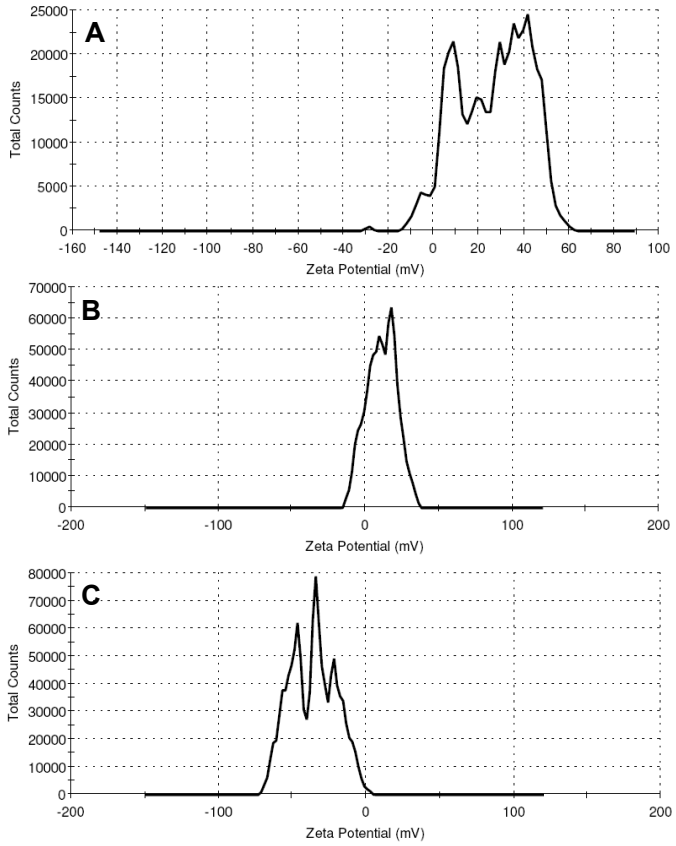

Figure 5.3 Zeta potential of (A) hematite nanorice (+26.1 mV), (B) $Gd_2O(CO_3)_2$:Eu (+11.1 mV), (C) silica coated hematite (-35.9 mV). Reproduced from Ref. 125 with permission from the Royal Society of Chemistry.

To increase the luminescence of the core-shell structure, and provide a hollow space for drug encapsulation, we etched the optically absorbing iron oxide core in oxalic acid solution at 60 °C for a controlled period of time. The obtained α-Fe_2O_3@SiO_2 particles had a monodispersed spindle-shaped shell with a hollow space around the core and appeared like "nanoeyes" in TEM images. After 9.5 h of etching, the magnetic cores of these nanoeyes were cylinder-shaped with an average length of 150 nm and diameter of

60 nm. In addition, the length of the iron oxide core was tunable from 0 to 400 nm with different etching time (Figure 5.4, 5.6).

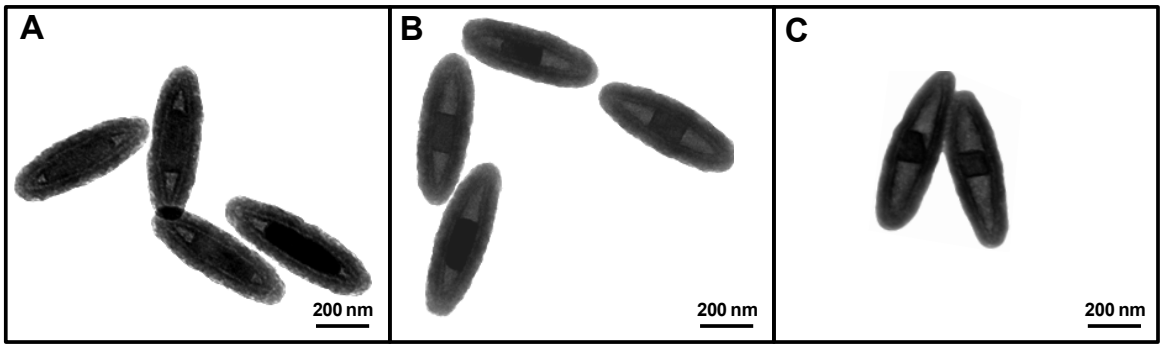

Figure 5.4 TEM images of nanoeyes incubated in 0.5 M oxalic acid at 60 ºC for (A) 8.5 h, (B) 9.5 h, (C) 10 h. Reproduced from Ref. 125 with permission from the Royal Society of Chemistry.

To synthesize radioluminescent particles, the silica-coated core-shell particles were then coated with a layer of $Gd_2O(CO_3)_2$:Eu through a homogeneous precipitation method from gadolinium, europium nitrate. In order to convert the α-Fe_2O_3 to γ-Fe_2O_3, the product above was treated by H_2/N_2 (5%/95%) at 450 °C for 3h and calcined later in the air at 350 °C for 24 h. The resulting monodispersed nanoeyes (γ-Fe_2O_3@SiO_2@Gd_2O_3:Eu) had an average length of about 500 nm and diameter of 80 nm (Figure 5.1B). They consisted of a ~10 nm silica intermediate shell and 40 nm phosphor outer shell which could be distinguished in TEM images such as Figure 5.1C because of the different electron penetrability between the Gd_2O_3, SiO_2, and γ-Fe_2O_3 core.

X-ray diffraction (XRD) was performed on the nanocomposite samples in order to investigate their structure and composition. Figure 5.5a shows the XRD pattern of the precursor of nanoeyes (α-Fe_2O_3@SiO_2@$Gd_2O(CO_3)_2$:Eu). The X-ray diffraction pattern

of α-Fe_2O_3 is clearly distinguished from the broad peak at about 30º from the porous $Gd_2O(CO_3)_2$:Eu. The XRD pattern of nanoeyes (Figure 5.5b) exhibits the characteristic diffraction peaks of cubic structure of Gd_2O_3. The γ-Fe_2O_3 core peaks in Figure 5.5b are indiscernibly weak because the cores have a small volume percentage and cross-section compared to the Gd_2O_3. However, the XRD pattern of γ-Fe_2O_3 can be readily distinguished under a thin shell (~10 nm) of Gd_2O_3:Eu (Figure 5.5c).

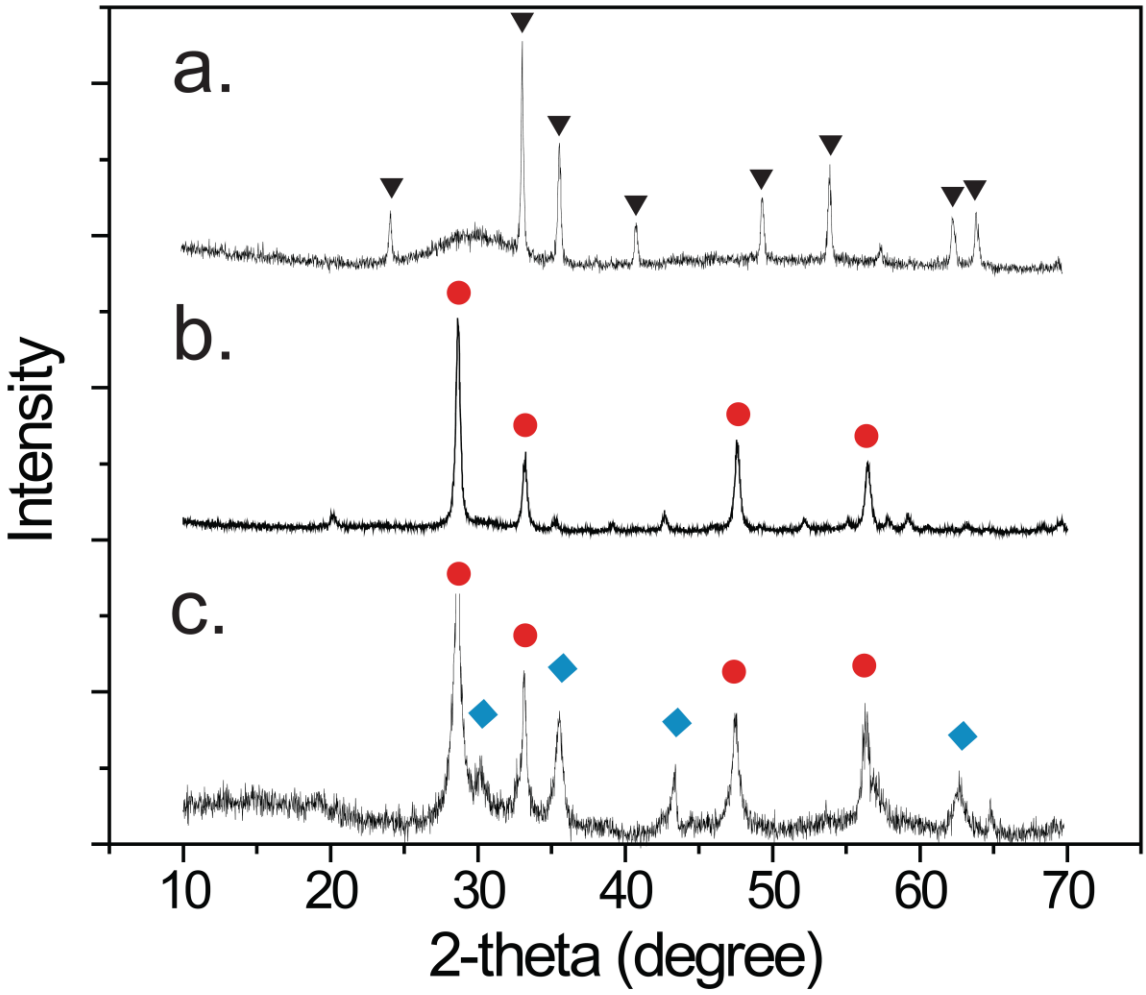

Figure 5.5 XRD patterns of (a) precursor of nanoeye (α-Fe_2O_3@SiO_2@$Gd_2O(CO_3)_2$:Eu), (b) nanoeye γ-Fe_2O_3@SiO_2@Gd_2O_3:Eu (iron oxide core was incubated in oxalic acid for 9.5 h), (c) nanoeye (iron oxide core was incubated in oxalic acid for 9.5 h) with thin Gd_2O_3:Eu shell (~10 nm). (▼: α- Fe_2O_3, ●: Gd_2O_3:Eu, ◆:γ-Fe_2O_3) Reproduced from Ref. 125 with permission from the Royal Society of Chemistry.

Magnetic and optical and properties of magnetic luminescent nanoparticles

In order to elucidate the magnetic properties of the nanoeyes, we synthesized similar shell structures with solid iron oxide cores and hollow particles with dissolved cores by incubation of the α-Fe_2O_3@SiO_2 in oxalic acid for 0 h and 17 h, respectively (Figure 5.6). The solid-core nanorice (γ- Fe_2O_3@SiO_2@Gd_2O_3:Eu) and hollow nanorice (SiO_2@Gd_2O_3:Eu) both are monodispersed with a radioluminescent shell shape almost identical to the nanoeyes (Figure 5.7).

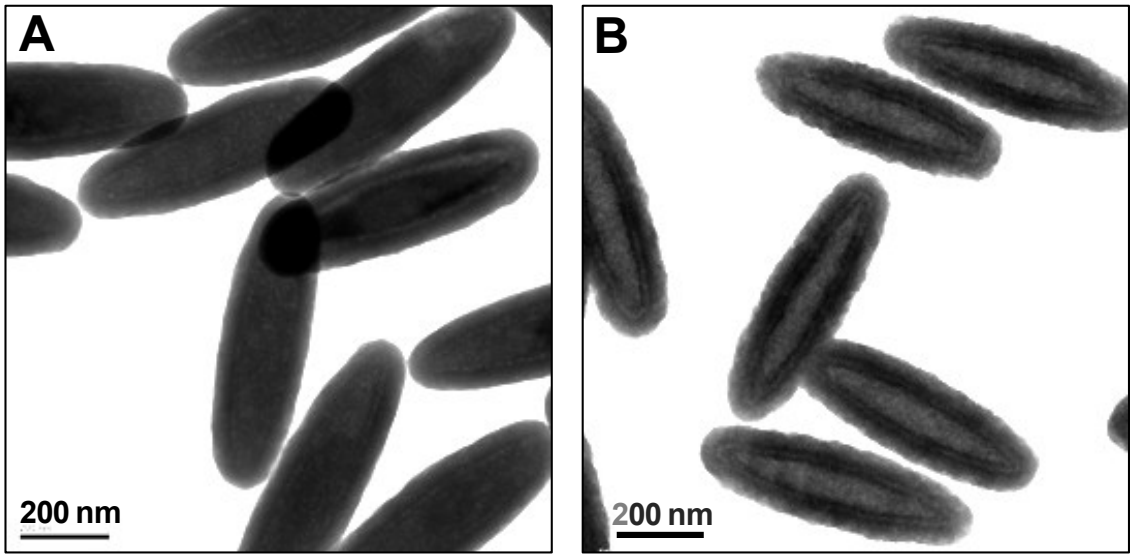

Figure 5.6. TEM image of nanorice (A) and hollow nanorice (B). Reproduced from Ref. 125 with permission from the Royal Society of Chemistry.

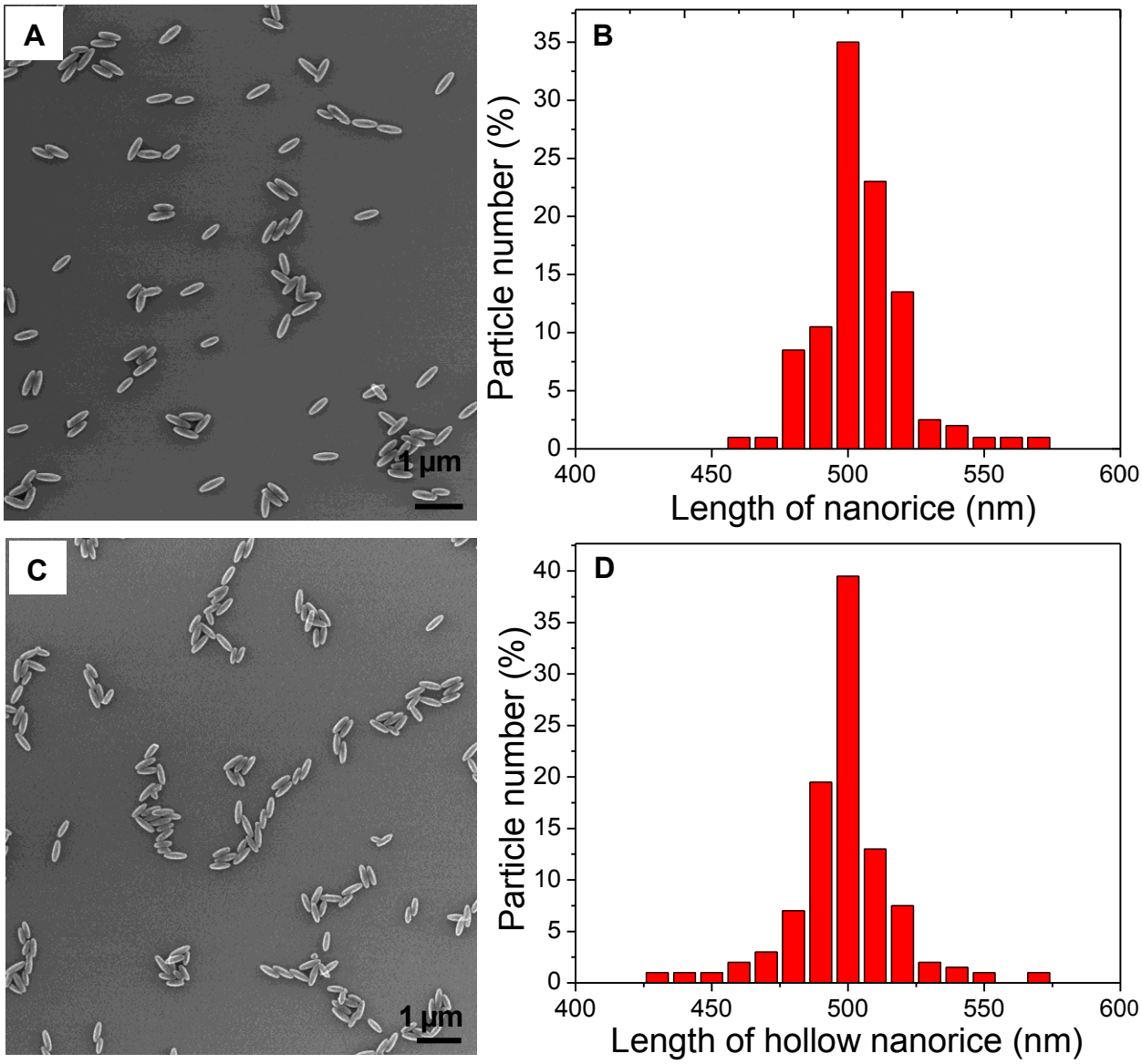

Figure 5.7 SEM images of nanorice (γ-Fe_2O_3@SiO_2@Gd_2O_3:Eu, solid structure) (A) and corresponding size distribution (B). SEM images of hollow nanorice (SiO_2@Gd_2O_3:Eu) (C), and corresponding size distribution (D). Reproduced from Ref. 125 with permission from the Royal Society of Chemistry.

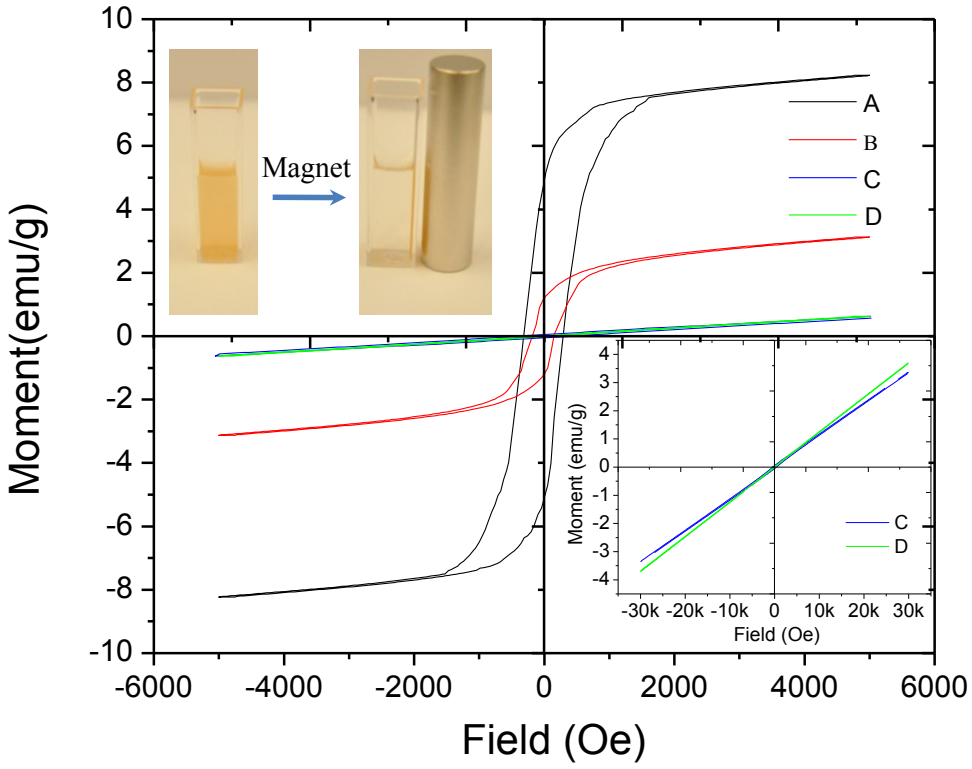

Figure 5.8 The magnetic hysteresis loops of magnetic probes. (A) nanorice with maghemite as the core, (B) nanoeyes (iron oxide core was incubated in oxalic acid for 9.5 h), (C) nanorice with hematite as the core, and (D) hollow nanorice. Bottom inset shows the hysteresis loops of nanorice with hematite as the core and hollow nanorice. Top inset show rapid (3 min) magnetophoretic separation of a solution of nanoeyes in a 1 cm pathlength cuvette. Reproduced from Ref. 125 with permission from the Royal Society of Chemistry.

The room temperature magnetic hysteresis loops of magnetic nanorice, nanoeyes, and hollow nanorice are shown in Figure 5.8. The hollow nanorice (SiO_2@Gd_2O_3:Eu) are paramagnetic, with minimal hysteresis and a magnetic susceptibility of 1.23×10^{-4} emu g^{-1} Oe^{-1} and showed no sign of saturation up to applied fields of 30 kOe. From the TEM images (Figure 5.6) the core is approximately 13% of the volume and a similar percentage of the mass. The iron oxide was converted to maghemite (γ-Fe_2O_3) via H_2 reduction followed by oxidization in air (350 °C 24 h), and the particle colour changed from red with the hematite core to brownish with the maghemite core. The nanorice magnetization curve (Figure 5.8A) had two components, a hystertic ferrimagnetic (or ferromagnetic) component with a coercivity of 308 Oe and a saturation magnetization of ~7.6 emu/g, and a paramagnetic component (linear slope at large applied fields). The saturation magnetization of the ferrimagnetic component is approximately 10% of the saturation magnetization of bulk γ-Fe_2O_3 (74 emu/g).[173] These results are consistent with a core ~10% maghemite by weight and a shell ~90% by weight which is also consistent with the TEM images and ICP elemental analysis data. The hysteresis curve for nanoeye (Figure 5.8B) had a smaller ferrimagnetic component with a saturation magnetization of 2.3 emu/g, which is consistent with a 3-fold reduction in weight per cent of maghemite. The coercivity decreased to 165 Oe likely due to the decreases in the aspect ratio of the iron oxide core. Although the saturation magnetization of the partially dissolved nanoeyes is smaller than the nanorice, the magnetization is still strong enough for rapid magnetophoretic separation (inset figure of Figure 5.8).

In addition to magnetophoretic separation in magnetic field gradients, the particles are expected to align with external magnetic fields due to their magnetic shape anisotropy. This alignment is useful in developing sensitive and rapid immunoassays, viscosity sensor, and improved intracellular sensors with orientation and shape-dependent properties.[174-176] For example, orientation of non-spherical particles has been shown to affect phagocytosis rates for adherent macrophages.[129, 177] In addition, the ability for particles to rotate is useful for determining if particles are bound, while the rotation rate in solution is useful for measuring viscosity and viscous drag.[175] We demonstrate that the magnetic nanoeyes rotate in response to a rotating external magnetic field by measuring the scattering signal intensity as the particles rotate in response to a changing magnetic field. Experimentally, we placed a solution of nanoeyes in water/glycerol (v_{water}:$v_{glycerol}$=1:9) on a glass slide and observed the scattering intensity with a dark field microscope. The nanoeyes were orientated by an external magnetic field which rotated by 90 º in every 3 s. As depicted in Figure 5.9, the scattering intensity was largest when the particles were oriented parallel to the sample plane and presented the largest scattering area. The scattering intensity decreased when the particles were oriented parallel to the optical axis. Figure 5.9C shows the magnetically modulated optical scattering by the nanoeyes. This rotational modulation cannot be observed for spherical particles which have isotropic scattering properties.

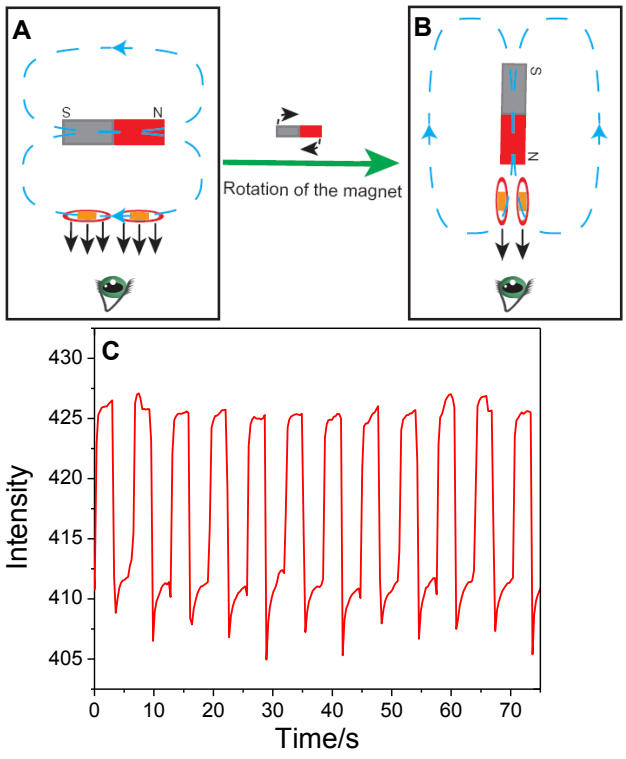

Figure 5.9 Schematic presentation of magnetic modulation of scattering of light (A, B) by nanoeyes (iron oxide core was incubated in oxalic acid for 9.5 h), (C) Intensity time series for nanoeyes under darkfield microscope. Reproduced from Ref. 125 with permission from the Royal Society of Chemistry.

In addition to magnetic rotation and separation, the nanoeyes display fluorescence under 480 nm excitation light and radioluminescence under X-ray excitation (Figure 5.10). The main emission peak of the Gd_2O_3:Eu phosphor shell with cubic structure was observed at 610 nm, which corresponds to a red emission from the $^5D_0 \rightarrow {}^7F_2$ Eu^{3+} transition. The fluorescence and radioluminescence of the solid core nanorice were hardly detected. The luminescence quenching is likely due to inner filter effects as the 10 nm

silica shell spacer and hollow regions in the core would inhibit resonant energy transfer. Previous approaches to address this quenching problem by separating the luminescent shell from the absorptive core using a coating thick silica shell (>50 nm) also increase the particle size.[161, 165] By contrast, the current method of partial dissolving the iron oxide core reduces the quenching while maintains the total nanoparticle size and volume. We expect that carefully controlling dissolution time will allow optimization of the optical and magnetic properties. In addition, a hollow space is formed around the iron oxide core in the nanoeyes which could serve to encapsulate drugs for drug delivery applications (See Figure 5.11). We expect that low molecular weight drugs can be loaded into the hollow space of the particles.

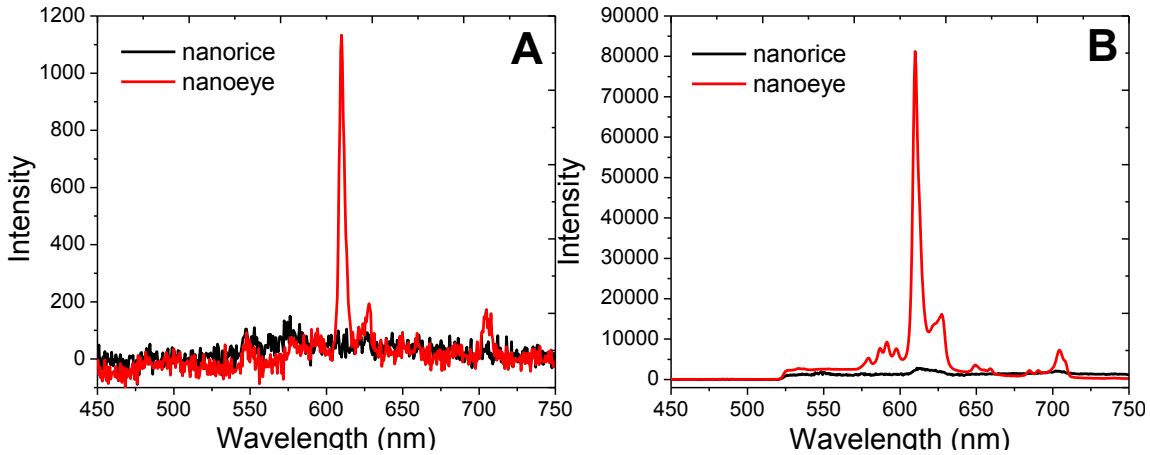

Figure 5.10 (A) Radioluminescence spectra of nanoeyes (iron oxide core was incubated in oxalic acid for 9.5 h) and nanorice excited by X-ray, (B) Fluorescence spectra of nanoeyes (iron oxide core was incubated in oxalic acid for 9.5 h) and nanorice excited by 480 nm light. Reproduced from Ref. 125 with permission from the Royal Society of Chemistry.

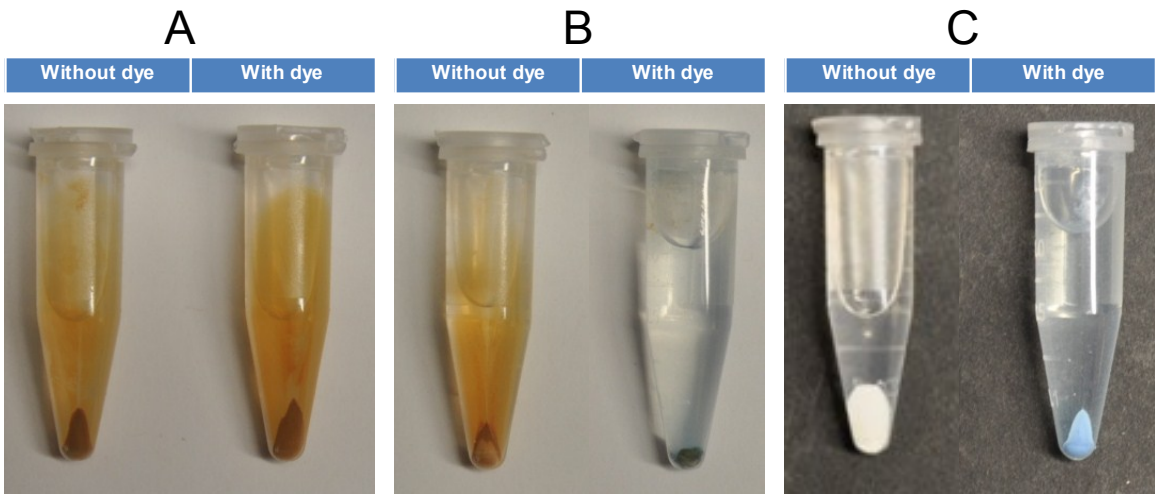

Figure 5.11 Photography of nanorice (A), nanoeyes (B), and hollow nanorice (C) without and with bromocresol green dye encapsulated by a ~10 nm silica coating. Samples were obtained after centrifuged for 15 min at 4000 rpm. Reproduced from Ref. 125 with permission from the Royal Society of Chemistry.

Although the hollow nanorice obtained by completely dissolving the iron oxide are paramagnetic, brightly luminescent, and have a large internal space for encapsulation, their magnetic moment is weak compared to the solid nanorice and nanoeyes, especially at low fields. As a result, they separate only very slowly with typical permanent magnet-generated magnetic fields and field gradients. The nanorice particles with a solid iron oxide core respond rapidly to magnetic fields but display only weak fluorescence and negligible radioluminescence. In addition, there is not much space within the core for dye and drug encapsulation. By partially dissolving the iron oxide core, nanoeyes are formed which display magnetophoresis and radioluminescence. Their bright luminescence under UV (365 nm) and X-ray irradiation is shown in Figure 2.12. Compared with the UV

fluorescence, the X-ray luminescence of the nanoeyes provides a background-free image which can be used for deep tissue imaging. The hollow regions in the nanoeyes could also be used for indicator dye and drug encapsulation for theranostic applications. To test whether the pores in the Gd_2O_3 shell were large enough for small molecules to diffuse through, we incubated the nanoparticles in a solution of bromocresol blue dye, encapsulated the dye and particle with ~ 10 nm silica layer, and washed and separated the particles via centrifugation. The dye could indeed be encapsulated (see Figure 5.11), while a control, the solid core particles could not encapsulate dye. We are currently developing coatings to control the dye release rate.

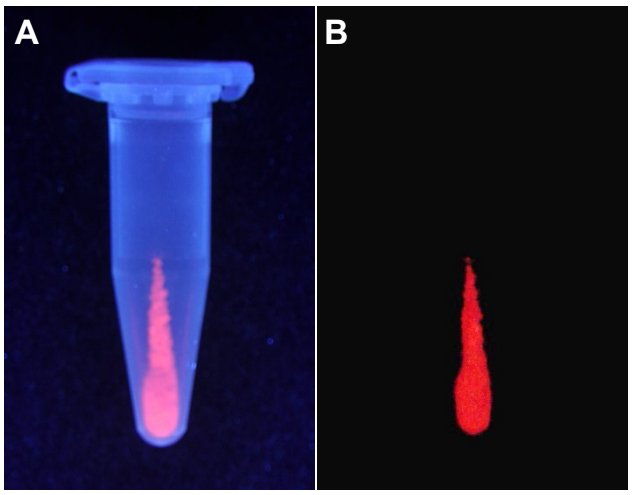

Figure 5.12 Photograph of hollow nanorice under (A) UV light (365 nm) and (B) X-ray luminescence. Reproduced from Ref. 125 with permission from the Royal Society of Chemistry.

Magnetic luminescent nanoparticles as T_2 contrast agent

It is useful to have contrast agents that provide both radioluminescence and MRI contrast in order to validate measurements, and provide complimentary information (e.g. molecular information with functional XLT spectroscopy using indicators and tissue contrast with MRI). Our magnetic radioluminescent particles are expected to serve as *T2* and T_2* contrast agents because of their strong magnetic moment in static MRI fields. This is consistent with recent work showing that gadolinium oxide nanoparticles have higher relaxivities compared with gadolinium chelates.[169, 178-179]

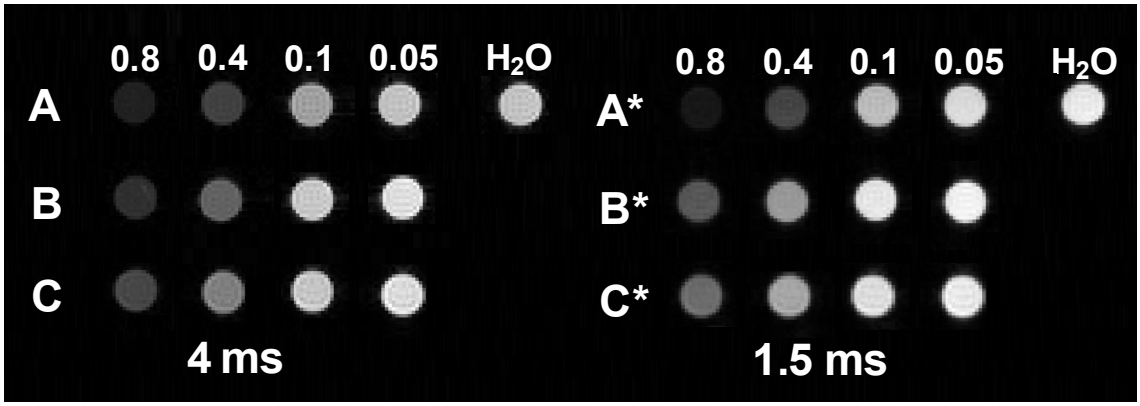

Figure 5.13 T_2 and T_2*-weighted images of nanorice, nanoeyes (iron oxide core was incubated in oxalic acid for 9.5 h), and hollow nanorice at echo time of 4 ms and 1.5 ms, respectively. Group A: T_2-weighted images of nanorice with concentration of 0.8 mg/ml, 0.4 mg/ml, 0.1 mg/ml, and 0.05 mg/ml. Group B: T_2-weighted images of nanoeyes with concentration of 0.8 mg/ml, 0.4 mg/ml, 0.1 mg/ml, and 0.05 mg/ml. Group C: T_2-weighted images of hollow nanorice with concentration of 0.8 mg/ml, 0.4 mg/ml, 0.1 mg/ml, and 0.05 mg/ml. Group A*: T_2-weighted images of nanorice with concentration

of 0.8 mg/ml, 0.4 mg/ml, 0.1 mg/ml, and 0.05 mg/ml. Group B*: T_2*-weighted images of nanoeyes with concentration of 0.8 mg/ml, 0.4 mg/ml, 0.1 mg/ml, and 0.05 mg/ml. Group C*: T_2-weighted images of hollow nanorice with concentration of 0.8 mg/ml, 0.4 mg/ml, 0.1 mg/ml, and 0.05 mg/ml. Reproduced from Ref. 125 with permission from the Royal Society of Chemistry.

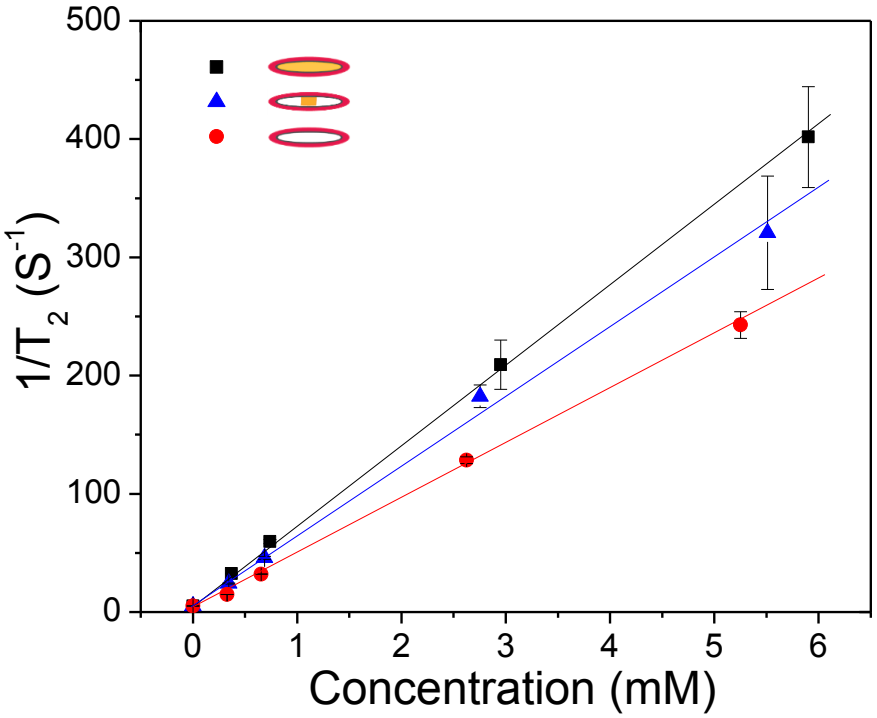

Figure 5.14 The relaxation rate curves as a function of concentration. ■: nanorice, ▲: nanoeyes (iron oxide core was incubated in oxalic acid for 9.5 h), ● hollow nanorice. Error bars represent the standard deviation. Reproduced from Ref. 125 with permission from the Royal Society of Chemistry.

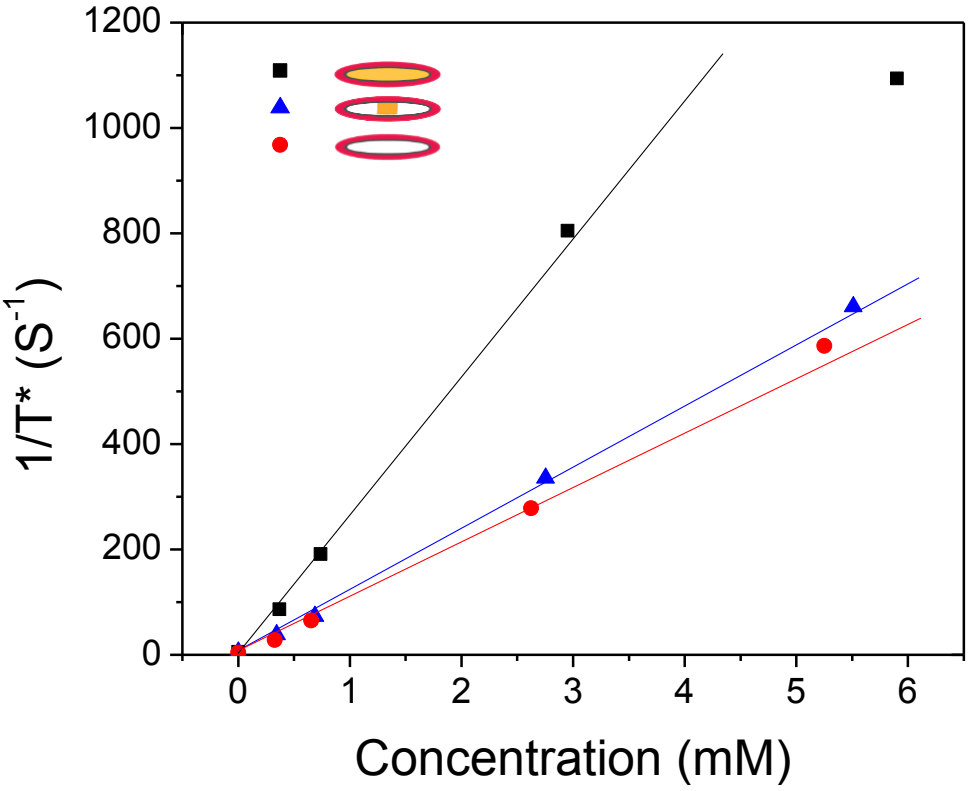

Figure 5.15 The relaxation rate curves, $1/T_2$*, as a function of particle concentration. To calculate relaxivity, r_2*, the curve is fit to a straight line for concentrations up to 0.4 mg/mL) ■: nanorice, ▲: nanoeyes (iron oxide core was incubated in oxalic acid for 9.5 h), ● hollow nanorice. Reproduced from Ref. 125 with permission from the Royal Society of Chemistry.

Figure 5.13 shows T_2 and T_2* weighted images after 4 ms and 1.5 ms, respectively. The decrease with echo time was fit to an exponential in order to calculate the relaxation rate, $R_2 = 1/T_2$ and $R_2^* = 1/T_2^*$ at each concentration. These relaxation rates are shown as a function of concentration in Figure 5.14 and Figure 5.15 (see Table 5.1 for the molar concentration of Gd and Fe in 0.8, 0.4, 0.1, and 0.05 mg/ml of solution). The

curves are approximately linear, although there is some evidence of saturation at the highest concentration, 0.8 mg/ml. Fitting the points up to 0.4 mg/mL (2.6-3 mM), the relaxivities, r_2 and r_2* are 68.73 $mM^{-1}s^{-1}$ and 274.11 $mM^{-1}s^{-1}$ respectively for the nanorice; 58.10 mM^{-1} s^{-1} and 120.43 $mM^{-1}s^{-1}$ for the nanoeyes, and 46.00 $mM^{-1}s^{-1}$ and 111.76 $mM^{-1}s^{-1}$ for the hollow nanorice. The relaxivity is calculated based on the total molar concentration of both Gd^{3+} and Fe^{3+}. For comparison with other literature we have also calculated r_2 and r_2* using the molar concentrations of just Gd^{3+} and Fe^{3+}, and the total mass concentration in mg/mL (see Table 5.2). For all particles, r_2* is larger than r_2 because r_2 includes contributions from local static field inhomogeneities caused by the magnetic moment of the particles. The difference between r_2 and r_2* may provide more specificity towards the contrast agents, especially for the nanorice which display a factor of 4 increased relaxivity. The iron oxide core significantly increased the relaxivities, with the solid core providing the highest relaxivity and the hollow core the least.

Table 5.1 ICP analysis of Gd^{3+} and Fe^{3+} in nanorice, nanoeyes, and hollow nanorice in 0.8, 0.4, 0.1, 0.05 mg/ml of solution.The 0 value for Fe^{3+} means < 0.01 mg/L, i.e. below the limit of detection. Reproduced from Ref. 125 with permission from the Royal Society of Chemistry.

Weight concentration / Type of nanoparticle		0.8 mg/ml	0.4 mg/ml	0.1 mg/ml	0.05 mg/ml
Nanorice	Gd^{3+}	4.700 mM	2.350 mM	0.588 mM	0.294 mM
	Fe^{3+}	1.200 mM	0.600 mM	0.150 mM	0.075 mM
Nanoeyes	Gd^{3+}	4.780 mM	2.390 mM	0.598 mM	0.299 mM
	Fe^{3+}	0.730 mM	0.365 mM	0.091 mM	0.046 mM
Hollow nanorice	Gd^{3+}	5.250 mM	2.626 mM	0.656 mM	0.328 mM
	Fe^{3+}	0 mM	0 mM	0 mM	0 mM

Table 5.2 r_2 and r_2* calculated based on molar concentration Gd^{3+}, Fe^{3+}, Gd^{3+}+Fe^{3+}, and weight concentration of particles. Reproduced from Ref. 125 with permission from the Royal Society of Chemistry.

Relaxivity / Type of nanoparticle		r_2	r_2*
Nanorice	Weight concentration	514 ml $mg^{-1}s^{-1}$	2029 ml $mg^{-1}s^{-1}$
	Molar concentration (Gd^{3+})	86.28 $mM^{-1}s^{-1}$	344.10 $mM^{-1}s^{-1}$
	Molar concentration (Fe^{3+})	337.92 $mM^{-1}s^{-1}$	1347.71 $mM^{-1}s^{-1}$
	Molar concentration (Gd^{3+}+Fe^{3+})	68.73 $mM^{-1}s^{-1}$	274.11 $mM^{-1}s^{-1}$
Nanoeyes	Weight concentration	454 ml $mg^{-1}s^{-1}$	847 ml $mg^{-1}s^{-1}$
	Molar concentration (Gd^{3+})	66.97 $mM^{-1}s^{-1}$	138.82 $mM^{-1}s^{-1}$
	Molar concentration (Fe^{3+})	438.54 $mM^{-1}s^{-1}$	909.00 $mM^{-1}s^{-1}$
	Molar concentration (Gd^{3+}+Fe^{3+})	58.10 $mM^{-1}s^{-1}$	120.43 $mM^{-1}s^{-1}$
Hollow nanorice	Weight concentration	322 ml $mg^{-1}s^{-1}$	701 ml $mg^{-1}s^{-1}$
	Molar concentration (Gd^{3+})	46.00 $mM^{-1}s^{-1}$	111.76 $mM^{-1}s^{-1}$

Previous work showed that ultrasmall Gd_2O_3 nanoparticles (1~10 nm)[139-142] and hollow nanosparticles with thin Gd_2O_3 shell (~10 nm)[143] served as good T_1 contrast

agents and moderate T_2 contrast agents. In contrast, our spindle-shaped nanoparticles with a ~40 nm Gd_2O_3:Eu shell worked better as a T_2 contrast agents. This may be due to low water exchange efficiency inside of the porous Gd_2O_3 nanoparticles, which is consistent with earlier work by using the porous Gd_2O_3 nanoparticles (~200 nm in diameter).[143] Compared to FDA-approved iron oxide nanoparticle contrast agents such as Ferumoxtran (Resovist®, 65 $mM^{-1}s^{-1}$), cross-linked iron oxide particle (CLIO-Tat, 62 $mM^{-1}s^{-1}$), and water soluble iron oxide (WSIO, 78 $mM^{-1}s^{-1}$), our nanorice, nanoeyes, and hollow nanorice had similar T_2 relaxivities.[147-150] However, these T_2 relaxivities were several times higher than typical gadolinium chelates (Gd-DTPA, 4.9 $mM^{-1}s^{-1}$)[144] and Gd_2O_3 nanoparticles (14.1~16.9 $mM^{-1}s^{-1}$).[144-146] Most importantly, the contrast is sufficient for many drug delivery applications. For example, 5~10 mg/mL is a typical magnetic particle concentration in tumors for magnetic hyperthermia,[180] while our particles have several times faster relaxation rates than the gel even at the lowest concentrations of 50 μg/mL (R_2 is 37.7 s^{-1} for the nanorice, 29.3 s^{-1} for nanoeyes, and 20.0 s^{-1} for the hollow nanorice).

Nanoparticle Cytotoxicity Assay

Previous studies toxicity of ~80 nm iron oxide nanoparticles found no acute or subacute toxic effects by histologic or serologic studies in rats or beagle dogs which received a total of 3 mmol Fe/kg.[181] In order to study the potential cytotoxicity of the rare earth elements in the magnetic imaging probes (nanorice, nanoeyes, and hollow nanorice), an *in vitro* cytotoxicity test of hollow nanorice was performed on MCF-7 breast cancer

cells (Figure 5.16). The viability of the untreated cells was set as 100% in order to calculate the viability of the cells treated by different concentration of X-ray phosphors. Cell viability is not significantly affected by the Gd_2O_3:Eu nanoparticles up to concentration of at least 250 μg/ml (24 hr exposure).

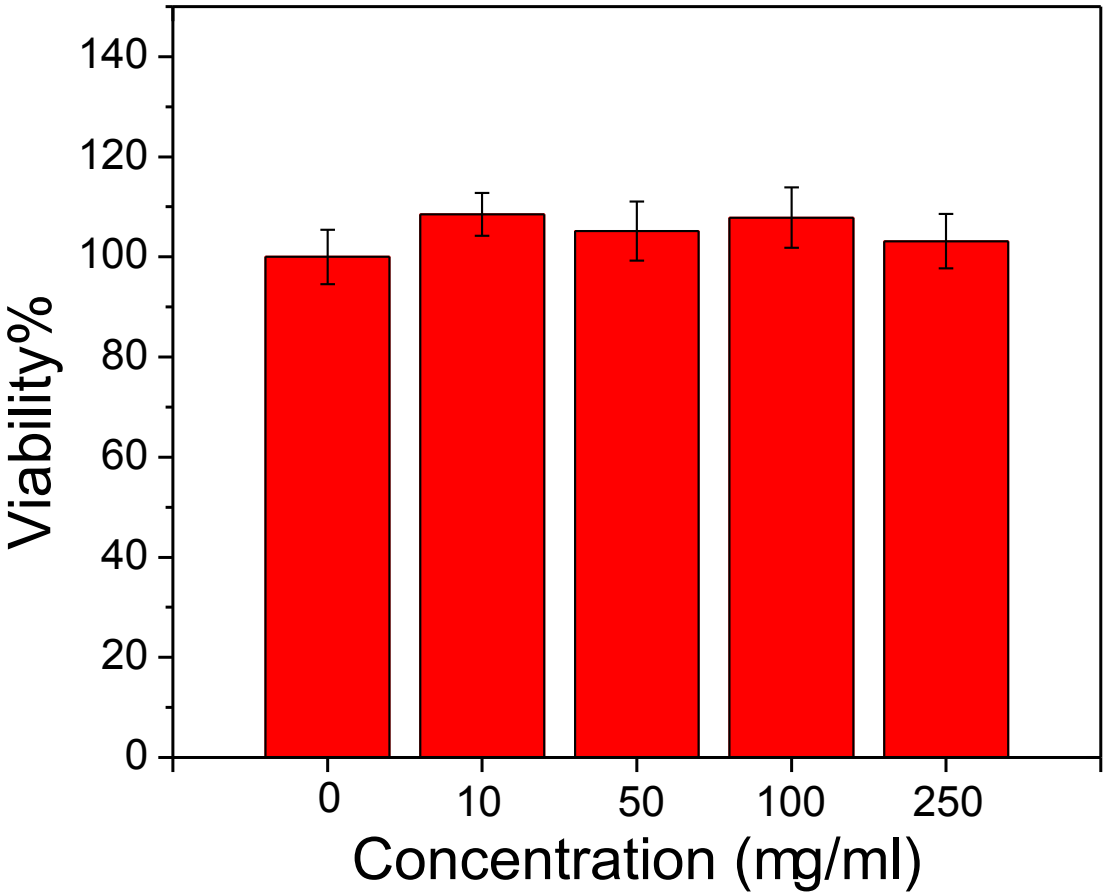

Figure 5.16 Cytotoxicity test for hollow nanorice (Gd_2O_3:Eu). Reproduced from Ref. 125 with permission from the Royal Society of Chemistry.

Conclusion

We successfully prepared magnetic luminescent nanoparticles using silica coated hematite as a template. The silica coating plays a critical role on the growth of phosphor

shell on the surface of the nanocores. After synthesis, the cores were made magnetic via high temperature reduction in H_2 and oxidization in air. The magnetic core size could be controlled while preserving the luminescent shell by dissolving the core in oxalic acid. Intermediate core sizes displayed both magnetic and luminescent properties. These novel magnetic luminescent nanoparticles are advantageous because they allow for magnetic separation and multimodal imaging with MRI, fluorescence and radioluminescence. We expect that such nanocomposites, combining the advantages of magnetism and luminescence, will find extensive applications in drug delivery and bioimaging. For example, the hollow structure in the partially dissolved iron oxide phosphor can be loaded with small dyes and drug molecules. Our synthesis technique is attractive because multifunctional particles can be made by coating the core templates with multiple layers of materials, each with a controlled thickness and composition. Different sizes, shapes (spherical and non-spherical), and structures (hollow and non-hollow) can be obtained by varying the shape and size of the hematite templates. Future work will study the effect of size and shape on magnetic, luminescent, and bio-distribution properties.

Experimental Section

Materials

Iron (III) chloride anhydrous and tetraethoxysilane (TEOS) were purchased from Sigma-Aldrich (St. Louis, MO, USA). Gadolinium Nitrate, Europium nitrate, potassium dihydrogen phosphate, and sulfur powder (99.5%) were purchased from obtained from Alfa Aesar (Ward Hill, MA). Ethanol (anhydrous, denatured), urea, oxalic acid, ammonium hydroxide, and nitric acid were obtained from BDH

Chemicals Ltd (Poole, Dorset, UK). Deionized (DI) water was purchased from EMD Chemicals Inc. (Gibbstown, NJ, USA). Polyvinylpyrrolidone (PVP K-30, MW 40,000) was purchased from Spectrum Chemicals (Gardena, CA). Agarose (melting point 88±1 ºC) was purchased from Shelton Scientific (Peosta, IA). All chemicals were used as received without further purification.

Synthesis of spindle-shaped hematite particle

Monodispersed spindle-shaped hematite nanoparticles with controllable aspect ratios were fabricated were prepared according to the method described by Ozaki and coworkers[182]. Typically, 100 ml of aqueous solution containing 2.0×10^{-2} M $FeCl_3$ and 4.0×10^{-4} M KH_2PO_4 were aged at 100 °C for 72 hours. The resulting precipitate was centrifuged and washed three times with water.

Synthesis of spindle-shaped hematite particle with silica shell

To obtain momodispersed hematite-silica core-shell nanoparticles, the PVP assisted coating method was used.[183] The spindle-shaped hematite particles synthesized above were dispersed ultrasonically to a 80 ml solution containing PVP (0.6 g), water (6 ml), and ethanol (74 ml). The suspension was stirred using a magnetic stir bar at room temperature and a solution of TEOS (270 μl) in 20 ml ethanol was added, followed by 4 ml of ammonia hydroxide. After 3h, the reaction mixture was precipitated by centrifuging at 4000 rpm for 16 min. The particles were washed three times with ethanol and centrifuged to collect the product.

Synthesis of spindle-shaped magnetic phosphors

The products above were suspended in 180 ml distilled water with 1.8 g PVP and 11.34 g oxalic acid (0.5 M) incubated at 60 °C for certain time. The hematite partially dissolved particles were collected by centrifugation and rinsed with DI water twice. The obtained particles were resuspended with 3 ml $Gd(NO_3)_3$, 1.5 ml $Eu(NO_3)_3$ (80 mM), and 1.8 g PVP in pure water to form 300 ml of solution. 18 g of urea was added to the solution and the solution was maintained at 80 °C for 90 min. The precursor of magnetic phosphor was collected by centrifugation. The precursor of spindle-shaped precursor was calcined in a furnace at 600 °C for 60 min. The powder was then transferred to a tube furnace with a H_2/N_2 (5%/95%) flow at 450 °C for 3h. After that, the sample was calcined in the tube furnace at 350 °C for 24 h.

Preparing nanocomposites for MR Imaging.

T_2 and T_2* MR measurements were acquired for the spindle-shaped γ-Fe_2O_3@SiO_2@Gd_2O_3:Eu particles at a series of concentrations (0.8 mg/ml, 0.4 mg/ml, 0.1 mg/ml, and 0.05 mg/ml). The particles were dispersed in 0.5% agarose gel at 80 °C and cooled to room temperature in NRM tubes to set the gel. The gel prevented settling and aggregation allowing MRI imaging several days after preparation.

Cell viability test

MCF-7 breast cancer cells were seeded at a density of 10,000 cells/well in a 96-well plate. Cells were stored at 37 °C at 5% CO_2 and attached to the plate overnight. Nanoparticles were suspended in media, sonicated for 10 minutes to disperse, and diluted to 250, 100, 50, and 10 μg/ml. Media was removed from wells and fresh media or nanoparticle in media was added to each well. Five repeats were done for each

concentration. Nanoparticles were incubated with cells overnight and the next day a Presto Blue assay (Life Technologies) was performed. Media was removed and 100 µl of a 1:9 ratio Presto Blue in culture media was added to each well. Cells were incubated at 37 °C and 5% CO_2 for 45 minutes. Fluorescent intensity was taken with a plate reader with an excitation wavelength of 560 nm and an emission wavelength of 590 nm. Fluorescent intensity for each concentration of nanoparticle was normalized as a percentage of the fluorescent intensity of the control cells. Percent viability averages were plotted with error bars of one standard deviation.

Intrumentation

Transmission and scanning electron microscopy (TEM) were performed on a H9500 operated at 300 kV and HD2000 microscope operated at 100 kV, respectively. An X-ray diffractometer (Rigaku; MiniFlex, Cu Kα) was used to characterize the XRD pattern of the magnetic phosphors. For fluorescence spectra, 480 nm light was used to excite the phosphors.

To measure radioluminescence, X-ray was generated by a mini X-ray tube (Amptek Inc. MA, USA), the X-ray tube was operated with tube voltage of 40 kV and tube current of 99 µA. The sample was mounted on a Leica Microscope (Leica DMI 5000M, Wetzlar, Germany) equipped with a DeltaNu DNS 300 spectrometer (Intevac-DeltaNu, Laramie, WY USA) with a 150 lines/mm grating blazed at 500 nm.

The Zeta-potential of the nanoparticles was determined using a Malvern Instruments Zetasizer Nano ZS with a 633 nm He-Ne laser. Prior to the experiment, the particles were diluted in distilled water (0.1 mg/ml). Magnetization measurements were

performed at the designated temperature using vibrating sample magnetometer (VSM) option of physical property measurement system (PPMS, Quantum Design, USA), with the applied magnetic field sweeping between +/- 3.0 Tesla at a rate of 50 Oe/sec. Determination of the gadolinium and iron content in a sample was performed by inductively coupled plasma (ICP)- (Optima 3100 RL; Perkin-Elmer).

In order to magnetically modulate the optical scattering from the magnetic luminescent particles, the particles were oriented and rotated in a magnetic field. A permanent magnet (NdBFe, 1" in diameter, 3" in length, magnetized through its diameter) was attached to a stepper motor and controlled by motion control software (Si Programmer; Applied Motion Products, Watsonville, CV). Every 3s, the permanent magnet was rotated 90º, first clockwise and then anticlockwise.

All MRI experiments were performed on a Varian 4.7T horizontal bore imaging system (Agilent Inc, Santa Clara, CA). Samples, contained in 5 mm NMR tubes, were placed in a 63 mm inner diameter quadrature RF coil for imaging. MRI gradient echo scout images were collected in all three imaging planes (axial, coronal, and sagittal) for subsequent image planning, with repetition time (TR) = 100 ms, echo time (TE) = 4 ms, number of slices =20, slice thickness =2, matrix size 128×128, field of view (FOV) = 40 mm×40 mm, number of acquisitions (NEX) =2. Relaxivity measurements were then collected on a single 2 mm thick imaging slice, approximately perpendicular to the long axis of the NMR tubes. The single slice, with FOV = 36 mm×36 mm, was imaged using a T_2-weighted multi-spin echo imaging sequence with TR = 3000, NEX = 10, echo spacing = 4ms, number of echoes = 10, and 128 x 128 matrix. T_2*-weighted

images were collected using a gradient echo imaging sequence with TR = 500 ms, flip = 20°, 128×128 matrix, NEX = 10, and echo times = [1.5, 3, 4.5, 9, 15 ms]. Following data collection, images were analyzed using Matlab 2011a (The Mathworks, Inc., Natick, MA). Regions of interest (ROI's), encompassing approximately 70-80 voxels, were manually drawn in each sample, and the signals from those voxels averaged to obtain a mean signal for each sample. The same ROI was used to calculate the mean signal of the sample across all echo times.

CHAPTER SIX

VI. CONCLUSIONS AND FUTURE DERECTIONS

In chapter II and III, we developed a novel technique (XEOL) for in situ chemical imaging through tissue with high spatial resolution. When the X-ray excited luminescence combines with suitable chemical sensing dyes (fluorescent and colorimetric indicators), a background-free radioluminescence based pH sensor was fabricated. The high spatial resolution (0.30 mm) through 10 mm of chicken breast was demonstrated by detecting a two-color X-ray phosphor film. We then extended the XEOL technique to imaging silver dissolution under 10 mm pork where it also offers a combination of high spatial resolution (limited by the X-ray beam width) and high sensitivity optical detection. Fluorescent and colorimetric indicators and stains are widely used for histology and biomedical research because of their high sensitivity and specificity for a wide variety of analytes. XEOL indicators combine the advantages of optical indicators with high resolution, low background imaging from scanning X-ray excitation. A particularly attractive application is imaging chemical (e.g biofilm) and mechanical changes on implanted medical devices, which can become infected. Many analytes can be measured (e.g. pH, silver metal dissolution, oxygen, and protease activity). Relatively thick phosphor films may be used to improve X-ray luminescence capture, and signal strength especially at high energies. The two dimensional nature of the surfaces simplifies and speeds up imaging. An important challenge will be to minimize the spectral distortion caused by wavelength dependent tissue scattering and absorption, especially for deeply implanted devices. Several techniques are possible, including calculation of spectral

ratios using closely spaced spectral peaks, use of spectral reference regions near to the sensor region, and lifetime-based imaging. Another technical challenge will be integrating the sensor film onto the implanted device while minimizing delamination, abrasion, and reducing bacterial adhesion. After sensor development, the next step will be integration of sensing with active components such as combining magnetic or photothermal hyperthermia and drug release with local pH sensors to monitor the effect of therapies on local biofilm chemistry.

In addition to chemical analysis on surfaces, XEOL can be used for three dimensional tomography similar to X-ray luminescence tomography (XLT) and limited-angle XLT. For example, our group has developed hollow nanoparticles with encapsulated magnetic iron oxide nanoparticles. The luminescence is quenched by iron oxide in the core and increases as the iron oxide is etched.[125] We have also encapsulated indicator dyes and are studying leaching rate as a function of pH. In future we expect that these types of sensors will be useful for local drug delivery while measuring the amount of drug delivered in time. Additional sensors with unique optical emission spectra can be used for simultaneously studying changes in cellular chemistry such as endosomal pH changes upon apoptosis. Such *in situ* sensors will be useful for optimizing therapeutic agents and monitoring effectiveness.

Future work involves using chemical indicator dyes for oxygen and other analytes, using narrower X-ray beams and more sensitive detection optics for two dimensional chemical imaging and tomography, and developing a portable imaging system. Two dimensional chemical imaging will be especially useful for measuring

chemical changes on a surface, such as in situ detection of acidosis, hypoxia, and hydroxyapatite degradation on implanted devices with bacterial colonies. Phosphoresent lifetime measurements are alternative approaches which do not depend on scattering or absorption. We may also measure the lifetime of long-lived Oxygen sensing molecules such as Ru(dpp) or platinum complexes. These dyes are quenched by oxygen and serve as oxygen sensors. We can also use phosphors with relatively fast decay time to distinguish the lifetime of the chemical indicator from the phosphors or use long lifetime phosphors and measure the quenching lifetime caused by adsorbed acceptor molecules or plasmonic nanoparticles. Recent developments in X-ray imaging and contrast agents are opening up new opportunities for high-resolution functional imaging. In all cases, a key advantage of XEOL is that high resolution images can be generated because X-rays can penetrate deeply through tissue and have relatively low scattering coefficients. The images can also be co-registered with structural information from X-ray attenuation imaging and integrated with other imaging techniques such as diffuse optical fluorescence tomography and MRI. The main disadvantage of X-ray imaging, however, is that large X-ray doses cause short term tissue damage/radiation sickness, and increase the long term risk of developing cancer.[47, 184-185] Consequently, the challenge will be to maximize the analytical sensitivity, specificity, image resolution, and acquisition rate while minimizing the X-ray dose, contrast concentration, and contrast toxicity. The use of up-conversion nanophosphors which are able to emit visible light under near infrared light excitation is alterative approach to address the safety concern of X-ray but at cost of spatial resolution.[186-187]

A wide variety of contrast agents with unique spectra have been developed for phosphor film applications and these can be used for X-ray luminescence tomography contrast (see Table. 1). New X-ray excited luminescent nanoparticles are expected to explored to meet the application of XEOL. High optical collection efficiencies are also required using large area photodetectors and potentially integrating sphere optics. In limited angle configurations the X-ray luminescence tomography images can be acquired rapidly, although with some loss of resolution along one dimension.[56] We expect that continuing development of phosphor nanomaterials, targeting moieties, and instrumentation will greatly expand the utility of X-ray luminescence tomography. Many of the phosphor materials also have large magnetic permeability and serve as effective MRI contrast agents.[125]

In Chapter IV, we present a flexible template-directed method to produce non-sphrical radioluminescent nanocapsules for an anticancer drug (DOX) carrier, monitor release kinetics, and magnetic drug carrier. The hollow radioluminescence nanocapsules demonstrate a multifunctional platform with an X-ray excited optical luminescence (XEOL) spectrum that changes during drug release. These nanocapsules are also paramagnetic, allowing them to be used as MRI imaging agents. The future work will focus on the study of toxicity of DOX loaded nanocapsules, pH dependent drug release in vivo, target DOX loaded capsules to tumors, and measure *in situ* release rates and tumor growth for various nanocapsule sizes, shapes, and surface chemistries. In order to reduce required X-ray dose to capsule enough X-ray excited luminescence, more studies will focus on enhance the luminescence of anophosphors. Some templates such as carbon

nanospheres which can be decomposed in the synthesis of nanophosphors is one of the approaches to simplify the process of nanocarrier synthesis. Some flux (Na_2CO_3, NaF, etc.) used in traditional solid reaction can successfully improve the luminescence of X-ray phosphors. However, the size (> 1 μm) of phosphors are not suitable for molecular imaging or drug delivery. Novel method based on the use of flux are promising to obtain ultrabright X-ray phosphor in nanosize. Combination of up conversion phosphors which can be excited by near infrared and emit visible light with X-ray phosphor is alternative approach to reduce the dose of X-ray used to locate the drug nanocarrier.

Chapter V provides a partially etching method to fabricated magnetic luminescent nanocapsules. These magnetic capsules can serve good contrast agent for XEOL, T_2 weighted MRI, and magnetic nanocarriers. In the future, we plan to target the tumor *in vivo* by applying magnetic field on the drug loaded magnetic capsules. Novel method should also be explored to improve the luminescence intensity such as the use of flux to improve the X-ray excited luminescence or coating brighter up-conversion phosphor on iron oxide nancores. In order to increase the saturated magnetization of the nanocarriers, fabricating stronger magnetic materials such as pure iron nanoparticles need be studied because these materials shows ultra-high saturated magnetization (212 emu/g)[188] and relaxivity (330 $mM^{-1}s^{-1}$) for T_2-weighted magnetic resonance imaging [189].

Overall, XEOL-based multifunctional X-ray nanophosphors are highly promising for rapid and sensitive chemical analysis in tissue or the surface of implanted medical devices. With further improvements in instrumentation and contrast agents, we expect a bright future for high resolution molecular imaging with X-ray nanophosphors.

APPENDICES

Appendix A

Copy right permission from the Royal Society of Chemistry

CLEMSON UNIVERSITY

Hongyu Chen <hongyuc@g.clemson.edu>

RE: Website Email: Copyright permission requests

CONTRACTS-COPYRIGHT (shared) <Contracts-Copyright@rsc.org> Wed, Nov 14, 2012 at 4:04 AM
To: Hongyu Chen <hongyuc@clemson.edu>

Dear Dr Chen

The Royal Society of Chemistry (RSC) hereby grants permission for the use of your paper(s) specified below in the printed and microfilm version of your thesis. You may also make available the PDF version of your paper(s) that the RSC sent to the corresponding author(s) of your paper(s) upon publication of the paper(s) in the following ways: in your thesis via any website that your university may have for the deposition of theses, via your university's Intranet or via your own personal website. We are however unable to grant you permission to include the PDF version of the paper(s) on its own in your institutional repository. The Royal Society of Chemistry is a signatory to the STM Guidelines on Permissions (available on request).

Please note that if the material specified below or any part of it appears with credit or acknowledgement to a third party then you must also secure permission from that third party before reproducing that material.

Please ensure that the thesis states the following:

Reproduced by permission of The Royal Society of Chemistry

and include a link to the paper on the Royal Society of Chemistry's website.

Please ensure that your co-authors are aware that you are including the paper in your thesis.

Regards

Gill Cockhead

Publishing Contracts & Copyright Executive

Gill Cockhead (Mrs), Publishing Contracts & Copyright Executive

Royal Society of Chemistry, Thomas Graham House

Science Park, Milton Road, Cambridge CB4 0WF, UK

Tel +44 (0) 1223 432134, Fax +44 (0) 1223 423623

http://www.rsc.org

-----Original Message-----

From: Hongyu Chen [mailto:hongyuc@clemson.edu]

Sent: 09 November 2012 14:20

To: CONTRACTS-COPYRIGHT (shared)

Subject: Website Email: Copyright permission requests

To: Gill Cockhead

This Email was sent from the following rsc.org page:

/AboutUs/Copyright/Permissionrequests.asp (http://www.rsc.org/AboutUs/EmailPage.asp?address=nzy%7F%7Dln%7F%7E8nz%7B%u201E%7Dtrs%7FK%7D%7En9z%7Dr&CCaddress=&name=Gill%20Cockhead&url=/AboutUs/Copyright/Permissionrequests.asp)

Hi Gill,

I am preparing my thesis entitled "Multifunctional nanophosphors for tissue imaging and drug delivery" I would appreciate permission to reuse the following items in my thesis.

Item 1:

Title:Optical imaging in tissue with X-ray excited luminescent sensors

Author: Hongyu Chen,David E. Longfield,Venkata S. Varahagiri,KhanhVan T. Nguyen,Amanda L. Patrick,Haijun Qian,Donald G. VanDerveer,Jeffrey N. Anker

Publication:Analyst

Publisher:Royal Society of Chemistry

Date: Jun 21, 2011

Item 2:

Title:Magnetic and optical properties of multifunctional core-shell radioluminescence nanoparticles Author:Hongyu Chen,Daniel C. Colvin,Bin Qi,Thomas Moore,Jian He,O. Thompson Mefford,Frank Alexis,John C. Gore,Jeffrey N. Anker Publication:Journal of Materials Chemistry Publisher:Royal Society of Chemistry Date:May 25, 2012

Item 3:

Title:Advances in functional X-ray imaging techniques and contrast agents

Author: Hongyu Chen,Melissa M. Rogalski,Jeffrey N. Anker

Publication:Physical Chemistry Chemical Physics Publisher:Royal Society of Chemistry Date:Aug 9, 2012

Yours sincerely,

Hongyu Chen

Membership No. :

Appendix B

Copy right permission from the American Chemistry Society

CLEMSON UNIVERSITY

Hongyu Chen <hongyuc@g.clemson.edu>

copyright permission requests

EIC Office <eic@anchem.acs.org> Tue, Nov 13, 2012 at 4:09 PM
To: Hongyu Chen <hongyuc@g.clemson.edu>

Dear Hongyu Chen:

You have my permission to use this article "High-Resolution Chemical Imaging through Tissue with an X-ray Scintillator Sensor" in your thesis as long as the correct citations are made as directed in the ACS Thesis/Dissertation Policy and the ACS Journal Publishing Agreement.

Sincerely,

Prof. Jonathan V. Sweedler

Editor-in-Chief

Analytical Chemistry

Phone: 217-244-7359

Fax: 202-513-8699

Email: eic@anchem.acs.org

REFERENCES

1. Nikl, M., *Measurement Science and Technology* 2006, ***17***, R37.

2. Röntgen, W. C., *Sitz Ber Phys Med Ges Wuerzb* 1895, ***9***, 132-141.

3. Dorenbos, P., *Nuclear Instruments and Methods in Physics Research Section A: Accelerators, Spectrometers, Detectors and Associated Equipment* 2002, ***486***, 208-213.

4. Holl, I., Lorenz, E. and Mageras, G., *Nuclear Science, IEEE Transactions on* 1988, ***35***, 105-109.

5. Sakai, E., *Nuclear Science, IEEE Transactions on* 1987, ***34***, 418-422.

6. Valentine, J. D., Moses, W. W., Derenzo, S. E., Wehe, D. K. and Knoll, G. F., *Nuclear Instruments and Methods in Physics Research Section A: Accelerators, Spectrometers, Detectors and Associated Equipment* 1993, ***325***, 147-157.

7. De Haas, J. T. M., Dorenbos, P. and Van Eijk, C., *Nuclear Instruments and Methods in Physics Research Section A: Accelerators, Spectrometers, Detectors and Associated Equipment* 2005, ***537***, 97-100.

8. De Haas, J. T. M. and Dorenbos, P., *Nuclear Science, IEEE Transactions on* 2008, ***55***, 1086-1092.

9. Syntfeld, A., Moszynski, M., Arlt, R., Balcerzyk, M., Kapusta, M., Majorov, M., Marcinkowski, R., Schotanus, P., Swoboda, M. and Wolski, D., *Nuclear Science Symposium Conference Record, 2004 IEEE* **2004**, pp. 1545-1550 Vol. 1543.

10. Murray, R., *Nuclear Instruments* 1958, ***2***, 237-248.

11. van Loef, E. V. D., Dorenbos, P., van Eijk, C. W. E., Krämer, K. W. and Güdel, H. U., *Nuclear Instruments and Methods in Physics Research Section A: Accelerators, Spectrometers, Detectors and Associated Equipment* 2002, ***486***, 254-258.

12. van Loef, E. V. D., Dorenbos, P., van Eijk, C. W. E., Krämer, K. W. and Güdel, H. U., *Nuclear Instruments and Methods in Physics Research Section A: Accelerators, Spectrometers, Detectors and Associated Equipment* 2005, ***537***, 232-236.

13. Menefee, J., Swinehart, C. and O'Dell, E., *Nuclear Science, IEEE Transactions on* 1966, ***13***, 720-724.

14. van Loef, E. V., Wilson, C. M., Cherepy, N. J., Hull, G., Payne, S. A., Choong, W. S., Moses, W. W. and Shah, K. S., *Nuclear Science, IEEE Transactions on* 2009, ***56***, 869-872.

15. Ronda, C. R., *Luminescence: from theory to applications*, LibreDigital, **2008**, p.

16. Brixner, L. H., *Materials Chemistry and Physics* 1987, ***16***, 253-281.

17. Marvin J, W., *Journal of Luminescence* 2002, ***100***, 35-45.

18. Issler, S. L. and Torardi, C. C., *Journal of Alloys and Compounds* 1995, ***229***, 54-65.

19. Derenzo, S. E. and Moses, W. W., *Heavy scintillators for scientific and industrial applications* 1993, 125-135.

20. van Loef, E. V., Higgins, W. M., Glodo, J., Brecher, C., Lempicki, A., Venkataramani, V., Moses, W. W., Derenzo, S. E. and Shah, K. S., *Nuclear Science, IEEE Transactions on* 2007, ***54***, 741-743.

21. Greskovich, C. and Duclos, S., *Annual review of materials science* 1997, ***27***, 69-88.

22. Eijk, C. W. E. v., *Physics in Medicine and Biology* 2002, ***47***, R85.

23. Weber, M. J. and Monchamp, R. R., *Journal of Applied Physics* 1973, ***44***, 5495-5499.

24. Zdesenko, Y. G., Avignone Iii, F., Brudanin, V., Danevich, F., Nagorny, S., Solsky, I. and Tretyak, V., *Nuclear Instruments and Methods in Physics Research Section A: Accelerators, Spectrometers, Detectors and Associated Equipment* 2005, ***538***, 657-667.

25. Moszyński, M., Balcerzyk, M., Czarnacki, W., Nassalski, A., Szczęśniak, T., Kraus, H., Mikhailik, V. and Solskii, I., *Nuclear Instruments and Methods in Physics Research Section A: Accelerators, Spectrometers, Detectors and Associated Equipment* 2005, ***553***, 578-591.

26. Lempicki, A., Randles, M. H., Wisniewski, D., Balcerzyk, M., Brecher, C. and Wojtowicz, A. J., *Nuclear Science, IEEE Transactions on* 1995, ***42***, 280-284.

27. Moszynski, M., Kapusta, M., Mayhugh, M., Wolski, D. and Flyckt, S. O., *Nuclear Science, IEEE Transactions on* 1997, ***44***, 1052-1061.

28. Mihóková, E., Nikl, M., Mareš, J. A., Beitlerová, A., Vedda, A., Nejezchleb, K., Blažek, K. and D'Ambrosio, C., *Journal of Luminescence* 2007, ***126***, 77-80.

29. Melcher, C., Manente, R. and Schweitzer, J., *Nuclear Science, IEEE Transactions on* 1989, ***36***, 1188-1192.

30. Mares, J. A., Beitlerova, A., Nikl, M., Solovieva, N., D'Ambrosio, C., Blazek, K., Maly, P., Nejezchleb, K. and de Notaristefani, F., *Radiation Measurements* 2004, ***38***, 353-357.

31. Mares, J. A., Nikl, M., Mihokova, E., Kvapil, J., Giba, J. and Blazek, K., *Journal of Luminescence* 1997, ***72–74***, 737-739.

32. Dujardin, C., Pedrini, C., Blanc, W., Gacon, J., Spijker, J. C., Frijns, O., Eijk, C. W. E., Dorenbos, P., Chen, R. and Fremout, A., *Journal of Physics: Condensed Matter* 1998, ***10***, 3061.

33. Melcher, C. and Schweitzer, J., **1991**, pp. 228-231 vol. 221.

34. van Eijk, C. W. E., *Nuclear Instruments and Methods in Physics Research Section A: Accelerators, Spectrometers, Detectors and Associated Equipment* 2003, ***509***, 17-25.

35. Kang, Y., Park, S., Lenggoro, I. and Okuyama, K., *Journal of Physics and Chemistry of Solids* 1999, ***60***, 379-384.

36. Okumura, M., Tamatani, M., Matsuda, N., Takahara, T. and Fukuta, Y. in *Ceramic scintillator, method for producing same, and x-ray detector and x-ray CT imaging equipment using same*, *Vol.* U.S. Patent 6,384,417, **2002**.

37. Deych, R. and Dolazza, E., *Sensors Applications Symposium, 2007. SAS '07. IEEE* **2007**, pp. 1-6.

38. Takagi, K. and Fukazawa, T., *Applied Physics Letters* 1983, ***42***, 43-45.

39. Ishibashi, H., Shimizu, K., Susa, K. and Kubota, S., *Nuclear Science, IEEE Transactions on* 1989, ***36***, 170-172.

40. Feldmann, C., Jüstel, T., Ronda, C. R. and Schmidt, P. J., *Advanced Functional Materials* 2003, ***13***, 511-516.

41. Pratx, G., Carpenter, C. M., Sun, C., Rao, R. P. and Xing, L., *Optics letters* 2010, ***35***, 3345-3347.

42. Pratx, G., Carpenter, C. M., Sun, C. and Xing, L., *Medical Imaging, IEEE Transactions on* 2010, ***29***, 1992-1999.

43. Luo, X. and Cao, W., *Science in China Series B: Chemistry* 2007, ***50***, 505-513.

44. Hu, L., Yan, B., Zhang, J. and Wang, X., *Journal of Physics D: Applied Physics* 2007, ***40***, 7519.

45. Mao, S., Liu, Q., Gu, M., Mao, D. and Chang, C., *Journal of Alloys and Compounds* 2008, ***465***, 367-374.

46. Osseni, S. A., Lechevallier, S., Verelst, M., Dujardin, C., Dexpert-Ghys, J., Neumeyer, D., Leclercq, M., Baaziz, H., Cussac, D., Santran, V. and Mauricot, R., *Journal of Materials Chemistry* 2011, ***21***, 18365-18372.

47. Morgan, N. Y., Kramer-Marek, G., Smith, P. D., Camphausen, K. and Capala, J., *Radiation Research* 2009, ***171***, 236-244.

48. Chen, W. and Zhang, J., *Journal of Nanoscience and Nanotechnology* 2006, ***6***, 1159-1166.

49. Moronne, M. M., *Ultramicroscopy* 1999, ***77***, 23-36.

50. Adam, J.-F., Moy, J.-P. and Susini, J., *Review of Scientific Instruments* 2005, ***76***, 091301-091301-091315.

51. Shroff, H., Galbraith, C. G., Galbraith, J. A. and Betzig, E., *Nat Meth* 2008, ***5***, 417-423.

52. Hein, B., Willig, K. I. and Hell, S. W., *Proceedings of the National Academy of Sciences* 2008, ***105***, 14271.

53. Hecht, B., Sick, B., Wild, U. P., Deckert, V., Zenobi, R., Martin, O. J. F. and Pohl, D. W., *The Journal of Chemical Physics* 2000, ***112***, 7761-7774.

54. Pratx, G., Carpenter, C. M., Sun, C. and Lei, X., *Medical Imaging, IEEE Transactions on* 2010, ***29***, 1992-1999.

55. Carpenter, C., Sun, C., Pratx, G., Rao, R. and Xing, L., *Medical physics* 2010, ***37***, 4011.

56. Carpenter, C., Pratx, G., Sun, C. and Xing, L., *Phys. Med. Bio.* 2011, ***56***, 3487.

57. Liu, Y., Chen, W., Wang, S. and Joly, A. G., *Applied Physics Letters* 2008, ***92***, 043901.

58. Wang, G., Cong, W., Durairaj, K., Qian, X., Shen, H., Sinn, P., Hoffman, E., McLennan, G. and Henry, M., *Opt. Express* 2006, ***14***, 7801-7809.

59. Song, Y., You, H., Huang, Y., Yang, M., Zheng, Y., Zhang, L. and Guo, N., *Inorganic Chemistry* 2010, ***49***, 11499-11504.

60. Sun, C., Pratx, G., Carpenter, C. M., Liu, H., Cheng, Z., Gambhir, S. S. and Xing, L., *Advanced Materials* 2011, ***23***, H195-H199.

61. Zimmerli, W., *Best Practice & Research Clinical Rheumatology* 2006, ***20***, 1045-1063.

62. Ehrlich, G. D., Stoodley, P., Kathju, S., Zhao, Y., McLeod, B. R., Balaban, N., Hu, F. Z., Sotereanos, N. G., Costerton, J. W. and Stewart, P. S., *Clinical orthopaedics and related research* 2005, 59.

63. Gore, J., Yankeelov, T. and Peterson, T., *Journal of Nuclear Medicine* 2009, ***50***, 999.

64. Theer, P., Hasan, M. T. and Denk, W., *Opt. Lett.* 2003, ***28***, 1022-1024.

65. Liu, Y., Chen, W., Wang, S. and Joly, A., *Applied Physics Letters* 2008, ***92***, 043901.

66. Chen, W., Wang, S., Westcott, S. and Zhang, J. in *Energy-transfer nanocomposite materials and methods of making and using same*, *Vol.* U.S. Patent 7,538,329, **2009**.

67. Novotny, L. in *Chapter 5 The history of near-field optics*, *Vol. Volume 50* (Ed. Wolf, E.), Elsevier, **2007**, pp. 137-184.

68. Dunn, R. C., *Chemical reviews* 1999, ***99***, 2891-2928.

69. Hidalgo, G., Burns, A., Herz, E., Hay, A. G., Houston, P. L., Wiesner, U. and Lion, L. W., *Applied and Environmental Microbiology* 2009, ***75***, 7426-7435.

70. Davies, D., *Nat Rev Drug Discov* 2003, ***2***, 114-122.

71. Wang, P. and Cargill III, G., *Journal of Applied Physics* 1997, ***81***, 1031.

72. Hirano, S. and Suzuki, K. T., *Environmental health perspectives* 1996, ***104***, 85.

73. Künnemeyer, J., Terborg, L., Meermann, B. r., Brauckmann, C., Möller, I., Scheffer, A. and Karst, U., *Environmental Science & Technology* 2009, ***43***, 2884-2890.

74. Palmer, R. J., Butenhoff, J. L. and Stevens, J. B., *Environmental research* 1987, ***43***, 142-156.

75. Chatterjee, D. K., Rufaihah, A. J. and Zhang, Y., *Biomaterials* 2008, ***29***, 937-943.

76. Popovtzer, R., Agrawal, A., Kotov, N. A., Popovtzer, A., Balter, J., Carey, T. E. and Kopelman, R., *Nano Letters* 2008, ***8***, 4593-4596.

77. Troy, T., Jekic-McMullen, D., Sambucetti, L. and Rice, B., *Molecular Imaging* 2004, ***3***, 9.

78. Farrell, T. J., Patterson, M. S. and Wilson, B., *Medical Physics* 1992, ***19***, 879-888.

79. Marquez, G., Wang, L. V., Lin, S.-P., Schwartz, J. A. and Thomsen, S. L., *Appl. Opt.* 1998, ***37***, 798-804.

80. Zhang, H. F., Maslov, K., Stoica, G. and Wang, L. V., *Nat Biotech* 2006, ***24***, 848-851.

81. Schuler, M., Owen, G. R., Hamilton, D. W., de Wild, M., Textor, M., Brunette, D. M. and Tosatti, S. G. P., *Biomaterials* 2006, ***27***, 4003-4015.

82. Helmchen, F. and Denk, W., *Nature methods* 2005, ***2***, 932-940.

83. Wang, G., Cong, W., Durairaj, K., Qian, X., Shen, H., Sinn, P., Hoffman, E., McLennan, G. and Henry, M., *Optics Express* 2006, ***14***, 7801-7809.

84. Gore, J. C., Yankeelov, T. E. and Peterson, T., *Journal of Nuclear Medicine* 2009, ***50***, 999.

85. Gambhir, S. S., *Nat Rev Cancer* 2002, ***2***, 683-693.

86. Jaszczak, R. J., Coleman, R. E. and Whitehead, F. R., *Nuclear Science, IEEE Transactions on* 1981, ***28***, 69-80.

87. Robertson, R. and et al., *Physics in Medicine and Biology* 2009, ***54***, N355.

88. Cavouras, D., Kandarakis, I., Nomicos, C. D., Bakas, A. and Panayiotakis, G. S., *Radiation Measurements* 2000, ***32***, 5-13.

89. Lankinen, A., Svensk, O., Mattila, M., Tuomi, T., Lipsanen, H., McNally, P., O'Reilly, L. and Paulmann, C., *Journal of X-Ray Science and Technology* 2008, ***16***, 215-220.

90. Naftel, S., Yiu, Y., Sham, T. and Yates, B., *Journal of Electron Spectroscopy and Related Phenomena* 2001, ***119***, 215-220.

91. Hein, B., Willig, K. and Hell, S., *Proceedings of the National Academy of Sciences* 2008, ***105***, 14271.

92. Rust, M. J., Bates, M. and Zhuang, X., *Nat Meth* 2006, ***3***, 793-796.

93. Anker, J. N., Hall, W. P., Lyandres, O., Shah, N. C., Zhao, J. and Van Duyne, R. P., *Nat Mater* 2008, ***7***, 442-453.

94. Daniel, W., Han, M., Lee, J. and Mirkin, C., *Journal of the American Chemical Society* 2009, ***131***, 6362-6363.

95. Lytton Jean, A., Gibbs Davis, J., Long, H., Schatz, G., Mirkin, C. and Nguyen, S., *Advanced Materials* 2009, ***21***, 706-709.

96. Gosheger, G., Hardes, J., Ahrens, H., Streitburger, A., Buerger, H., Erren, M., Gunsel, A., Kemper, F., Winkelmann, W. and von Eiff, C., *Biomaterials* 2004, ***25***, 5547-5556.

97. Dubertret, B., Calame, M. and Libchaber, A., *Nature biotechnology* 2001, ***19***, 365-370.

98. Pal, T., Jana, N. and Sau, T., *Radiation Physics and Chemistry* 1997, ***49***, 127-130.

99. Bosworth, N. and Towers, P., *Nature* 1989, ***341***, 167-168.

100. Glickman, J., Schmid, A. and Ferrand, S., *Assay and drug development technologies* 2008, ***6***, 433-455.

101. Gorokhova, E. I., Demidenko, V. A., Eron'ko, S. B., Oreshchenko, E. A., Rodny, P. A. and Mikhrin, S. B., *J. Opt. Technol.* 2010, ***77***, 50-58.

102. Anan'eva, G. V., Gorokhova, E. I., Demidenko, V. A., Parfinskii, V. A. and Khristich, O. A., *J. Opt. Technol.* 2005, ***72***, 58-61.

103. Gechev, T. and Hille, J., *The Journal of cell biology* 2005, ***168***, 17.

104. Pellinen, R., Korhonen, M., Tauriainen, A., Palva, E. and Kangasjarvi, J., *Plant Physiology* 2002, ***130***, 549.

105. Kittler, S., Greulich, C., Diendorf, J., Köller, M. and Epple, M., *Chemistry of Materials* 2010, ***22***, 4548-4554.

106. Geranio, L., Heuberger, M. and Nowack, B., *Environmental Science & Technology* 2009, ***43***, 8113-8118.

107. Ivanova, E., Hasan, J., Truong, V., Wang, J., Raveggi, M., Fluke, C. and Crawford, R., *Applied Microbiology and Biotechnology* 2011, ***91***, 1149-1157.

108. Liu, J. and Hurt, R. H., *Environmental Science & Technology* 2010, ***44***, 2169-2175.

109. Ho, C.-M., Yau, S. K.-W., Lok, C.-N., So, M.-H. and Che, C.-M., *Chemistry – An Asian Journal* 2010, ***5***, 285-293.

110. Niethammer, P., Grabher, C., Look, A. and Mitchison, T., *Nature* 2009, ***459***, 996-999.

111. Test, S. and Weiss, S., *Journal of Biological Chemistry* 1984, ***259***, 399.

112. Chen, H., Patrick, A. L., Yang, Z., VanDerveer, D. G. and Anker, J. N., *Analytical Chemistry* 2011, ***83***, 5045-5049.

113. Morelli, D., Ménard, S., Colnaghi, M. I. and Balsari, A., *Cancer Research* 1996, ***56***, 2082-2085.

114. Von Hoff, D. D., Layard, M. W., Basa, P., Davis, J. H. L., Von Hoff, A. L., Rozencweig, M. and Muggia, F. M., *Annals of Internal Medicine* 1979, ***91***, 710-717.

115. Gabizon, A., Shmeeda, H. and Barenholz, Y., *Clinical Pharmacokinetics* 2003, ***42***, 419-436.

116. Lee, E. S., Na, K. and Bae, Y. H., *Journal of Controlled Release* 2005, ***103***, 405-418.

117. Lee, E. S., Na, K. and Bae, Y. H., *Nano Letters* 2005, ***5***, 325-329.

118. Andersson, J., Rosenholm, J., Areva, S. and Lindén, M., *Chemistry of Materials* 2004, ***16***, 4160-4167.

119. Barbé, C., Bartlett, J., Kong, L., Finnie, K., Lin, H. Q., Larkin, M., Calleja, S., Bush, A. and Calleja, G., *Advanced Materials* 2004, ***16***, 1959-1966.

120. Lai, C. Y., Trewyn, B. G., Jeftinija, D. M., Jeftinija, K., Xu, S., Jeftinija, S. and Victor, S. Y. L., *Journal of the American Chemical Society* 2003, ***125***, 4451-4459.

121. Zhu, Y., Shi, J., Shen, W., Dong, X., Feng, J., Ruan, M. and Li, Y., *Angewandte Chemie* 2005, ***117***, 5213-5217.

122. Eijk, C. W. E., *Physics in Medicine and Biology* 2002, ***47***, R85.

123. Chen, H., Longfield, D. E., Varahagiri, V. S., Nguyen, K. T., Patrick, A. L., Qian, H., VanDerveer, D. G. and Anker, J. N., *Analyst* 2011, ***136***, 3438-3445.

124. Chen, H., Rogalski, M. M. and Anker, J. N., *Physical Chemistry Chemical Physics* 2012.

125. Chen, H., Colvin, D. C., Qi, B., Moore, T., He, J., Mefford, O. T., Alexis, F., Gore, J. C. and Anker, J. N., *Journal of Materials Chemistry* 2012, ***22***, 12802-12809.

126. Chen, H., Moore, T., Qi, B., Colvin, D. C., Jelen, E. K., Hitchcock, D. A., He, J., Mefford, O. T., Gore, J. C., Alexis, F. and Anker, J. N., *ACS Nano* 2012, (under review).

127. Decuzzi, P., Godin, B., Tanaka, T., Lee, S. Y., Chiappini, C., Liu, X. and Ferrari, M., *Journal of Controlled Release* 2010, ***141***, 320-327.

128. Gratton, S. E. A., Ropp, P. A., Pohlhaus, P. D., Luft, J. C., Madden, V. J., Napier, M. E. and DeSimone, J. M., *Proceedings of the National Academy of Sciences* 2008, ***105***, 11613.

129. Champion, J. A. and Mitragotri, S., *Proceedings of the National Academy of Sciences of the United States of America* 2006, ***103***, 4930-4934.

130. Huang, X., Li, L., Liu, T., Hao, N., Liu, H., Chen, D. and Tang, F., *ACS Nano* 2011, ***5***, 5390-5399.

131. Ishikawa, T. and Matijevic, E., *Langmuir* 1988, ***4***, 26-31.

132. Ozaki, M., Kratohvil, S. and Matijević, E., *Journal of colloid and interface science* 1984, ***102***, 146-151.

133. Piao, Y., Kim, J., Na, H. B., Kim, D., Baek, J. S., Ko, M. K., Lee, J. H., Shokouhimehr, M. and Hyeon, T., *Nat Mater* 2008, ***7***, 242-247.

134. Franz, K. A., Kehr, W. G., Siggel, A., Wieczoreck, J. and Adam, W. in *Luminescent Materials*, *Vol.* Wiley-VCH Verlag GmbH & Co. KGaA, **2000**.

135. Sukhorukov, G., Dähne, L., Hartmann, J., Donath, E. and Möhwald, H., *Advanced Materials* 2000, ***12***, 112-115.

136. Ibarz, G., Dähne, L., Donath, E. and Möhwald, H., *Advanced Materials* 2001, ***13***, 1324-1327.

137. Shchukin, D. G., Sukhorukov, G. B. and Möhwald, H., *Angewandte Chemie* 2003, ***115***, 4610-4613.

138. Zhu, Y., Shi, J., Shen, W., Dong, X., Feng, J., Ruan, M. and Li, Y., *Angewandte Chemie International Edition* 2005, ***44***, 5083-5087.

139. Petoral, R. M., Söderlind, F., Klasson, A., Suska, A., Fortin, M. A., Abrikossova, N., Selegård, L. a., Käll, P.-O., Engström, M. and Uvdal, K., *The Journal of Physical Chemistry C* 2009, ***113***, 6913-6920.

140. Park, J. Y., Baek, M. J., Choi, E. S., Woo, S., Kim, J. H., Kim, T. J., Jung, J. C., Chae, K. S., Chang, Y. and Lee, G. H., *ACS Nano* 2009, ***3***, 3663-3669.

141. Ahrén, M., Selegård, L. a., Klasson, A., Söderlind, F., Abrikossova, N., Skoglund, C., Bengtsson, T. r., Engström, M., Käll, P.-O. and Uvdal, K., *Langmuir* 2010, ***26***, 5753-5762.

142. Shi, Z., Neoh, K. G., Kang, E. T., Shuter, B. and Wang, S.-C., *Contrast Media & Molecular Imaging* 2010, ***5***, 105-111.

143. Huang, C.-C., Liu, T.-Y., Su, C.-H., Lo, Y.-W., Chen, J.-H. and Yeh, C.-S., *Chemistry of Materials* 2008, ***20***, 3840-3848.

144. Bridot, J., Faure, A., Laurent, S., Rivière, C., Billotey, C., Hiba, B., Janier, M., Josserand, V., Coll, J., Vander Elst, L., Muller, R., Roux, S., Perriat, P. and Tillement, O., *Journal of the American Chemical Society* 2007, ***129***, 5076-5084.

145. McDonald, M. A. and Watkin, K. L., *Academic radiology* 2006, ***13***, 421-427.

146. Fortin, M., Jr, R. M. P., Söderlind, F., Klasson, A., Engström, M., Veres, T., Käll, P. and Uvdal, K., *Nanotechnology* 2007, ***18***, 395501.

147. Wang, Y., Hussain, S. and Krestin, G., *European radiology* 2001, ***11***, 2319-2331.

148. Josephson, L., Tung, C., Moore, A. and Weissleder, R., *Bioconjugate Chemistry* 1999, ***10***, 186-191.

149. Jun, Y., Huh, Y., Choi, J., Lee, J., Song, H., Kim, K., Yoon, S., Kim, K., Shin, J., Suh, J. and Cheon, J., *Journal of the American Chemical Society* 2005, ***127***, 5732-5733.

150. Jun, Y., Seo, J. and Cheon, J., *Accounts of Chemical Research* 2008, ***41***, 179-189.

151. Tsai, C., Hung, Y., Chou, Y., Huang, D., Hsiao, J., Chang, C., Chen, Y. and Mou, C., *Small* 2008, ***4***, 186-191.

152. Dobson, J., *Drug development research* 2006, ***67***, 55-60.

153. Lee, J. E., Lee, N., Kim, H., Kim, J., Choi, S. H., Kim, J. H., Kim, T., Song, I. C., Park, S. P., Moon, W. K. and Hyeon, T., *Journal of the American Chemical Society* 2009, ***132***, 552-557.

154. Wang, D., He, J., Rosenzweig, N. and Rosenzweig, Z., *Nano Letters* 2004, ***4***, 409-413.

155. Anker, J. N. and Kopelman, R., *Applied Physics Letters* 2003, ***82***, 1102.

156. Lu, H., Yi, G., Zhao, S., Chen, D., Guo, L. H. and Cheng, J., *Journal of Materials Chemistry* 2004, ***14***, 1336-1341.

157. Johannsen, M., Gneveckow, U., Eckelt, L., Feussner, A., Waldöfner, N., Scholz, R., Deger, S., Wust, P., Loening, S. and Jordan, A., *International journal of hyperthermia* 2005, ***21***, 637-647.

158. Feng, J., Shan, G., Maquieira, A., Koivunen, M. E., Guo, B., Hammock, B. D. and Kennedy, I. M., *Analytical Chemistry* 2003, ***75***, 5282-5286.

159. Carpenter, C. M., Pratx, G., Sun, C. and Xing, L., *Physics in Medicine and Biology* 2011, ***56***, 3487.

160. Mi, C., Zhang, J., Gao, H., Wu, X., Wang, M., Wu, Y., Di, Y., Xu, Z., Mao, C. and Xu, S., *Nanoscale* 2010, ***2***, 1141-1148.

161. Yu, X., Shan, Y., Li, G. and Chen, K., *Journal of Materials Chemistry* 2011, ***21***, 8104-8109.

162. Zhang, Y., Pan, S., Teng, X., Luo, Y. and Li, G., *The Journal of Physical Chemistry C* 2008, ***112***, 9623-9626.

163. Narita, A., Naka, K. and Chujo, Y., *Colloids and Surfaces A: Physicochemical and Engineering Aspects* 2009, ***336***, 46-56.

164. Lei, Z., Pang, X., Li, N., Lin, L. and Li, Y., *Journal of Materials Processing Technology* 2009, ***209***, 3218-3225.

165. Gai, S., Yang, P., Li, C., Wang, W., Dai, Y., Niu, N. and Lin, J., *Advanced Functional Materials* 2010, ***20***, 1166-1172.

166. Dosev, D., Nichkova, M., Liu, M., Guo, B., Liu, G.-y., Hammock, B. D. and Kennedy, I. M., *Journal of Biomedical Optics* 2005, ***10***, 064006-064007.

167. Nichkova, M., Dosev, D., Gee, S. J., Hammock, B. D. and Kennedy, I. M., *Analytical Chemistry* 2005, ***77***, 6864-6873.

168. Kim, S., Park, J., Kang, S., Cha, B., Cho, S., Shin, J., Son, D. and Nam, S., *Nuclear Instruments and Methods in Physics Research Section A: Accelerators, Spectrometers, Detectors and Associated Equipment* 2007, ***576***, 70-74.

169. Klasson, A., Ahrén, M., Hellqvist, E., Söderlind, F., Rosén, A., Käll, P. O., Uvdal, K. and Engström, M., *Contrast Media & Molecular Imaging* 2008, ***3***, 106-111.

170. Itoh, H. and Sugimoto, T., *Journal of colloid and interface science* 2003, ***265***, 283-295.

171. Canelas, D. A., Herlihy, K. P. and DeSimone, J. M., *Wiley Interdisciplinary Reviews: Nanomedicine and Nanobiotechnology* 2009, ***1***, 391-404.

172. Stöber, W., Fink, A. and Bohn, E., *Journal of colloid and interface science* 1968, ***26***, 62-69.

173. Berkowitz, A., Schuele, W. and Flanders, P., *Journal of Applied Physics* 1968, ***39***, 1261-1263.

174. Anker, J. N., Behrend, C. and Kopelman, R., *Journal of Applied Physics* 2003, ***93***, 6698-6700.

175. McNaughton, B. H., Kehbein, K. A., Anker, J. N. and Kopelman, R., *The Journal of Physical Chemistry B* 2006, ***110***, 18958-18964.

176. Behrend, C. J., Anker, J. N., McNaughton, B. H. and Kopelman, R., *Journal of Magnetism and Magnetic Materials* 2005, ***293***, 663-670.

177. Champion, J. A., Katare, Y. K. and Mitragotri, S., *Journal of Controlled Release* 2007, ***121***, 3-9.

178. Bridot, J. L., Faure, A. C., Laurent, S., Rivière, C., Billotey, C., Hiba, B., Janier, M., Josserand, V., Coll, J. L. and Vander Elst, L., *Journal of the American Chemical Society* 2007, ***129***, 5076-5084.

179. Bazzi, R., Flores, M., Louis, C., Lebbou, K., Zhang, W., Dujardin, C., Roux, S., Mercier, B., Ledoux, G. and Bernstein, E., *Journal of colloid and interface science* 2004, ***273***, 191-197.

180. Pankhurst, Q. A. and et al., *Journal of Physics D: Applied Physics* 2003, ***36***, R167.

181. Weissleder, R., Stark, D., Engelstad, B., Bacon, B., Compton, C., White, D., Jacobs, P. and Lewis, J., *American Journal of Roentgenology* 1989, ***152***, 167-173.

182. Ozaki, M. and Matijević, E., *Journal of colloid and interface science* 1985, ***107***, 199-203.

183. Pang, T., Cao, W., Xing, M., Feng, W., Xu, S. and Luo, X., *Journal of Rare Earths* 2010, ***28***, 509-512.

184. Cohen, B., *Radiation Dose from Adult and Pediatric Multidetector Computed Tomography* 2007, 33-49.

185. Badea, C., Drangova, M., Holdsworth, D. and Johnson, G., *Phys. Med. Bio.* 2008, ***53***, R319.

186. Zhou, J., Liu, Z. and Li, F., *Chemical Society Reviews* 2012, ***41***.

187. Wang, F., Banerjee, D., Liu, Y., Chen, X. and Liu, X., *Analyst* 2010, ***135***, 1839-1854.

188. Nikitenko, S. I., Koltypin, Y., Liu, Y., Palchik, O., Felner, I., Xu, X. N. and Gedanken, A., *Angewandte Chemie* 2001, ***40***, 4447-4449.

189. Cheong, S., Ferguson, P., Feindel, K. W., Hermans, I. F., Callaghan, P. T., Meyer, C., Slocombe, A., Su, C., Cheng, F., Yeh, C., Ingham, B., Toney, M. F. and Tilley. R. D., *Angewandte Chemie 2011, 123, 4292-4295*.